A STUDY OF STIMULATED RAMAN SCATTERING IN A CO_2 LASER PRODUCED PLASMA

by

GRANT W.J. MCINTOSH

B.Sc.(Hons.) University of Manitoba 1981

M.Sc. University of British Columbia 1984

A THESIS SUBMITTED IN PARTIAL FULFILMENT OF
THE REQUIREMENTS FOR THE DEGREE OF
DOCTOR OF PHILOSOPHY

in

THE FACULTY OF GRADUATE STUDIES
(DEPARTMENT OF PHYSICS)

We accept this thesis as conforming
to the required standard

THE UNIVERSITY OF BRITISH COLUMBIA

January 1987

In presenting this thesis in partial fulfilment of the requirements for an advanced degree at the University of British Columbia, I agree that the Library shall make it freely available for reference and study. I further agree that permission for extensive copying of this thesis for scholarly purposes may be granted by the head of my department or by his or her representatives. It is understood that copying or publication of this thesis for financial gain shall not be allowed without my written permission.

Department of Physics

The University of British Columbia
1956 Main Mall
Vancouver, Canada
V6T 1Y3

Date January 26, 1987

ABSTRACT

Stimulated Raman scattering (SRS) has been studied experimentally in a CO_2 laser plasma interaction. A N_2 gas jet target was irradiated with CO_2 laser light (wavelength, $\lambda = 10.6\mu$m and frequency, ω_o) at intensities up to 10^{14} Wcm^{-2}. SRS occurs at intensities greater than 3 x 10^{13} Wcm^{-2}, which is fair agreement with threshold predictions for a plasma with an electron temperature of 300eV and a density scale length of 300μm. After this intensity is reached, the plasma waves grow exponentially in time with a growth rate of 6 x $10^{-3}\omega_o$. This was measured with ps resolution ruby laser Thomson scattering. Spatial growth was also observed. Scattered infrared light at 2λ was found. Weak IR light in a broad band near 15μm was also found. The saturated plasma wave level and the number of hot electrons at 150 keV are well correlated, which indicates that trapping is responsible for the electrons. However, trapping is not responsible for the saturation of the instability. Frequency resolved Thomson scattering revealed that ion acoustic waves start at the peak of the SRS fluctuations. Once the ion acoustic waves grow to a large amplitude, SRS is quenched and does not reappear.

TABLE OF CONTENTS

LIST OF TABLES

LIST OF FIGURES

ACKNOWLEDGMENTS

I am deeply indebted to my supervisor, Dr. Jochen Meyer, for his constant interest and encouragement in the course of this work, and for many stimulating discussions and suggestions. Special thanks are extended to Zhang Yazhou for his tireless aid in the infrared diagnostics. Hubert Houtman's skilful operation of the ruby laser is also much appreciated. I would also like to extend a thank-you to Dr. A.J.Barnard who attempted against tremendous odds to improve the English of the thesis. (Any remnants of awkward grammar are my own responsibility.) Finally, I would like thanks to Dr. John Bernard, Dr. Roman Popil, Greg Stuart, Kelly Mah and Jim Booth for many hours of moral support, colourful discussions, and last, but not least, the Friday afternoon beer gardens which made graduate life bearable (BEERable?).

LIST OF SYMBOLS

- A – the atomic weight of ions in the plasma
- $\vec{B}$, B – magnetic field
- c_s – ion acoustic wave speed
- c – vacuum speed of light
- $\vec{E}$, E – electric field (sometimes with a subscript)
- e – the charge on the electron
- EMW, EM, em – electromagnetic wave
- EPW, epw – electron plasma wave
- I – intensity (usually of the incident laser light)
- IA, ia – ion acoustic
- $\vec{J}$ – current density
- k_x – wave vector for oscillation x
- k_d – Debye wavevector
- k_o – wavevector of CO_2 light in the plasma
- k_BT – temperature in energy units (usually eV)
- L – density scale length
- m_e, m – mass of the electron
- N – number density (sometimes with a subscript)
- n – electron number density (sometimes with subscript)
- n_{cr} – the critical electron number density
- R – reflectivity
- r_e – classical electron radius
- SBS – stimulated Brillouin scattering
- SRS – stimulated Raman scattering
- TPD – two-plasmon decay instability
- U – energy density (usually with a subscript)
- v_- – group velocity of scattered em wave

- v_{epw} – group velocity of epw
- v_{ph}, v_p – phase velocity of epw
- v_o – the quiver velocity of an electron in an electric field
- v_e, v_{th} – electron thermal speed
- Z – average ionic charge in the plasma
- ω_x – angular frequency for oscillation x
- ω_p – electron plasma frequency
- ω_o – angular frequency of incident CO_2 laser
- ϕ – electrostatic wave potential
- ν_{ei} – the electron-ion collision frequency
- Λ – the Coulomb logarithm
- λ – wavelength (sometimes with a subscript)
- λ_D – Debye length
- δn – electron number density fluctuation amplitude
- γ – growth or damping rate (sometimes with a subscript)
- κ' – gradient of wave vector mismatch
- $d\Omega, \Delta\Omega$ – differential solid angle
- Ω_c – electron cyclotron frequency
- θ – angle between incident and scattered ruby light
- χ_e – susceptibility
- τ – short period of time
- Ψ – angle between incident and scatterd CO_2 light

CHAPTER 1

Introduction

1.1 Preliminary Remarks

Early in the twentieth century, the interaction of light with matter was investigated on many fronts. One observation of particular interest to this work was made by Raman who noted that light scattered from molecules was shifted by frequencies characteristic of vibrations in the molecule. Subsequent work showed that this phenomenon was universal – light scattered from solids, liquids, and gases could show characteristic shifts. A plasma, too, has its characteristic frequencies and light scattered from it does show a frequency shift. The frequency difference which is of most interest in this work is approximately the electron plasma frequency. (This plasma frequency is proportional to the square root of the electron number density. The density at which the incident laser frequency equals the plasma frequency is called the critical density, n_{cr}.) Light which leaves the plasma with this frequency shift is said to be Raman scattered. In the late 1960's, the theory of parametric oscillators (originally derived for electrical applications) was applied to a laser-plasma interaction. An interesting result was found – the Raman scattering was, for high light intensities, an instability and would grow exponentially. The name for this instability is stimulated Raman scattering (SRS).

The invention of the laser made it possible to study the interaction of electromagnetic radiation with matter at previously unattainable intensities. In particular, the power levels were such that the parametric instabilities could be excited. These

instabilities were interesting for basic scientific reasons alone. However the same high intensities also made laser fusion a possibility. Fusion schemes proposed the compression of small pellets of deuterium-tritium fuel to high densities and to high temperatures. At these high densities and temperatures the fusion reaction can procede at its optimum rate. The proposed method involved the irradiation of the outer surface of the pellet with high intensity laser beams. The outer layer would blow off and the inner core would be compressed by the implosion that is a consequence of the conservation of momentum. The material blown off would be a plasma and hence, the study of the laser interaction with the plasma became of practical importance.

Computer simulations showed that the interaction has some serious and unexpected consequences. There was, of course, scattered light. If the incident light is less efficiently absorbed the possible compression of the target is reduced. More importantly, associated with SRS was the production of high energy electrons. These electrons would stream forward from the blowoff plasma and enter the fuel pellet where they would lose their energy and heat up the pellet, making the compression even more difficult.

The analytical and computer models of the interaction of light with the target had to be confirmed experimentally. The first observation of SRS was made by Bobin in 1973 and this remained the only observation until 1978. Since then, experiments have shown that SRS is indeed a troublesome problem. The enhanced levels of scattered light have been measured. The fast electrons predicted by the simulations have been observed. Yet, as more and more experiments were conducted at higher and higher intensities, some unexpected results were obtained. The most puzzling result was a gap in the frequency spectra of the scattered laser light. [1] A gap in the spectra can be thought of as a gap in the densities at which the scattering is thought to be occurring. The observed gap corresponded to densities between 0.1 and 0.24 n_{cr}.

Since each scattered light wave is produced by a particular plasma wave, one would also expect a gap in the plasma wave spectrum. It is therefore worthwhile to study the plasma waves by other methods. If no gap in the plasma wave spectrum is observed and if a gap is observed in the IR spectrum, then the model of SRS may have to be modified. The standard model of SRS is described in detail in chapter 2.

It is also important to measure the properties of the high energy electrons. If either their number or their energies disagree with the computer simulations, then the plans for laser fusion may have to be changed. The best way to check the simulations would be to compare the properties of the observed plasma waves with the electrons.

An instability which grows exponentially cannot continue to do so forever; there must be some mechanism which saturates and quenches the growth. Simulations have shown that the presence of fast electrons can cause saturation. Other simulations have shown that coupling between the electron plasma waves and other waves in the plasma can cause saturation. Once again experiments can be set up which can determine if either of these mechanisms is responsible.

1.2 Motivation for the Present Work

With the brief background provided, the motivation for the present work becomes clearer. In a plasma generated by a CO_2 laser (wavelength λ_o=10.6μm), all the aspects of SRS are observable with standard techniques. The density fluctuations can be measured with Thomson scattering, the scattered EM waves can be detected with sensitive infrared detectors, and the electrons can be analyzed with a simple electron spectrometer and scintillator detectors.

The major questions to be answered by this work are:

- In a plasma of a known density, are there enhanced fluctuations present corresponding to that density?

- Is there scattered light corresponding to the observed fluctuations?
- How are the number and energy distribution of the high energy electrons related to the enhanced fluctuations?
- What causes SRS to saturate and decay?

1.3 Organization of the Thesis

The theory and the observable consequences of SRS relevant to this work are presented in chapter 2. In chapter 3, the experimental details and the methods of analysis used on the data are given. Chapter 4 contains the results of my experiments while the implications and comparisons with theory and other experiments are found in Chapter 5. In Chapter 6 a consistent and concise summary of the SRS process is found. The original contributions of this work and suggestions for further work end that chapter.

Throughout this thesis the CGS Gaussian system of units is used. Only equations which are quoted elsewhere in the thesis are numbered.

CHAPTER 2

Theory of stimulated Raman scattering

2.1 Introduction

A plasma consists of a free electron gas interspersed in a free ion gas. As such, an electromagnetic wave interacting with it can be handled readily. Work of this nature has been undertaken since the 1960's and has shown that many nonlinear optical phenomena should occur in a plasma if the incident EM field is large enough. Indeed, the nonlinear aspects are hardly avoidable.

In this chapter, the physical origin of such nonlinear phenomena is explained. The discussion begins with an overview of parametric instabilities with emphasis on Stimulated Raman Scattering (SRS). This is followed by a derivation of the basic growth rate for SRS and the related two-plasmon decay (TPD) instability for a homogeneous plasma. Expressions for the threshold intensity and the growth rate under more realistic assumptions are then reviewed for comparison with experimental results. The chapter ends with a discussion of computer simulations.

2.2 Overview of SRS

In a plasma, in the absence of an external magnetic field, three types of waves can be supported : a high frequency longitudinal electron plasma wave (EPW), a low frequency longitudinal ion acoustic wave (IAW), and a high frequency transverse electromagnetic wave (EMW). Each wave has a frequency, ω and a wave

vector, k. These waves obey dispersion relations which can be written in the following simplified forms [12]:

$$\omega_{EPW}^2 = \omega_p^2 + 3k_B T k_{EPW}^2/m_e,$$

$$\omega_{IAW} = c_s k_{IAW},$$

and

$$\omega_{EMW}^2 = \omega_p^2 + c^2 k_{EMW}^2,$$

where the plasma frequency

$$\omega_p = \sqrt{\frac{4\pi n_e e^2}{m_e}},$$

and ion acoustic speed

$$c_s = \sqrt{Zk_B T/m_i}$$

have been introduced.

In a parametric instability, one of these waves decays into two others, subject to the scattering conditions

$$\vec{k}_o = \vec{k}_1 + \vec{k}_2$$

and

$$\omega_o = \omega_1 + \omega_2.$$

These conditions are sometimes refered to as conservation of momentum and energy, which is not correct; they are phase matching conditions. In the decay of an incident EM wave, four decay modes are possible:

$$EMW \rightarrow EMW + IAW \quad \text{(Stimulated Brillouin Scattering)}$$

$$EMW \rightarrow EMW + EPW \quad \text{(Stimulated Raman Scattering)}$$

$$EMW \rightarrow EPW + IAW \quad \text{(Parametric Decay Instability)}$$

and

$$EMW \rightarrow EPW + EPW \quad \text{(Two - plasmon Decay Instability).}$$

Other decays (e.g. $EMW \rightarrow EMW + EMW$) are forbidden since the dispersion relations and the scattering conditions cannot be satisfied simultaneously.

If only the dispersion relations at temperature T=0 and the scattering conditions are considered for SRS the following can be found: (1) for the scattered EM wave, of frequency ω_s,

$$\frac{\omega_s}{\omega_o} = 1 - \frac{\omega_p}{\omega_o} \qquad 2-1$$

and (2) for the electron plasma wave,

$$(k_{epw}) = \frac{\omega_o}{c}[(1 - \frac{\omega_p^2}{\omega_o^2}) + (1 - \frac{2\omega_p}{\omega_o}) - 2(1 - \frac{\omega_p^2}{\omega_o^2})^{1/2}(1 - \frac{2\omega_p}{\omega_o})^{1/2}\cos\psi]^{1/2} \qquad 2-2$$

where ψ is the angle between the incident (frequency ω_o) and scattered EM waves. The density at which $\omega_o = \omega_p$ is called the critical density n_{cr} so that $\omega_p^2/\omega_o^2 = n/n_{cr}$.

One dimensional computer simulations [2,3] have shown that high energy electrons can be generated by SRS and that the electrons have, at high energies, a distribution of velocities that decreases exponentially. Such a decrease is characteristic of a Maxwellian distribution. The simulations indicate that an approximate temperature

$$k_B T = m_e c^2([1 - (\frac{\omega_{epw}}{ck_{epw}})^2]^{-1/2} - 1) \qquad 2-3$$

can be fitted. The physical explanation for this behaviour is not known.

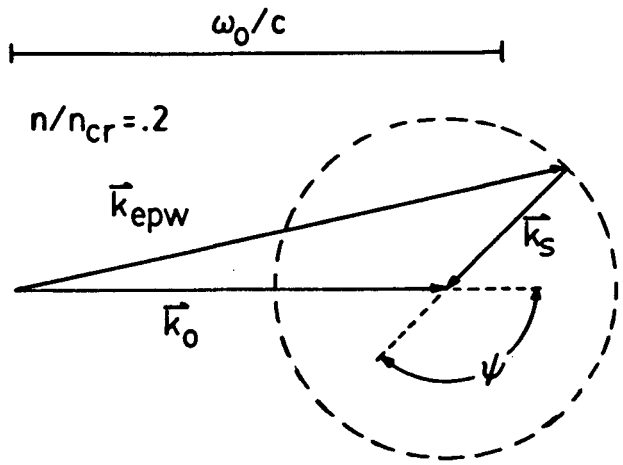

Figure 2-1 Wavevector matching conditions for SRS. The drawing is to scale. $k_o \neq \omega_o/c$ because of dispersion in the plasma.

The amount of scattered energy can be estimated. If we imagine n EM quanta decaying to n scattered EM quanta and n EPW quanta, we get the trivial relationships

$$\frac{n\hbar\omega_o}{\omega_o} = \frac{n\hbar\omega_s}{\omega_s} = \frac{n\hbar\omega_{epw}}{\omega_{epw}} \qquad 2-4$$

which are the Manley-Rowe conditions [4] that relate the total energy in a particular mode ($n\hbar\omega$) to that in any other. The ratio of the respective frequencies indicates the relative amounts of energy in each mode. (These relations were originally derived for classical oscillators in which the energy in a particular mode is $E^2/(8\pi)$ where E is the electric field associated with that mode.) The energy in a given

mode does not have to remain in that mode. The scattered EM radiation could be absorbed by the plasma through other processes, such as inverse bremsstrahlung absorption while the plasma wave energy could be partially or completely transferred to the electrons.

To sum up SRS has the observable consequences of a scattered EM wave, an enhanced electron plasma wave fluctuation, and high energy electrons. The relative amount of energy in each of these systems should be related to each other. For ψ=180°, i.e. for direct electromagnetic backscatter, the values for these observables have been plotted in figures 2-2, 2-3 and 2-4 as a function of plasma density.

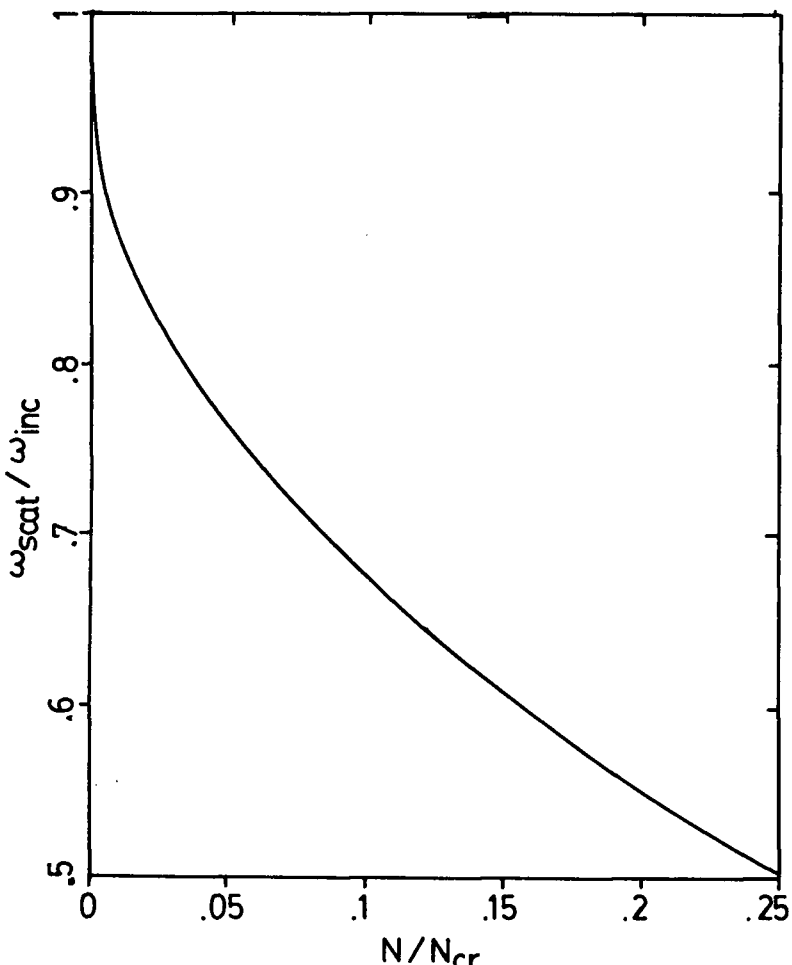

Figure 2-2 Frequency of scattered Raman light from eqn 2-1.

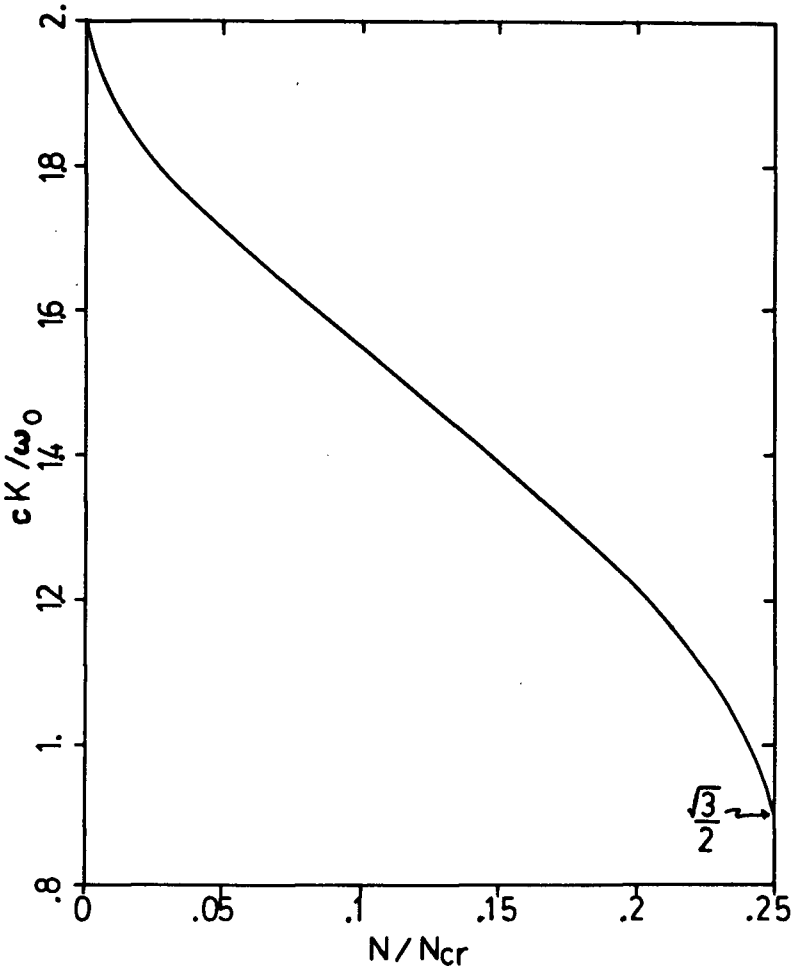

Figure 2-3 Wavevectors of Raman fluctuations from eqn 2-2.

2.3 Details of SRS and Two-plasmon Decay

The mechanisms which determine the presence and importance of SRS cannot be found by considerations of the previous section alone. The details of the interaction must be studied. In this section a derivation of the growth rate, γ_o, of SRS in an infinite, homogeneous plasma is given. There are several assumptions made and these are clearer if explicitly pointed out as they are made. The homogeneous growth rate is the maximum rate at a given density and defines a timescale for SRS. The lower growth rates in a finite or inhomogeneous plasma usually involve a knowledge of γ_o. The following derivation is based upon a number of sources with the important ones being Jackson [5], Shen [6], Tsytovich [7], Forslund et al.[8], Drake

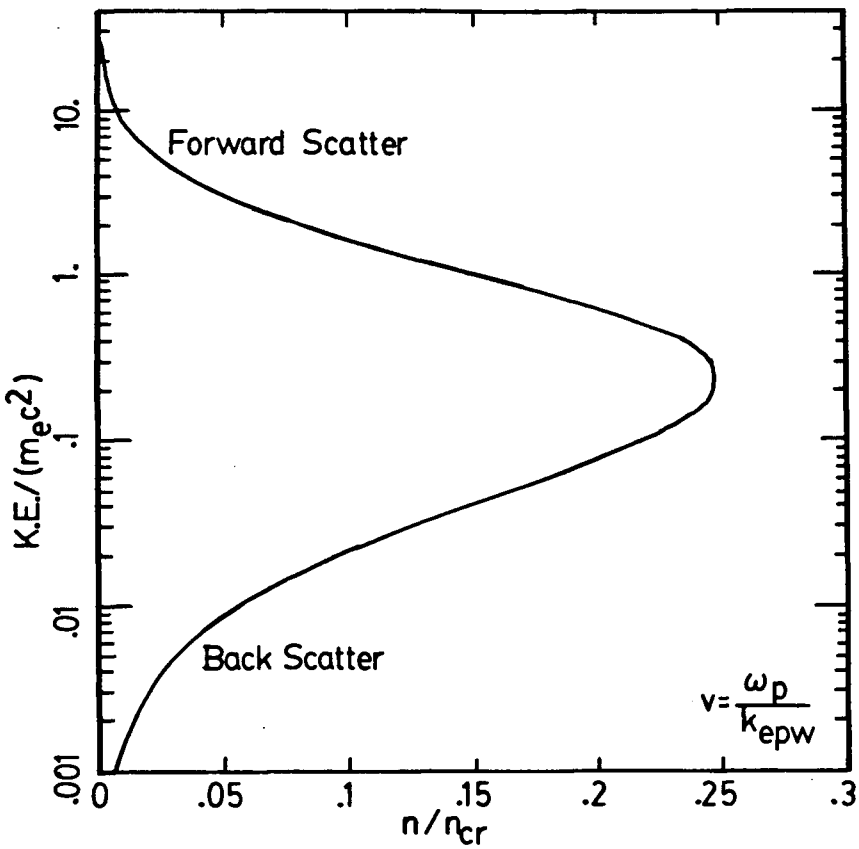

Figure 2-4 Expected fast electron temperatures from eqn 2-3.

et al.[9] and Langdon et al.[10]. It is not mathematically rigorous but the physical mechanisms should be clear.

The starting point is Maxwell's equations:

$$\nabla \times \vec{B} = \frac{1}{c}\frac{\partial \vec{E}}{\partial t} + \frac{4\pi}{c}\vec{J}$$

$$\nabla \cdot \vec{B} = 0$$

$$\nabla \times \vec{E} = -\frac{1}{c}\frac{\partial \vec{B}}{\partial t}$$

$$\nabla \cdot \vec{E} = 4\pi \sum_j (N_j q_j) \qquad 2-5.$$

In this section, the following symbols are used: $\vec{E}$ for electric field, $\vec{B}$ for magnetic field, c for the speed of light, N_j for number density of species j with charge q_j, e for the electron charge, v for the plasma fluid velocity, ω for angular frequency of a wave, and $\vec{k}$ for the wavevector of a wave. The wave equation for $\vec{E}$ is

$$\nabla(\nabla \cdot \vec{E}) - \nabla^2 \vec{E} - \frac{1}{c^2}\frac{\partial^2 \vec{E}}{\partial t^2} = \frac{4\pi}{c}\frac{\partial \vec{J}}{\partial t}$$

which upon Fourier transformation gives

$$-\vec{k}(\vec{k} \cdot \vec{E}) + k^2 \vec{E} - \frac{\omega^2}{c^2}\vec{E} = \frac{4\pi i\omega}{c}\vec{J}.$$

Physically, one imagines $\vec{E}$, the electric field, as being generated by currents, $\vec{J}$. $\vec{J}$ may be generated by a nonlinear response in a plasma. If we neglect ion currents we get

$$\vec{J}(\vec{r},t) = eN(\vec{r},t)\vec{v}(\vec{r},t) \qquad 2-6$$

and

$$\vec{J}(\vec{k},\omega) = e\int\int N(\vec{k}',\omega')\vec{v}(\vec{k}'',\omega'')\delta(\vec{k}-\vec{k}'-\vec{k}'')\delta(\omega-\omega'-\omega'')d^3\vec{k}'d^3\vec{k}''d\omega'd\omega''.$$

In an infinite plasma the integrals are replaced by sums over all $\vec{k}', \vec{k}''$ which satisfy the matching conditions. N($\vec{r}$, t) and $\vec{v}(\vec{r},t)$ are described in the fluid model for the plasma, the conservation of momentum:

$$\frac{\partial \vec{v}}{\partial t} + \vec{v} \cdot \nabla \vec{v} = \frac{q}{m_e}(\vec{E} + \frac{\vec{v}}{c} \times \vec{B}) - \frac{3k_b T}{m_e N_o}\nabla N \qquad 2-7$$

and the continuity equation:

$$\frac{\partial N}{\partial t} + \nabla \cdot (N\vec{v}) = 0 \qquad 2-8.$$

The term involving ∇N in Eqn. 2-7 represents the pressure gradient force in an ideal gas. $\vec{J}(\vec{k},\omega)$ must be calculated using realistic assumptions. Since three wave interactions in the presence of a strong EM wave (identified by the subscript o) are of most interest, this will lead to a natural choice of couplings between the three waves in which the differences in wavevector and frequency of two of the waves are equal to $\vec{k}_o$ and ω_o. Only lowest order couplings will be considered.

This set of equations (Eqn. 2-5 to 2-8) can be solved numerically with a computer. Initial analytic behaviour can be found by using expansion techniques. The density N is separated into two parts, a constant average density N_o and a fluctuating part n. First, the linear response of the plasma to an EMW is found. The linear dispersion relations for an EMW and an EPW are derived. The density fluctuation level which is enhanced by the nonlinear response of the plasma is calculated next. The nonlinear dispersion relation for the scattered wave is given and the growth rate for SRS is derived from it. In the following the subscripts on $\vec{E}$, $\vec{k}$, and ω refer to particular waves.

The linear response of a plasma to an electric field $\vec{J}(\vec{k}_1,\omega_1)$ is easy to calculate. We need to find

$$\frac{4\pi}{c^2}\frac{\partial \vec{J}}{\partial t} \approx \frac{4\pi e N_o}{c^2}\frac{\partial \vec{v}}{\partial t}.$$

We substitute for the derivative of $\vec{v}$ neglecting the $\vec{v}\times\vec{B}$, $\vec{v}\cdot\nabla$ and $\partial(n\vec{v})/\partial t$ terms from eqn 2-7. Upon Fourier transforming, we get

$$\frac{i\omega_1}{c^2}\vec{J}(\vec{k}_1,\omega_1) = \frac{\omega_p^2}{c^2}\vec{E}_1 - \frac{3k_BT4\pi e i\vec{k}_1 n}{m_e c^2}.$$

To find n we neglect the $\nabla \cdot (n\vec{v})$ term in the continuity equation (eqn 2-8) and Fourier transform the result to get , upon rearrangement ,

$$n(\vec{k}_1, \omega_1) = \frac{N_o \vec{k}_1 \cdot \vec{v}}{\omega_1}.$$

To find $\vec{v}$, we Fourier transform the equation describing the variation of v and neglect all terms except that involving $\vec{E}_1$. Rearranging , we find

$$\vec{v} = \frac{ie\vec{E}_1}{m_e \omega_1}.$$

Substituting $\vec{v}$ into the expression for n and n into the expression for $\vec{J}$, we obtain

$$\frac{i\omega_1 \vec{J}(\vec{k}_1, \omega_1)}{c^2} = \frac{\omega_p^2}{c^2}\vec{E}_1 + \frac{3k_B T \omega_p^2 \vec{k}_1 (\vec{k}_1 \cdot \vec{E}_1)}{m_e c^2 \omega_1^2}.$$

Substituting this into the wave equation for $\vec{E}_1$ and regrouping the terms we see that

$$[(-1 + \frac{\omega_p^2 3k_B T}{\omega_1^2 m_e c^2})\vec{k}_1\vec{k}_1 + (k_1^2 - \frac{\omega_1^2}{c^2} + \frac{\omega_p^2}{c^2})\vec{I}\vec{I}] \cdot \vec{E}_1 = \frac{4\pi i \omega_1 \vec{J}_{N.L.}(\vec{k}_1, \omega_1)}{c^2}$$

where $\vec{J}_{N.L.}$ contains the non-linear terms and $\vec{I}\vec{I}$ is the unit dyadic tensor. When the nonlinear term is neglected, the dispersion relations for transverse ($\vec{k}_1 \cdot \vec{E}_1 = 0$) and longitudinal waves are obtained, namely,

$$\omega_1^2 = \omega_p^2 + c^2 \vec{k}_1^2 \quad \text{(Transverse)}$$

and

$$\omega_1^2 = \omega_p^2 + \frac{\omega_p^2 3k_B T \vec{k}_1^2}{\omega_1^2 m_e} \quad \text{(Longitudinal)}.$$

(Remember that $\omega_p \approx \omega_1$.)

The term $\vec{J}_{N.L.}$ must now be calculated. It is generated by the density perturbation $n(\vec{k}_2, \omega_2)$ beating with the velocity generated by the incident EMW$(\omega_o, \vec{k}_o)$ where $\vec{k}_2 = \vec{k}_o - \vec{k}_1$ and $\omega_2 = \omega_o - \omega_1$. Higher order couplings and the anti-Stokes coupling are neglected. In this approximation we find

$$\frac{i\omega_1 \vec{J}_{N.L.}}{c^2} = \frac{i\omega_1 en(\vec{k}_2, \omega_2)\vec{v}(\vec{k}_o, \omega_o)}{c^2}.$$

The quiver velocity $\vec{v}(\vec{k}_o, \omega_o)$ is given by

$$\vec{v}(\vec{k}_o, \omega_o) = \frac{ie\vec{E}_o}{m_e \omega_o}.$$

(Hereafter, v_o actually refers to $v(\vec{k}_o, \omega_o)$.)

$n(\vec{k}_2, \omega_2)$ must be calculated from the wave equation which is found by combining the continuity and momentum equations for the fluid. The resulting equation for n, neglecting $\nabla\vec{v} \cdot \nabla\vec{v}$, is

$$\frac{\partial^2 n}{\partial t^2} + \frac{3k_B T \nabla^2 n}{m_e} + \frac{N_o e \nabla \cdot \vec{E}}{m_e} = \frac{eN_o \nabla \cdot (\vec{v} \times \vec{B})}{m_e c}.$$

As usual this is Fourier transformed to get

$$[-\omega_2^2 + \frac{3k_B T k_2^2}{m_e} + \omega_p^2]n = \frac{N_o \vec{k}_2}{c} \cdot \int\int \vec{v}' \times (\vec{k} \times \frac{e\vec{E}}{m_e})'' \delta(\vec{k}_2 - \vec{k}' - \vec{k}'') d\vec{k}' d\vec{k}''.$$

The RHS gives rise to a term of the form

$$\frac{k_2^2 N_o e^2 \vec{E}_o \cdot \vec{E}_1}{m_e^2 \omega_o \omega_1}.$$

Thus we find

$$n(\vec{k}_2,\omega_2) = \frac{k_2^2 \vec{E}_o \cdot \vec{E}_1 \omega_p^2}{(\omega_2^2 - \omega_p^2 - 3k_B T k_2^2/m_e)4\pi m_e \omega_o \omega_1}.$$

n is generated by the beating of $\vec{E}_o$ and $\vec{E}_1$ and is enhanced because of the $\vec{v} \times \vec{B}$ force. Using this n and the $\vec{v}(\vec{k}_o,\omega_o)$ we find the expression for $\vec{J}_{N.L.}$ which can be substituted into the wave equation for $\vec{E}_1$. The result is

$$[(-1 + \frac{\omega_p^2 3k_B T}{\omega_1^2 m_e c^2})\vec{k}_1\vec{k}_1 + (k_1^2 - \omega_1^2/c^2 + \omega_p^2/c^2)\vec{I}\vec{I}] \cdot \vec{E}_1 = \frac{\omega_p^2 \omega_1 n(\vec{k}_2,\omega_2)\vec{E}_o}{c^2 \omega_o N_o}.$$

This is readily inverted to give the scattered field

$$\vec{E}_1 = \omega_p^2 \frac{\omega_1}{\omega_o} \frac{n(\vec{k}_2,\omega_2)}{N_o} [(\vec{I}\vec{I} - \frac{\vec{k}_1\vec{k}_1}{k_1^2}) \frac{1}{(k_1^2 c^2 - \omega_1^2 + \omega_p^2)} - \frac{\vec{k}_1\vec{k}_1}{k_1^2(\omega_1^2 - \omega_p^2 - \omega_p^2 3k_B T k_1^2/\omega_1^2 m_e)}] \cdot \vec{E}_o.$$

Upon substituting for $n(\vec{k}_2,\omega_2)$, taking the dot product of $\vec{E}_o$ with both sides, cancelling $\vec{E}_o \cdot \vec{E}_1$ and recognizing that $(\vec{k}_1 \times \vec{E}_o)^2 = k_1^2 E_o^2 - (\vec{k}_1 \cdot \vec{E}_o)^2$, one arrives at the dispersion relation

$$1 = \frac{-k_2^2 \omega_p^2 e^2}{(\omega_2^2 - \omega_p^2 - 3k_B T k_2^2/m_e) m_e^2 \omega_o^2} \{ \frac{(\vec{k}_1 \times \vec{E}_o)^2}{k_1^2(k_1^2 c^2 - \omega_1^2 + \omega_p^2)} - \frac{(\vec{k}_1 \cdot \vec{E}_o)^2}{k_1^2(\omega_1^2 - \omega_p^2 - 3k_B T k_1^2 \omega_p^2/\omega_1^2 m_e)} \}. \qquad 2-9$$

This expression is equivalent to that given by Drake [9] provided (a) ions are neglected; (b) thermal effects are included; (c) the fluid susceptibilities

$$\chi_e(\omega,k) = \frac{-\omega_p^2}{\omega^2 - 3v_e^2 k^2}$$

are used in place of the kinetic ones; and (d) the anti-Stokes coupling is neglected. The importance of the terms in the { } in Eqn. 2-9 is found by examining the respective denominators. If the denominator is small (near zero) the term is quite important. The first term applies to SRS and the second term applies to the TPD instability. The cross and scalar products determine the important scattering directions. For SRS, the cross product implies that there should be no scattered EM wave in directions parallel to the incident, linearly polarized $\vec{E}_o$ and that EM scattering should be strongest in the plane perpendicular to $\vec{E}_o$. For TPD, the scalar product means the reverse situation is true i.e. the best planes for viewing EPW are those planes in which $\vec{E}_o$ lies. If we neglect the second term in the brackets in Eqn. 2-9 and rearrange the result we find

$$(\omega_2^2 - \omega_p^2 - 3k_BTk_2^2/m_e)(\omega_1^2 - \omega_p^2 - c^2k_1^2) = \omega_p^2k_2^2(v_o\sin(\pi/2 - \psi))^2 \qquad 2-10$$

where $\pi/2 - \psi$ is the angle between $\vec{k}_1$ and $\vec{v}_o$. Let $\omega_2 = \omega_{2r} + i\gamma$, $\omega_1 = \omega_{1r} - i\gamma$, $\gamma/\omega_1 \ll 1$ (where γ is the growth rate), $\omega_{2r}^2 = \omega_p^2 + 3k_BTk_2^2/m_e$ and $\omega_{1r}^2 = \omega_p^2 + c^2k_1^2$. With the substitution for $\omega_{2r} \approx \omega_p$ and $\omega_{1r} = \omega_o - \omega_{2r}$ into Eqn. 2-10 becomes

$$4\gamma^2\omega_{2r}\omega_{1r} = \omega_p^2k_2^2v_o^2\sin^2(\pi/2 - \psi).$$

The final result (with minor changes in notation) [8] is

$$\gamma_o = 0.5\frac{k_{epw}v_o\omega_p\sin(\pi/2 - \psi)}{\sqrt{\omega_p(\omega_o - \omega_p)}}. \qquad 2-11$$

This γ_o is the growth rate for SRS for an infinite, homogeneous plasma in the regime where damping (so far neglected) is not important and v_o is small enough that the approximation $\gamma/\omega \ll 1$ is valid. γ_o reaches a maximum when $\psi = \pi$ (direct backscatter). It should be remembered that k_{epw} depends upon ψ.

When $n = 0.25 n_{cr}$ the growth rate for TPD that is derived from Eqn. 2-9 is incorrect. At that density $k_1 = 0$, and both terms in the dispersion relation must be retained. Langdon [10] has considered this problem carefully and derived a slightly different dispersion relation for the TPD instability; the term corresponding to SRS remains unchanged. The modified dispersion relation reads

$$(\omega_2^2 - \omega_p^2 - 3k_B T k_2^2/m_e) = \frac{\omega_p^2 k_2^2 (\vec{k}_1 \times \vec{v}_o)^2}{2(\omega_1^2 - \omega_p^2 - c^2 k_1^2) k_1^2} + \frac{\omega_p^2 (k_1^2 - k_2^2)^2 (\vec{k}_1 \cdot \vec{v}_o)^2}{2(\omega_1^2 - \omega_p^2 - 3k_B T k_1^2/m_e) k_1^2 k_2^2}.$$

Considering only the TPD instability component we find the growth rate for TPD to be

$$\gamma_{2\omega_p} = \frac{k_o v_o}{2} \left[1 + \left(\frac{(k_x - k_o/2)^2 - (k_y^2 + k_o^2/4)}{2k_y (k_x - k_o/2)} \right)^2 \right]^{-1/2}. \qquad 2-12$$

This growth rate is a maximum if

$$(k_x - k_o/2)^2 = (k_y^2 + k_o^2/4) \qquad 2-13$$

which for $k_x, k_y \gg k_o$ reduces to $k_x = \pm k_y$. For $k_y = 0$, $k_x = k_o$ is the condition for maximum growth. When both terms are considered, the resulting wave is a mixed transverse-longitudinal mode. This is sometimes called the SRS-TPD hybrid mode. (The matching wave is purely longitudinal.)

To summarize: SRS grows at a rate γ_o given by Eqn. 2-11 and for $0.25 n_{cr}$ the effects of SRS and the TPD instability cannot be separated.

2.4 Thresholds, Growth Rates and Fast Electrons

The previous theory considered the case of undamped waves, a constant v_o, an infinite plasma, and no gradients in density, temperature or plasma velocity. These assumptions will be relaxed and the implications discussed.

The various waves generated can be damped by several means. Plasma waves can be damped by either collisionless Landau damping [11], at a rate given by

$$\gamma_l = \omega_p(\pi/8)^{1/2}(k_d/k)^3 \exp(-0.5(k_d/k)^2 \qquad 2-14$$

or by collisional damping

$$\gamma_c = \nu_{ei}/2$$

or both, where ν_{ei} is the electron-ion collision frequency [12]

$$\nu_{ei}(\mathrm{s}^{-1}) = \frac{1.5 \times 10^{-6} Z n_e(\mathrm{cm}^{-3})\Lambda}{T^{3/2}(\mathrm{eV})}.$$

Λ is the Coulomb logarithm, $\ln(12\pi n_e \lambda_D^3)$, with λ_D (cm)$= 6.9(T(^\circ K)/n_e(\mathrm{cm}^{-3}))^{1/2}$, the Debye length. (For the plasma conditions encountered in the present experiment the value of Λ can be set to 10.) Electromagnetic waves are mainly damped by collisional damping (inverse bremsstrahlung) for which the decay rate is

$$\gamma_{em} = \nu_{ei}\omega_p^2/2\omega_{em}^2.$$

The finite damping introduced by these rates requires that a threshold growth rate γ_T given by

$$\gamma_T^2 = (\gamma_l + \gamma_c)\gamma_{em} \qquad 2-15$$

must be reached before SRS occurs and once threshold is exceeded, the plasma waves grow but at a lower rate than γ_o. (Well above threshold, growth at γ_o is recovered.)

One obvious saturation mechanism is the decline in the incident laser light intensity as the interaction proceeds. Since the plasma waves and the backscattered waves are growing, some energy must be supplied. The incident EMW acts as the supply but its energy is not infinite. When energy is transfered to the waves and

the waves subsequently are damped, the energy cannot be returned to the pump wave. A steady state situation is soon reached. At this stage pump depletion has set in and the waves no longer grow. This process has been studied recently by McKinstrie et al. [13] (whose results agreed with simulations of Hiob and Barnard [14]). McKinstrie showed that the intensity reflectivity R saturates in an infinite, collisional plasma at

$$R = (\frac{\omega_s}{\omega_o})^3(\frac{m-1}{m^2}) \qquad 2-16$$

where $m = \gamma_o/\gamma_T$; note that $m \geq 1$. This suggests a lower reflectivity than that expected from the Manley-Rowe relations. R is a sensitive function of the threshold growth rate γ_T.

In any real experimental situation, a plasma is neither infinite nor homogeneous. The finite length of the interaction region has some consequences on the nature of the instability. Is it a convective or an absolute instability? The terms convective and absolute refer to the pattern of growth in space and time. Convective growth is such that after a short time $\tau = L/v_-$ the amplitude of a wave grows exponentially in space only. Absolute growth refers to growth which occurs everywhere, exponentially in time. In a finite but homogeneous plasma of length L, it seems reasonable to expect a minimum length for convective growth of SRS to occur and a maximum length above which the infinite homogeneous limit of absolute growth is recovered. Kroll [15] showed if L$< (v_- v_{epw})^{1/2}/\gamma_o$, only convective growth will occur, if $(v_- v_{epw})^{1/2}/\gamma_o <$ L $< v_-/\gamma_o$, absolute growth occurs but at a reduced rate

$$\gamma_r = 2\sqrt{(v_- v_{epw})/(v_- - v_{epw})^2}\gamma_o, \qquad 2-17$$

and if L$> v_-/\gamma_o$, growth at γ_o will be recovered for a time τ, followed by continued growth at the reduced rate. (v_- and v_{epw} are the group velocities of the scattered EM and plasma wave respectively.) Forslund et al.[8] showed that the absolute

instability in a finite plasma leads to both the reduced temporal growth (Eqn. 2-17) and a spatial growth (for weakly damped waves)

$$\mathrm{Im}k = \frac{\gamma_o}{\sqrt{v_{epw}v_-}} \qquad 2-18.$$

The physical reason for this behaviour is clearer if one realizes that the EM waves can escape from the plasma and also that the disturbance takes a finite time to propagate across the plasma. At the edge of the plasma facing the incident pump wave, the waves will have a headstart in growth compared to those at the far edge. The convective growth time τ is the finite time for the effect at the far edge to reach the front edge of the plasma.

In an inhomogeneous plasma the study of the instability becomes much more complicated, primarily because the wavevector matching condition cannot be satisfied at all points in the plasma. This mismatch is best quantified by the derivative,

$$\kappa' = \frac{d}{dx}(k_o(x) - k_{epw}(x) - k_s(x))$$

which is zero for a homogeneous plasma. If the density varies linearly with x

$$n(x) = n_o(1 - x/L),$$

then

$$\omega_p^2(x) = \omega_{po}^2(1 - x/L).$$

It is easy to show, for perfect frequency matching, that a $\vec{k}$ mismatch

$$\kappa' = (\omega_p^2/2c^2L)(k_o^{-1} - k_s^{-1} - c^2m_e/k_{epw}3k_bT)$$

exists which is approximately (for $k_s \neq 0$)

$$\kappa' = \frac{\omega_p^2 m_e}{6Lk_b T k_{epw}}.$$

The absolute or convective nature of SRS is important since the thresholds which the various theories predict for the instability depend upon the assumed nature of the instability. These threshold conditions are quite different for the different theories. Also, for comparison to later experimental results, the spatial distribution of the fluctuations is important. For example, Rosenbluth [16] showed that in an infinite, inhomogeneous plasma only convective growth could be expected with a maximum intensity growth

$$I/I_o = \exp(2\pi\gamma_o^2/\kappa' v_{epw} v_-) \qquad 2-19.$$

This differs from the usual convective growth in that this level of growth is reached at all points where the instability occurs i.e. the fluctuations will be of uniform amplitude over some region of space. Rosenbluth's condition for this growth is that the term in the exponent divided by 2π should be greater than 1. On the other hand, Pesme [17] showed this convective growth only occurs for a plasma of length L $> \gamma_o/\kappa'(v_{epw}v_-)^{1/2}$ and absolute growth (at the reduced temporal rate) occurs if $(v_{epw}v_-)^{1/2} <$ L $< \gamma_o/\kappa'(v_{epw}v_-)^{1/2}$. Dubois [18] states that Rosenbluth and Pesme are both wrong and that an absolute instability occurs in any size of plasma provided $\gamma_o^2/\kappa' v_{epw} v_- > 1$. In this case, the growth rate will be given by

$$\gamma = [\frac{2\gamma_o}{\sqrt{v_{epw}v_-}}(1 - (\frac{\kappa' v_{epw} v_-}{\gamma_o^2})^{2/3}\pi^{-1/2}) - (\frac{\gamma_-}{v_-} + \frac{\gamma_{epw}}{v_{epw}})]\frac{v_{epw}v_-}{v_- - v_{epw}} \qquad 2-20.$$

This expression also includes a new effect. In a finite, homogeneous plasma, there is a threshold growth rate set by convective damping, namely,

$$\gamma_T \geq \frac{(v_- v_{epw})^{1/2}}{2}\left(\frac{\gamma_-}{v_-} + \frac{\gamma_p}{v_{epw}}\right) \qquad 2-21.$$

When the expressions for γ_o , κ' and the condition for absolute growth that Dubois uses are combined, the threshold for absolute growth in an inhomogeneous but finite plasma becomes

$$\frac{v_o^2}{c^2} > \frac{4(k_o - k_{epw})}{k_{epw}^2 L} \qquad 2-22.$$

Chambers [19] solved the coupled mode equations describing SRS numerically and pointed out that the nature of an instability is a function of both the plasma size and the assumed boundaries. He also showed that the electrostatic mode energy is not uniformly distributed over the interaction region but tends to be larger near the boundary. The exact point of maximum fluctuations depends upon the density gradient and the ratio of the group velocities of the waves generated. With several different theories to choose from, the best thing one can do is to wait until some experiments have been made and then decide which theory is correct. At $0.25 n_{cr}$, the threshold formula (eqn 2-22) is not valid since $k_s = 0$ and therefore κ' is infinite. Drake and Lee [20] have shown that at this density the threshold should be

$$\frac{v_o}{c} = \frac{0.52}{(k_o L)^{2/3}} \qquad 2-23.$$

A caveat should be placed on any prediction of final fluctuation level versus position. Nonlinear effects, which are responsible for the saturation of the instability, can affect the levels. The extent or importance of these effects is the subject of ongoing investigations.

So far only a three wave interaction has been considered and the plasma fluid parameters have been varied. There are competing wave-wave interactions which can have an effect on SRS. Interactions like SBS and two-plasmon decay and other processes in which the waves produced by SRS decay cascade in further decays are considered to estimate how they effect SRS.

The effects of mobile ions have so far been neglected. Stimulated Brillouin Scattering (SBS), which has a lower threshold and a lower growth rate than SRS does, can drive large amplitude ion acoustic waves in the plasma. These waves could disrupt SRS if the EPW generated by SRS scatters off these ion acoustic waves. Although the energy transfered is small ($\omega_{ia} \ll \omega_{epw}$), the EPW could be scattered in any direction. These scattered EPW cannot phase match properly with the pump wave and SRS is quenched. The two dimensional nature of this effect has never been fully discussed although results from one dimensional studies have shown it could be quite important. (The 2D nature results from the wave vector matching condition.) Damping of an EPW by an IAW has been considered by Dawson [21], Sagdeev [22], and in an early (1970) computer simulation [23].

The effects of the TPD instability [24] on SRS are now discussed. TPD has a slightly lower threshold than SRS does and has a similar growth rate. Its effect is twofold. It can drive large amplitude IA waves [25] which could act as those of SBS do. It can also modify the local density profile near quarter critical density [25,26], decreasing the scale length L. As L decreases, the threshold for SRS increases. At lower densities, L increases and perhaps the threshold intensity required at those densities decreases. This profile modification could be responsible for a gap in the scattered EM spectrum.

Secondary decay processes, in which the scattered EMW or EPW decay, have also been proposed as saturation mechansims for SRS. In particular, the electrostatic wave could decay into another EPW and an IAW. This process was considered

by Karttunen [27,28,29]. For $\omega_p^2/\omega_o^2 \leq 0.1$,the damping rate due to this decay is

$$\gamma_{decay}/\gamma_o = (\frac{c}{v_e})(\frac{4k_o c_s \omega_o}{\omega_p^2})E_{epw}/E_o \qquad 2-24.$$

For T=300eV, $n/n_{cr} = 0.1$ and Z=4, one finds for a CO_2 laser plasma that $\gamma_{decay}/\gamma_o = 0.5E_{epw}/E_o$. During the nonlinear evolution of SRS, there can be instances where $E_{epw} \geq E_o$ and thus, this effect might be quite important for the saturation of SRS.

Related to the mode coupling effects are what I call convective effects. Koch and Williams [30] have considered coupling between forward and backscattered EM waves in a density gradient. The forward scattered waves are reflected from their critical surface and propagate down the density gradient, triggering the instability at lower densities by increasing the EM noise level. A similar mechanism may be applicable to the plasma waves generated near quarter critical density although away from $0.25n_{cr}$ the EM waves travel much faster than the EPW do. The plasma waves generated by SRS will propagate forward up the density gradient and be reflected at their critical surface. The waves will subsequently propagate down the graident. This suggests that SRS should start at lower densities as time progreses. The rate at which it does so may be estimated by noting that

$$dn/dt \approx (\partial n/\partial x)(dx/dt) \qquad 2-25$$

where dn/dx is related to the density scale length and dx/dt is v_{epw}. This effect should be kept in mind when the experimental data are examined.

The fluid model uses an average electron velocity. There are instances where the actual distribution of electron velocities is important. For example, Landau damping is sensitive to $\partial f/\partial \vec{v}$ evaluated at the phase velocity of the wave. The quoted formula, eqn 2-14, is derived under the assumption that the distribution of electron velocities was Maxwellian. Since fast high energy electrons are generated

with $v \approx v_{ph}$, the distribution function at v_{ph} may be modified. Estabrook [2] has shown that more plasma wave damping does occur. If the hot electrons have a Maxwellian distribution, the total rate is

$$\frac{\gamma_L}{\omega_{epw}} = (\frac{\pi}{8})^{1/2}\frac{v_{epw}}{v_e}(\frac{k_d}{k})^2(\frac{n_c}{n_T}\exp\{-.5(\frac{v_{epw}}{v_e})^2\} + (\frac{T}{T_{Hot}})^{3/2}\frac{n_{Hot}}{n_T}\exp\{-0.5(\frac{v_{epw}}{v_e})^2(\frac{T}{2T_{Hot}})\} \qquad 2-26$$

where n_c is number of cold electrons, n_{Hot} is the number of fast electrons, $n_T = n_c + n_{Hot}$ and T_{Hot} is the fast electron temperature. If T_{Hot} is too large, a relativistic particle distribution should be used in place of the ordinary Maxwellian distributions employed to derive the formula quoted.

The effects of any static (or quasistatic on γ_o^{-1} time scales) magnetic fields on SRS have been neglected in the discussion so far. The effects of such a magnetic field on SRS have been considered [35,36,37,38,39]. In the simplest case, SRS generates scattered light at the frequencies

$$\omega_s = \omega_o/2 \pm \Omega_c/4 \qquad 2-27$$

and its growth rate changes to

$$\gamma = \gamma_o(1 \pm 3\Omega_c/\omega_o) \qquad 2-28$$

where $\gamma_o \ll \Omega_c$ and $n = 0.25n_{cr}$ have been assumed. Ω_c is the electron cyclotron frequency. The scattered light is circularly polarized.

Many mechanisms can generate large magnetic fields in a laser- produced plasma, the most common being the macroscopic $\nabla n_e \times \nabla T_e$ source. The electric force in a plasma is balanced by a electron pressure gradient i.e. $n_e e\vec{E} = (\nabla p)$. If this electric field is substituted into Faraday's law and if the plasma behaves like an

ideal gas, the $\nabla n_e \times \nabla T_e$ magnetic field results. A simple estimate of the saturated field due to this mechanism was made by Max *et al.* [34] who showed

$$B_{max}(MGauss) = 36(T(keV))^{1/2}\frac{1}{L(\mu m)}\left(\frac{A}{Z+1}\right)^{1/2}.$$

For T = 300eV, L (the density scale length) = 300 μm, A (the atomic weight) = 14 and Z (the average charge) = 4, a field of 100 kG might be generated. The magnetic field which is a result of this mechanism will be torodial in shape with the axis of the torus along the laser axis. (A pulse of fast electrons is equivalent to a current and could also generate a large magnetic field.)

Particle trapping [31,32,33] in the electrostatic wave potential can generate high energy electrons. Trapping occurs for electrons whose velocities v are such that

$$0.5m_e v_{ph}^2 - e\phi < 0.5m_e v^2 < 0.5m_e v_{ph}^2 + e\phi$$

where the density fluctuation level (δn) is related to the electrostatic potential amplitude, ϕ, by the Fourier transformed Poisson equation

$$\delta n/n_o = \phi k^2/4\pi n_o e.$$

(This condition is not the usual condition for trapping which is $0.5m_e(v-v_{ph})^2 \leq e\phi$. If this is used a linear dependence of N on $\delta n^{1/2}$ instead of δn is obtained.) In a Maxwellian plasma there will always be some trapping. We can make a simple model for estimating the number of hot electrons generated by trapping. We assume that a constant fraction, f, of the electrons with energies between $0.5m(\omega/k)^2 + e\phi$ and $0.5m(\omega/k)^2 - e\phi$ are trapped by the wave potential, converted to high energy electrons, and subsequently detected. If the background plasma has a Maxwellian

distribution of velocities, the number of fast electrons produced will be

$$N_e = f n_o [\mathrm{erf}(x_+) - \mathrm{erf}(x_-)]$$

where

$$x_\pm^2 = 0.5m(\omega/k)^2/k_BT \pm e\phi/k_BT.$$

We can let x_+ go to infinity, provided $e\phi/k_BT \gg 1$. Because $x_- \gg 1$, we can use the asymptotic expansion for the resulting erfc x_- to arrive at

$$N_e = f n_o \exp(-x_-^2)/(\sqrt{\pi} x_-)$$

or

$$\ln N_e = \ln(f n_o/(\sqrt{\pi} x_-)) - x_-^2.$$

The first term on the RHS is effectively constant. Substituting the definition of x_-^2 and using ϕ from the Fourier transformed Poisson equation we find

$$\ln(N_e) = (4\pi e^2 n_o/k^2 k_B T)(\delta n/n_o) + C \qquad 2-29$$

where C is a constant. This relationship can be confirmed if the fluctuation level and the number of fast electrons are simultaneously measured.

2.5 Connection between the Infrared Reflectivity and the Fluctuation Levels

An electron density perturbation of depth $\delta n/n$ can scatter an electromagnetic wave. The level of the scattered light can be estimated with several approximate formulas. For the sake of discussion, suppose that a fluctuation level has been established and has been saturated by some unspecified mechanism. If the scattering is sufficiently weak, the amount of scattered light can be found using normal scattering theories. In this case, the level is considered due to Thomson scattering.

(This is the same scattering process that is used for diagnostic purposes. Here, it is the incident CO_2 laser light and not the probe ruby laser light which is scattered.) The scattered power, P_s, into solid angle $d\Omega$ in frequency range $d\omega$ is given by

$$\frac{1}{P_i}\frac{dP_s}{d\Omega d\omega} = nDS(\vec{k},\omega)r_e^2/(2\pi)$$

where

$$S(\vec{k},\omega) = \frac{1}{VT}\left[\frac{\delta n(\vec{k},\omega)}{n}\right]^2,$$

D is the length of the plasma, T is the time of observation, and V is the volume containing the plasma waves. This reduces to a reflectivity (for a single epw) of [40]

$$R = r_e^2\lambda_o^2 D^2(\delta n/n)^2/4 \qquad 2-30$$

where the scattered power is radiated back into the solid angle subtended by the incident laser beam. $r_e = e^2/(m_e c^2)$ is the classical electron radius. If the scattering is sufficiently strong, however, this formula must break down. (To see this, consider the $D \to \infty$ limit.) In this case, the coupling of the incident laser with the plasma must be considered more carefully. Vinogradov [41] has done so and found a non-linear reflectivity from a plasma. Kruer [42] has derived the same result and provided more detail on how it was found. The result for waves propagating in one spatial direction is R=$\tanh^2(\alpha D(\delta n/n))$ where α is the coupling constant between the vector potential of the incident EM wave and the plasma fluctuation, $\delta n/n$. Substituting the expression for α, we get

$$R = \tanh^2\frac{\pi}{2}\frac{\delta n}{n}\frac{D}{\lambda_o}\frac{n}{n_{cr}}\left(1-\frac{n}{n_{cr}}\right)^{-1/2} \qquad 2-31.$$

This result has the correct physical limits $R \to 0$ as $D \to 0$ and $R \to 1$ as $D \to \infty$. It also reduces to the normal Thomson scattering formula for weak scattering (when

the approximation tanh(x) = x is valid). There is also a correction for the refractive index of the medium which is usually ignored in the normal Thomson scattering formula. If the beam is fully coupled into the medium, the Manley-Rowe relations can be used to deduce a reflectivity. This is the largest limit since there cannot be 100% reflection from a density fluctuation if, for no other reason, conservation of action density ($n\hbar$) must be attained. (See the original justification of these relations in section 2-2.) The Manley-Rowe method uses an estimate of how much energy, U_{epw}, is contained in the plasma waves. This energy is just

$$U_{epw} = E^2 V/(8\pi)$$

where E is the electric field associated with a electron density fluctuation,

$$E = 4\pi e^2 \delta n/(k n_o)$$

and V is the volume containing the plasma waves. The amount of scattered infrared light is then

$$U_{scat} = U_{epw}\omega_s/\omega_{epw} \qquad 2-32.$$

The reflectivity R = U_{scat}/U_{inc} where U_{inc} is the amount of incident energy in the laser pulse.

2.6 Computer Simulations

SRS is straightforward only if many simplifying (and sometimes unrealistic) assumptions are made. Computer simulations which follow the temporal evolution of SRS are necessary, sometimes providing insight before analytic models are available. This section briefly describes how simulations are performed. Some results pertaining to this work are highlighted.

A collection of electrons and ions is placed in some region of space and the dynamics of these two species are followed by solving Maxwell's equations. (If there is no initial electromagnetic wave, the problem is called electrostatic.) If the number of particles becomes too large, computer solutions cannot be used since the number of interactions goes as N^2. Simplifying assumptions must be made. Two types of approach are common, the particle in cell (PIC) codes [43] and the Vlasov codes.

Most simulations have been made using the PIC method. This method divides the particles into cells by a mesh. The fields on the mesh are found by summing the fields due all the individual particles. Each particle within a cell is moved by the field at its position found by interpolation of the fields at the mesh boundaries of the cell. The procedure is repeated and the simulation progresses. Typical simulations would have 60000 particles and 60 cells.

The second approach involves the solution of Vlasov's equation and Maxwell's equations. In this method, it is the particle distribution which is followed. An approximation, the waterbag model, in which the boundaries of a uniform distribution are followed, make this way potentially much faster.

Common to both approaches are problems associated with infinite (periodic) versus finite plasmas and one versus two dimensional effects. In addition, relativistic efffects must be included as the velocities of some of the particles can be large.

Early simulations [44] in infinite, homogeneous plasmas showed that the threshold and growth rates analytically calculated are quite good. Other simulations [45] have shown that density scale lengths, background temperature, plasma noise levels and damping of waves play important roles in determining thresholds for SRS. When experiments are compared to the simulations, one should remain aware of the fact that simulations are only an approximation to reality. Several of the aforementioned effects could be present in an experiment, whereas simulations are usually restricted to examining the effect of one or two of them.

Simulations (usual 1-D) [32,44] identified two saturation mechanisms, pump depletion (discussed earlier) and fast electron generation. The generation of fast electrons is a damping mechanism as the energy is removed from the EPW and transferred to kinetic energy in the electrons. The fast electrons have a velocity distribution which appears Maxwellian with a temperature given approximately by $k_bT = 0.5m_ev_{ph}^2$. v_{ph} depends primarily on the plasma density but there is a temperature dependence that simulations [1] show is important for $T > 1$keV. Up to 2% of the electrons in the plasma could be converted to fast ones.

Other simulations [25,26] have identified further saturation mechanisms. Two dimensional simulations showed profile modification due to TPD (or SRS) and mode coupling to ion acoustic waves are important. Both mechanisms have a common origin. In TPD, two large amplitude epw are generated, $\vec{E}_{1,2} = \vec{E}_{1o,2o}\cos(\vec{k}_{1,2}\cdot\vec{r} - \omega_{1,2}t)$. The total energy density, given by the square of the total electric field, is given by

$$\vec{E}^2 = \vec{E}_{1o}^2 + \vec{E}_{2o}^2 - \vec{E}_{1o}\cdot\vec{E}_{2o}[\cos((\vec{k}_1-\vec{k}_2)\cdot\vec{r} - (\omega_1-\omega_2)t) + \cos((\vec{k}_1+\vec{k}_2)\cdot\vec{r} - (\omega_1+\omega_2)t)].$$

The pondermotive force is proportional to $\nabla\vec{E}^2$. The term $\nabla(\vec{E}_{1o}^2 + \vec{E}_{2o}^2)$ is responsible for modifying the plasma density near quarter critical. This profile modification is clearly seen in figure 2-5 which is reproduced from Langdon[26]. The second term, $\nabla(\vec{E}_1\cdot\vec{E}_2)$, will time average to zero unless $\omega_1 - \omega_2 \approx 0$ or at least is much less than ω_p. Ion acoustic waves, whose frequencies are much less than ω_p, could be excited by this means at $\vec{k}_{ia} = \vec{k}_1 - \vec{k}_2$. These ion waves were seen in the same simulations which found the profile modification.

A self-generated magnetic field found in yet another simulation [2] affects SRS by disrupting the transport of hot electrons. As Estabrook points out, reducing the hot electron transport increases the local hot electron density. The increased density leads to increased damping (see eqn 2-26).

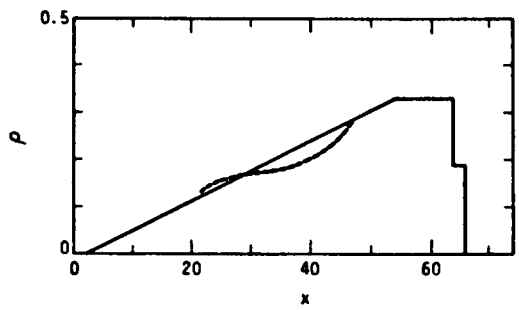

Figure 2-5 Density scale length decrease at $0.25n_{cr}$. Notice the shelf at lower densities.

One observable effect suggested by simulations [44] is, for light scattered from $0.25n_{cr}$, that the EM spectrum should show harmonics $\omega_o/2 + m\omega_o$ where m is an integer. (Similar behaviour is also expected as an indirect result of the TPD instability.) These harmonics were suppressed in the earlier theory when the higher order couplings were ignored. The simulations do not have this restriction and show that these couplings are present.

One interesting simulation [46] was done in 2-D. In it, SRS backscatter is seen to evolve into SRS sidescatter. This occurs because , as the plasma heats up , the EPW with the longest wavevectors become more damped. Since the EPW with the longest wavevector is the one responsible for direct backscatter, the shorter ones are obviously those responsible for side (and eventually forward) scatter. This effect is negligible for our plasma since the simulation showed it is not important in cool ($<$ 1 keV) plasmas.

CHAPTER 3

Experimental Details

In this chapter, the facilities used to generate a plasma and the diagnostics used to measure SRS-generated effects are described. These diagnostics include Thomson scattering to examine the plasma waves, infrared spectroscopy and an electron spectrometer. In addition, the methods of analysis of the results are outlined.

3.1 Laser and Target Characteristics

The study of parametric instabilities requires a system capable of generating a large v_o. (Remember that v_o is the velocity at which an electron oscillates in the electric field of the incident laser light.) Since v_o^2 is proportional to $I\lambda^2$, either a long wavelength or a high intensity must be used. A CO_2 laser with $\lambda = 10.6\mu m$ is ideal since a large v_o can be generated at modest intensities. In addition, n_{cr} for $10.6\mu m$ radiation is low so that visible light diagnostics (primarily Thomson scattering and interferometry) can be used without any absorption or refraction effects on the probe light. (Remember that n_{cr} is the electron number density at which the plasma frequency equals the incident laser frequency.)

The CO_2 laser has been described elsewhere [47,48,49] and is only outlined here. The physical layout of the system and essential operating parameters are shown in figure 3-1. The system consists of a hybrid oscillator, from which a 2 nanosecond pulse is electro-optically switched out using a Pockels cell, and 3 amplifiers which

increase the pulse energy to near 10 Joules. The switchout aspect is important since the electrical pulse used for this also triggers low jitter diagnostics such as a ruby laser [50,51], a Hamamatsu Temporal Disperser Model C1370-01 (streak camera), and a Tektronix 7104 oscilloscope. Other than routine maintenance changes, the system has remained identical to that described by Bernard [48] except that provision for changing the plane of polarization (defined by the plane containing $\vec{E}$ and $\vec{k}$) has been introduced. Previously, the plane of polarization was vertical at the target, but using a two mirror system it was changed to horizontal. The state of polarization was conveniently changed by the insertion of a quarterwave CdS plate (to give circular polarization) or a halfwave plate (to change linearly vertical to linearly horizontal polarization) after the final Ge flat on the hybrid table. For the spatially resolved Thomson scattering and the narrow range (4°) wavevector (k) resolved Thomson scattering, the plane of polarization was vertical. For the wide angle (18°) k resolved Thomson scattering, the frequency resolved Thomson scattering, and the IR measurements, the plane was horizontal. Circular polarization, although an option, was never used.

The target used was similar to that set up by Popil [52]. It is a pulsed nitrogen gas jet stabilized to laminar flow by a helium background [53]. The plasma which forms is subcritical ($n_{max} \approx 0.4 n_{cr}$) and has a time averaged temperature of 300 eV. The target chamber surrounding the jet was replaced by one with which diagnostics could be more easily performed. A new focussing lens was used. Previously, a symmetric biconvex KCl lens was used, whereas now, a KCl lens designed for minimum spherical aberration is used. The first lens was used for the spatially resolved Thomson scattering only. A schematic outline of the target (given in figure 3-2) shows the size of the jet relative to the incident laser beam and subsequent plasma. The plasma forms in two regions which correspond to the edges of the jet. The height at which the laser strikes the jet varies by $\pm$ 2 mm. The neutral gas

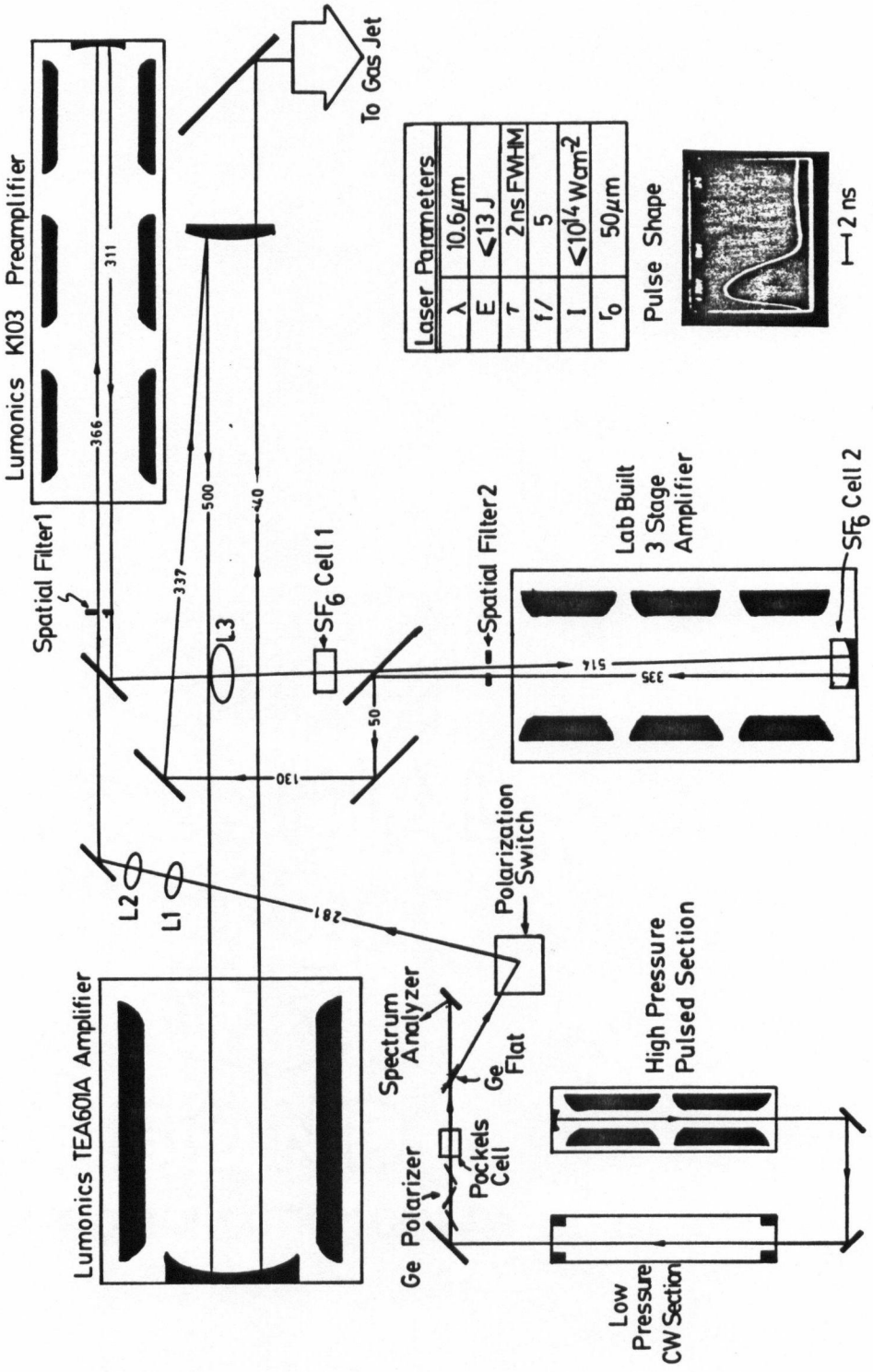

Figure 3-1 Layout of the CO_2 laser system. Typical performance parameters are shown

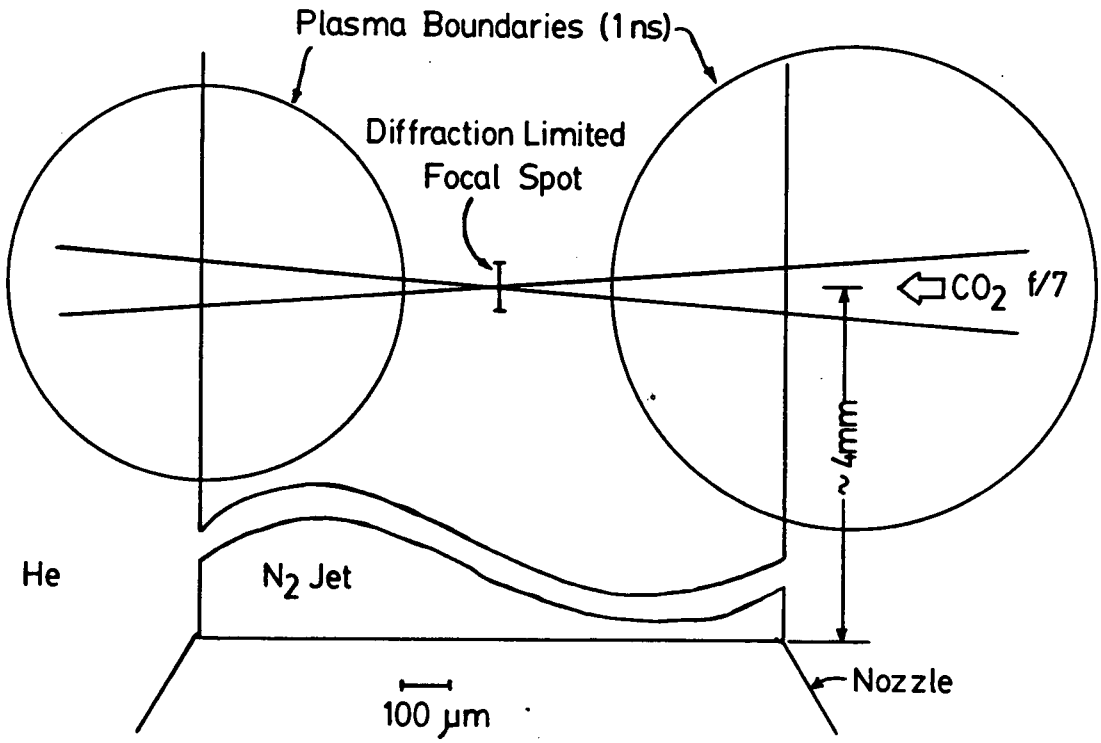

Figure 3-2 Gas jet target drawn to scale.

jet density and structure is uniform over such a variation in height and thus, this variation is thought to be unimportant.

Temporally and spatially integrated optical spectra of the plasma light indicate the presence of numerous N I and He I lines. N I lines are expected, but He I lines indicate that the gas outside the jet is breaking down. In this outside background plasma most of the SBS observed by Bernard [54] occurs.

A different type of gas jet was briefly examined. This jet, a He jet in a He background, was expected to have similar densities to those of the N_2 jet (confirmed by interferometry). Of course, there will be considerable difference in ion mass and it was explained in chapter 2 that the ions are important in determining the

saturation of the TPD instability. The structure of the N_2 jet was determined optically but the structure of the new jet cannot be studied by that method as the index of refraction for He is much smaller than that of N_2. A different method was used. A glow discharge between two small (1 cm by 2.5 cm) parallel steel electrodes separated by 3 cm was established in the background gas . The electrodes were oriented parallel to the gas jet. The gas jet was fired and the resulting glow in the jet was imaged through an image intensifier and photographed on Polaroid film. A shutter was used to control the time of exposure relative to the firing of the jet and also to control the length of the exposure. In figure 3-3, the gas jet structure can easily be recognized and appears to be laminar.

3.2 Thomson Scattering

Thomson scattering was used to examine the EPW fluctuations directly. Since the bulk of the important results to be presented were derived from this diagnostic, a short discussion of the background of the technique is given. The outline given closely follows the introductory chapters of Sheffield [56].

When an individual electron is accelerated in the field of an electromagnetic field $\vec{E}_o$, it radiates in the far field a dipole pattern. The field at an observer ($\vec{E}_s$) is proportional to

$$\frac{\hat{s} \times (\hat{s} \times \vec{E}_o)}{R}$$

where $\hat{s} = \vec{R}/r$ and $\vec{R}$ joins the observation point to the source origin. When there are many electrons, the far field pattern is a superposition of the effects of each electron with corrections for the retarded time differences and source phase differences at the individual electrons in plasma. This gives rise to a power pattern

$$P_s(\vec{R},\omega_s)d\Omega d\omega_s = \frac{cd\Omega}{4\pi^2}\lim_{T\to\infty}\frac{d\omega_s}{T}\Big[\int_{-T}^{T} dt \frac{e^2}{m_e c^2}\hat{s}\times(\hat{s}\times\vec{E}_{io})$$
$$\int_{Vol} d\vec{r} n_e(\vec{r},t)\exp(-i\omega_s(t-\hat{s}\cdot\vec{r}/c+R/c))\cos(\vec{k}_i\cdot\vec{r}-\omega_i t)\Big]^2.$$

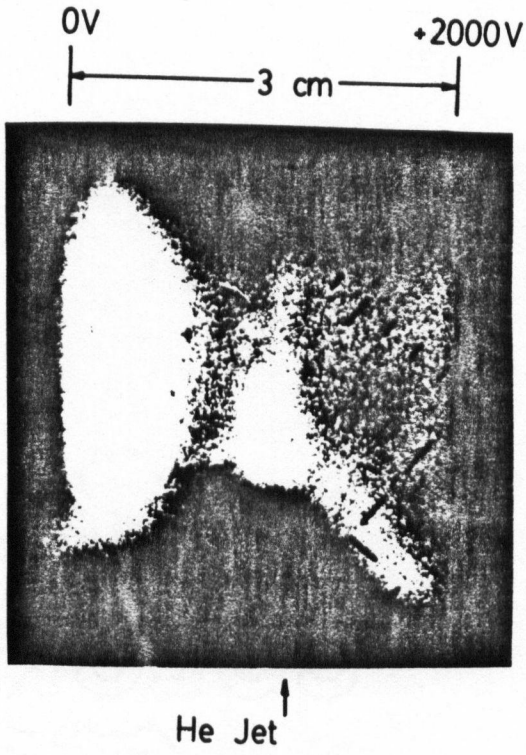

Figure 3-3 Laminar structure in the He jet. The bright glow to the left is the cathode glow in front of one of the electrodes. The direction and position of gas flow is indicated by the arrow.

n_e is the source weighting, the exponential term contains the retarded time factor and the cos term is the phase difference at the source. n_e is given by

$$n_e(\vec{r},t) = (\int \frac{d\vec{k}}{(2\pi)^4} \int d\omega n_e(\vec{k},\omega) \exp(-i(\vec{k}\cdot\vec{r} - \omega t)).$$

There are two terms (+ or −) in the exponentials which reduce to

$$i[(\omega - (\omega_s \pm \omega_i))t - (\vec{k} - (\omega_s\hat{s}/c \pm \vec{k}_i))\cdot\vec{r} - \omega_s R/c].$$

If an experiment is set up and a signal is observed at frequency ω_s and at an angle θ to the incident probe beam, it does not follow that the $\vec{k}$ is that calculated from $\vec{k} = \vec{k}_s - \vec{k}_i$. The response to a given wave is not a δ-function unless an infinite length of the wave is probed. If a finite segment is probed using Thomson scattering (or indeed, any scattering) there will be typically a sinc^2 type response. A monochromatic wave can give rise to a finite cone of rays. To see this consider the integrations which have to be performed to derive a δ function response. The integration over time reduces to $\delta(\omega - (\omega_s \pm \omega_i))$. At this point an integration over volume is usually performed to give $\delta(\vec{k} - (\vec{k}_s \pm \vec{k}_i))$. If we are dealing with a finite volume, this is not valid and the resulting scattered light will have some spread. Considering only $\vec{k}$ integration we get

$$P(\vec{R}) \propto \int_{\vec{k}} \int_{Vol} d\vec{k} d\vec{r} n_e(\vec{k}, \omega) \exp(i(\vec{k} - (\omega \hat{s}/c \pm \vec{k}_i)) \cdot \vec{r}).$$

Assume that $n_e(\vec{k}, \omega)$ is a slowly varying function of k. Then

$$P(\vec{R}) \propto n_e \mathrm{sinc}^2(k_z L_z) \mathrm{sinc}^2(k_x L_x) \mathrm{sinc}^2(k_y L_y),$$

where

$$k_{x,y,z} = (\vec{k} - (\omega_s \hat{s}/c \pm \vec{k}_i))_{x,y,z},$$

and a rectangular volume of plasma was assumed. It is only the finite scattering volume which gives rise to this diffraction effect.

Figure 3-4 shows a two dimensional representation of the scattering from a finite segment of plasma. Contours in k space (arbitrarily drawn) show the locii of directions of equal scattered intensity. The maximum intensity occurs when $\vec{k}_s = \vec{k}_i + \vec{k}$. (Only the + case is shown.) The exact angular extent depends upon

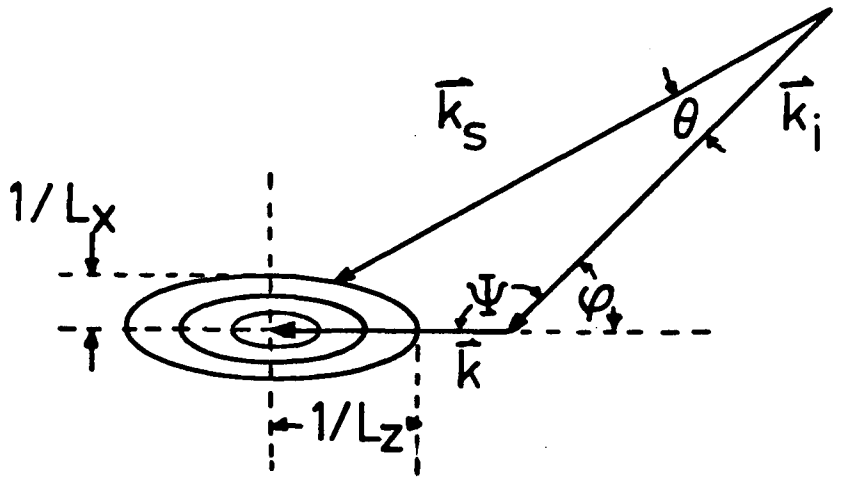

Figure 3-4 Two dimensional representation of scattering from a finite volume. The contours are arbitrary.

the scale lengths in the x and z directions, the angle of incidence, and length of k. The maximum angular extent will be

$$\pm\Delta\theta_1 \approx \frac{\sqrt{(\delta k_x)^2 + (\delta k_z)^2}}{k_i} \approx \frac{\lambda_r}{L}, \qquad 3-1$$

where

$$\delta k_{x,z} = \frac{1}{L_{x,z}} \quad .$$

For $L = 200\mu$m, an uncertainty of 0.2°results (FW).

If $L_{x,z} \rightarrow \infty$, there could still be a finite angular range of scattering if either $\vec{k}$ or $\vec{k}_i$ were not fixed. In a real experiment there will be a range of $\vec{k}_i$ due to the finite cone angle of the incident probe beam. This effect was minimized by imaging the vertical focal plane of the lens onto the slit of the streak camera. The distribution of light in the focal plane of a lens is related to the Fourier transform of the object [57] which in this case is the plasma. To be precise, in the present case, this is true only for directions parallel to the incident CO_2 laser beam because of the astigmatic

nature of the focussing used. One imagines the light scattered from the plasma to be a superposition of many cylindrical waves each of which is converging to a different line in the focal plane of the lens. If there were no plasma present, there would be a single cylindrical wave converging to a line. Because of the finite size of the lens the wave does not converge to a line, but rather gives rise to the usual single slit diffraction pattern. A similar pattern will be found for each of the converging waves which make up the light scattered from a plasma. In the present case, the angular error due to this pattern for light which passes through an f/100 lens at 694.3nm is about 0.01 radians, a small angle when compared to the scattering angles and thus will be ignored. In any other plane the diffraction patterns will be spread out and may overlap thereby reducing the angular resolution.

There are additional effects which can give rise to a finite range of scattering angles. These are best understood if we assume that an infinite length of the plasma wave is probed (thereby eliminating the finite length effect) and that the incident probe beam is a plane wave (thereby eliminating the finite angle effect of this beam). If we are considering the probing of a plasma with no *a priori* assumptions about the waves, then the frequency of the scattered light at a given angle must be well known in order to deduce the $\vec{k}$ of the plasma wave. However, there will always be a finite frequency spread of the scattered light which will result in an uncertainty in $\vec{k}_s$ along the direction of scatter of $\Delta\omega_s/c$. This results in an uncertainty of the plasma $\vec{k}$ doing the scattering. This uncertainty is shown in figure 3-4

In principle, if both the frequency and direction of the scattered probe light are known, the plasma wave probed is fixed and there should be no further complications. In practice there remains one problem that can give rise to a finite angle of scattered light. The incident laser beam is effectively composed of plane waves with k= constant but propagating at a range of angles to the beam axis. Within the cone angle of a laser, an angular spread $\pm\Delta\Psi$ in the direction of $\vec{k}$ is possible.

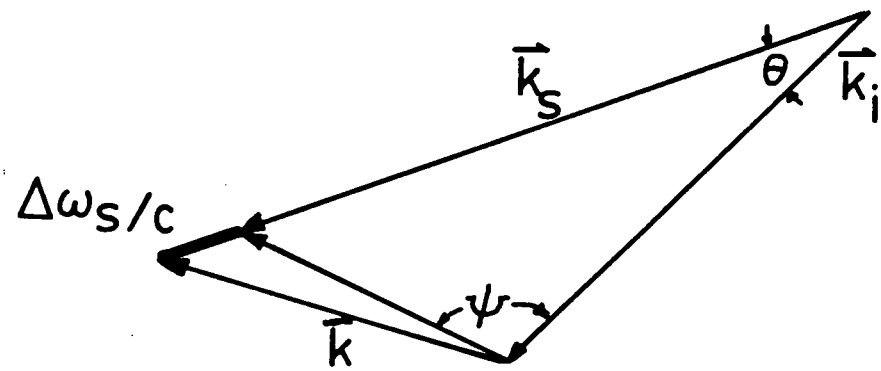

Figure 3-5 Uncertainty in k due to a finite $\Delta\omega_s$.

Simple trigonometry and calculus shows that this gives rise to an angular range in $\vec{k}_s$ of

$$\pm\Delta\theta_2 = \frac{k}{k_i}\frac{\cos\Psi}{\cos\theta}\Delta\Psi \qquad 3-2$$

where Ψ is angle between the incident probe and the CO_2 laser beam axis. This reduces to an FW uncertainty of 0.2°for $\Psi = 124°$and $\theta = 3°$.

The total angular uncertainty shown in the data presented (e.g. Fig.4- 6) is the sum in quadrature of the finite volume effect (Eqn.3-1) and the finite cone angle effect (Eqn.3-2).

Four different variations on Thomson scattering were performed: one spatially, two k-vector resolved and one frequency resolved. In each case, the frequency and wavevector matching conditions were chosen such that SRS driven EPW were observable. The frequency selection condition was obtained by using an interference filter which passes 670 nm light in an 11 nm FWHM passband. The frequency shift expected for light (blueshifted) from $0.25n_{cr}$ would give the scattered light a wavelength of 672.3 nm which is well within the passband. Light scattered from lower densities would have longer wavelengths. SBS scattered light and stray ruby

light both have wavelengths near 694.3 nm which is well outside the passband. Two filters were used in most cases. A second filter, a 694.3 nm filter tilted to 26°, had wider passband but still effectively rejected unshifted probe light. This combination of filters provided a signal to noise ratio of more than 10^4.

The k vector matching was obtained by a judicious choice of incident probe beam angle and scattered angles. The length of the incident probe wavevector is ω_{Ruby}/c while that of the scattered light is $(\omega_{Ruby} + \omega_p)/c$. The length of the EPW wavevector generated at $0.25n_{cr}$ is $\sqrt{3}\omega_o/2c$. Since these vectors sum to zero, elementary geometry yields

$$\cos\theta = (k_{epw}^2 - k_{Ruby}^2 - k_{Scat}^2)/(-2k_{Ruby}k_{Scat})$$

and

$$\sin\Psi = k_{Scat}\sin\theta/k_{epw}$$

where θ is the angle between the incident and scattered probe light and Ψ is the angle between the incident probe and the epw. Ψ was set assuming the EPW generated at $0.25n_{cr}$ was parallel to the incident CO_2 laser beam. Ψ was 124° while θ for $0.25n_{cr}$ was 2.6°. (Many previous Thomson scattering setups assume that $k_{Ruby} = k_{Scat}$, i.e., no frequency shift, in which case

$$\cos\theta = 1 - k_{epw}^2/2k_{Ruby}^2.$$

This shift cannot be ignored in this case since the difference in length between the incident and scattered ruby wavevector lengths, although small, is comparable to the length of the plasma wavevector probed. This means the scattering geometry must be carefully setup.)

The spatially resolved Thomson scattering was performed to determine where SRS occurred and to obtain some idea of the size of this region. In this experiment the plasma was magnified by a factor of 8 and imaged onto the slit of the streak camera. A mask was used to limit the angular extent of the scattered probe light imaged to 2.6–4.5°which corresponds to wavevectors expected to be present at densities in the range 0.15-0.25n_{cr}. The frequency range was limited by the aforementioned interference filters.

Since we are observing a 2-D region from an angle, there are projection effects which cause a distance perpendicular to incident CO_2 beam to be observed as a length. Consider figure 3-6 where two extreme cases are shown which both give rise to the same observed width W. To obtain a length l (in the direction of the CO_2 laser), a width w (perpendicular to the CO_2) is needed. Physically, w is limited to a maximum size by the size of the CO_2 laser beam i.e. $2r_o$ and a minimum size of zero. For a given W, l is limited in length. In the streak records presented, w has been assumed to be 0 and thus l is overestimated. If w is set to the maximum value, the observed l are generally reduced by about a third.

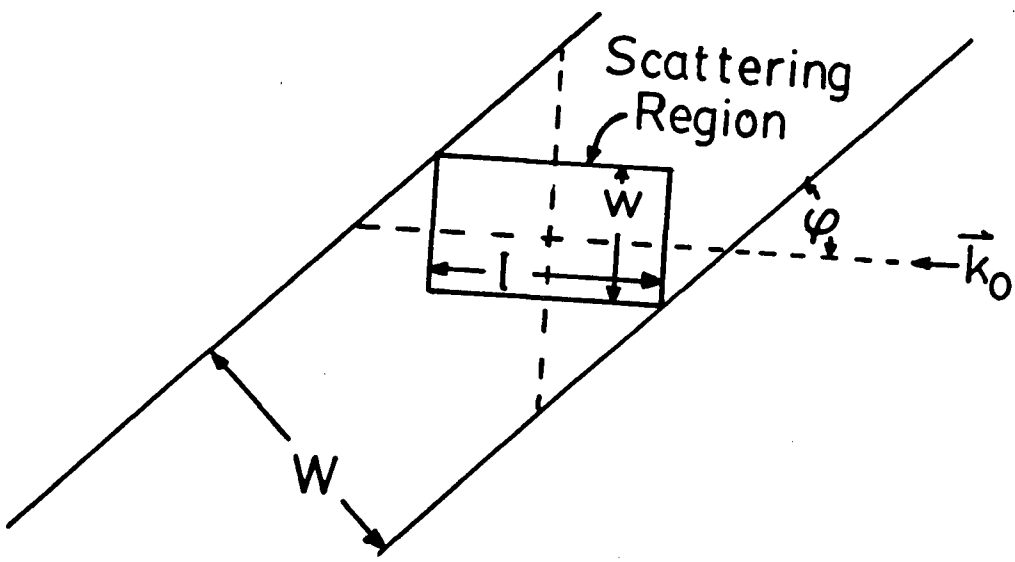

Figure 3-6 Projection effects on spatial Thomson scattering.

Two wavevector (k) resolved scattering experiments were set up which are outlined in figures 3-7 and 3-8. In the first experiment, only a limited angular range (2-4.5°) was imaged whereas in the the second experiment a much wider range (2-18°) was imaged. The first case will be described in some detail as the bulk of the results in this thesis were obtained from this experiment. An incident ruby laser pulse of 6ns duration was focussed astigmatically using a f/100 glass lens to a horizontal focus at the gas jet which is 3 mm wide and to a vertical focus 30 cm beyond the jet, where it is dumped into a stacked razor blade pile. The incident CO_2 laser beam focal volume and the ruby laser beam were aligned by forming a pinhole in an Al foil target located at the jet, centering the ruby laser alignment HeNe laser onto this pinhole and using the light diffracted through the pinhole to align the optics to the streak camera. For rough alignment, a second HeNe laser which simulated the scattered probe light was used. The Fourier transform plane, the plane at which the vertical focus was located, was imaged onto the streak camera slit. A mask located in this plane limited the angular range. The mask also limited the wavevectors to those within the cone angle of the CO_2 laser in the direction perpendicular to that resolved at the slit. The two interference filters were included to limit the frequency of the scattered light and to reduce stray probe and plasma light noise. A cylindrical lens was positioned in front of the streak camera slit so that the plasma was imaged onto the slit for directions perpendicular to the slit ; this lens would not affect any image along the slit other than translating it in space. In figure 3-7, the upper inset shows the relative sizes of the incident ruby, CO_2 and slit image at the jet. The arrangement of their sizes permitted the maximum signal to be gathered. A fiducial signal was guided to the the camera from the ruby laser to provide a record of any fluctuations in the ruby laser intensity incident upon the jet. The optical path lengths of the incident ruby laser pulse and the fiducial pulse were arranged so that both pulses were coincident at the streak camera slit.

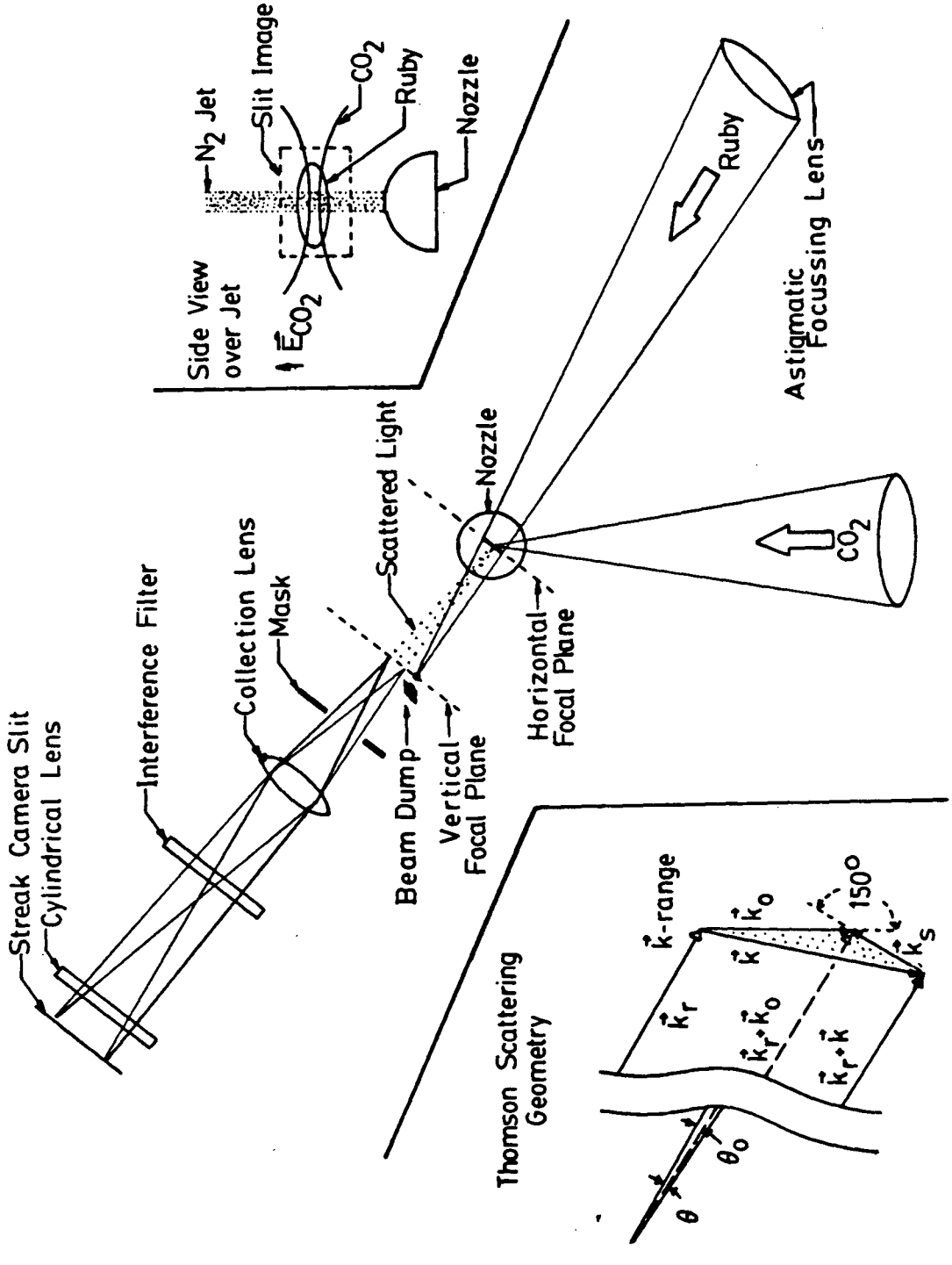

Figure 3-7 Narrow angle k resolved Thomson scattering.

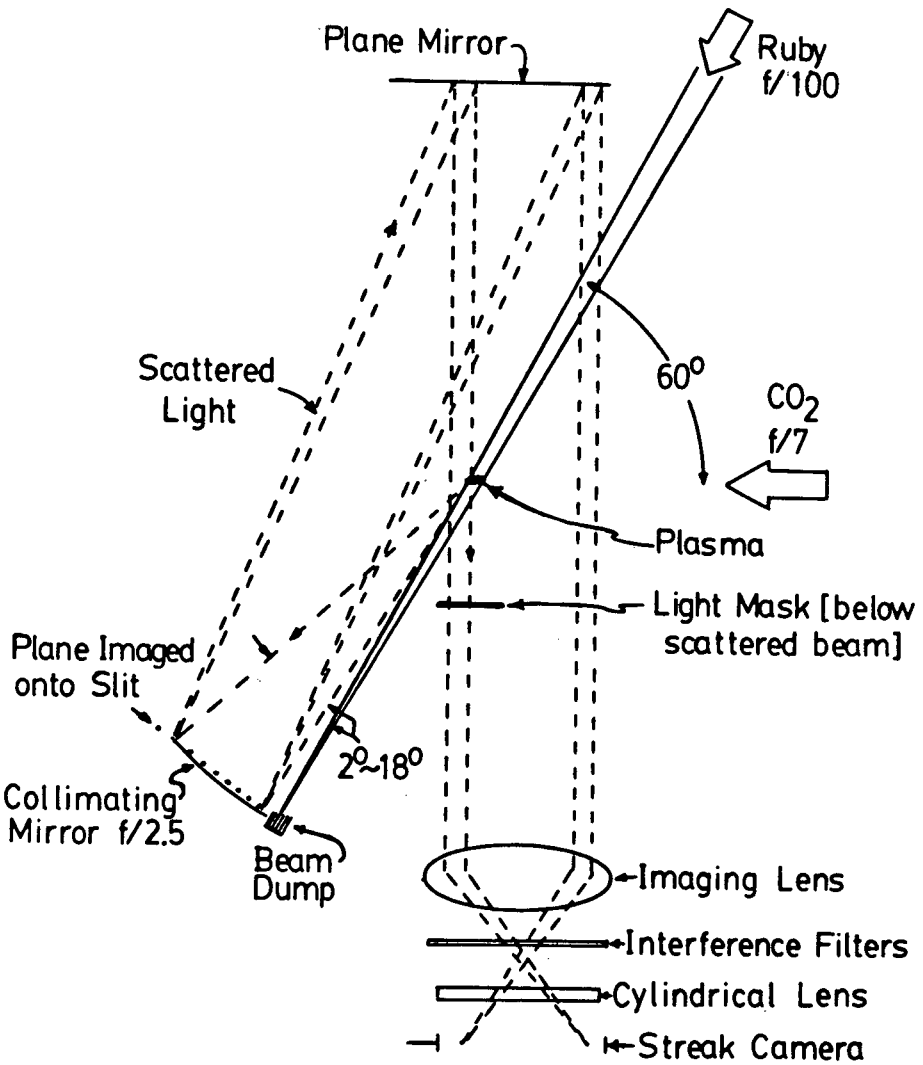

Figure 3-8 Wide angle k resolved Thomson scattering.

The optical system was calibrated absolutely using a Fresnel diffraction technique. Since this method is somewhat unusual, it will be described in detail. The technique relies upon Fresnel diffraction from a straight edge into the geometric shadow (dark) zone. A straight edge (razor blade) was placed vertically at the jet. The light imaged onto the streak camera was the light diffracted into the dark zone by this edge. The ruby laser was attenuated using neutral density filters by factors of 10^4 before and 10 after the straight edge. The resulting diffraction pattern was streaked and analyzed as follows.

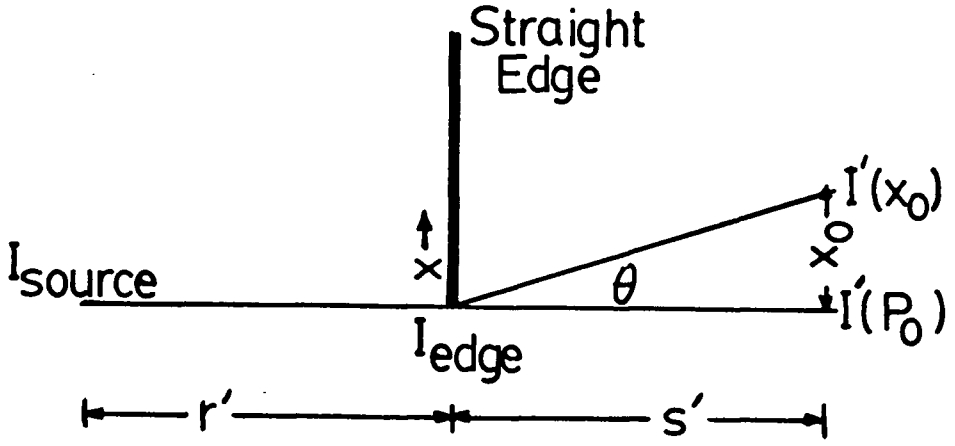

Figure 3-9 Fresnel diffraction geometry.

Diffraction theory [58] shows that

$$I(w) = [C(w)^2 + (1 - S(w))^2]I_o'$$

where C and S are the Fresnel cosine and sine integrals and

$$w = x\sqrt{\frac{2((r')^{-1} + (s')^{-1})}{\lambda}}.$$

The terms, r', s' and x are defined in figure 3-9. We are interested in large w where asymptotic expansions can be used to yield

$$I(w) = 2I_o'/\pi w^2.$$

It is also usual to calculate I for the plane of observation. This entails multiplication by a scale factor (see Klein [59]) since

$$x/r' = x_o/(r' + s').$$

The intensity we want should also be normalized to that at the edge. Since

$$I_o'(P_o) = I_{Source}/(r' + s')$$

and

$$I_{edge} = I_{Source}/r',$$

it follows that

$$I_o'(P_o) = r' I_{edge}/(r' + s').$$

Substituting for I_o' and x in the expression for $I(w)$ we find

$$I(x_o) = \lambda I_{edge}(s'/x_o)^2/\pi s'$$

which reduces to

$$I(\theta)/I_{edge} \approx \lambda/\pi s' \tan^2\theta.$$

When comparing the derivation summarized above to a more complete derivation found in standard textbooks, it might be useful to note that our source is the second (vertical) focus located on the same side of the edge as the plane of observation. This has no effect on the results found above.

At a particular angle, θ_o, and in a range $\delta\theta$ an amount $I(\theta_o)/I_{edge}$ is detected by the streak camera and gives a signal N_1. Corresponding to this signal, the fiducial has a level N_2. Then any subsequent signal observed over the same angular range is relatively calibrated since

$$(I_{scat}/I_{edge})_{absolute} = (\lambda 10^{-N.D.}/\pi s' \tan^2\theta_o)\frac{N_{signal}}{N_1}\frac{N_2}{N_{Fiducial}}.$$

Here, N.D. stands for the neutral density of the filters used. At this point we still cannot determine the actual fluctuation level as this requires a knowledge of the scattered power (or power times δt). The conversion from intensity to power requires a complete knowledge of all the areas involved. Three come to mind: (a) the area of the ruby laser radiation at the scattering volume; (b) the actual area from which scattered light is emitted; and (c) the area in the observation plane which corresponds to a pixel in the streak camera. In addition, in scattering theories it is usual to calculate the differential scattering (power per angular range). The resulting scattered power is

$$\frac{dP_s/d\theta}{P_{inc}} = \frac{I(\theta)}{I_{edge}}\left[\frac{s'\delta\theta\Delta y f}{\Delta x\Delta y}\right]\left[\frac{\Delta x\Delta y}{\sigma}\right]\left[\frac{1}{\delta\theta}\right].$$

The first term in square brackets on the right is the ratio of the detected area imaged onto the streak camera to the area the ruby laser illuminates at the jet. Here f represents the fraction of the area in the y direction imaged and is equal to 1.0 if the entire area is imaged. The second term corrects for the fact that the area of the Thomson scattering σ is not necessarily the same as the total area of the ruby laser radiation. The final term converts the entire expression to a differential scattering expression.

The scattering cross-section has been computed in terms of the fluctuation level by Slusher and Surko [40] for a single epw

$$(\delta n/n_o)^2 = 2dP_s/d\theta/n_e^2 r_e^2 L^2 \lambda^2 P_{inc}$$

where L= length of the scattering volume crossed, r_e is the classical electron radius and λ is the wavelength of the incident probe. A factor of $1/2$ has been introduced since the theoretical power (above) includes contributions from all frequencies. The experiment looks at power radiated in $1/2$ of the frequency range (only the anti-Stokes component).

Substituting for the scattering cross-section and simplifying, one finds

$$(\frac{\delta n}{n_o})^2 = \left[\frac{2 \quad 10^{-N.D.} N_2 \Delta y f}{\pi^2 r_e^2 \lambda \tan^2 \theta_o N_1}\right]\left[\frac{N_{signal}}{n_e^2 L^2 \sigma N_{fiducial}}\right] \qquad 3-3$$

where the term inside the first bracket is a constant for a given optical setup while the terms inside the second bracket can vary from shot-to-shot.

The wide angle k resolved system had the same incident optics as the narrow angle system. The scattered light was collimated by a mirror and directed out through a large window. (This was necessary since the window used in the first experiment was too small to permit a large angular range to be examined.) A narrow strip of area in the Fourier transform plane was demagnified and imaged onto the slit through interference filters and a cylindrical lens. The scattered light had to be sent over the gas jet and a mask was located such that no plasma light could reach the slit directly. (Without the mask, the scattered signal was lost in the plasma light.) Reasonable care was taken to ensure that the mask did not cut off part of the scattered light.

Common to both k resolved systems was the method of determining the scattering angles. The absolute angle (or position of known θ) was determined using a HeNe laser which passed through the CO_2 focal volume. Its angle was found by

noting the perpendicular distance, d_1, between the light from this HeNe laser and the HeNe laser used to align the ruby laser at a measured distance, d_2, from the jet. The angle was then arctan (d_1 /d_2). This angle was measured to ± 0.2 °. The streak camera channel corresponding to this angle was recorded. The uncertainty in this angle was due primarily to an uncertainty in d_1. Since d_1 was 20 ± 2mm and d_2 was 300 ± 2 mm, this means $\theta_o = 2.6 \pm .2°$.

The angular dispersion (degree / channel) was measured using a mask of equal dark and light regions of width w placed at the known distance d_2. The mask was examined by the streak camera in focus mode (the continuous or nonstreak mode of the camera) either in transmission (first setup) or reflection (second setup). The dispersion was calculated by noting the channels corresponding to the light-dark transistion and dividing the difference in channels into the angle arctan(w / d_2). For the narrow angle Thomson scattering system, the average dispersion was 0.00022 radians per pixel.

To interpret the resulting k-resolved records, some assumptions about the frequency of the scattered light had to be made. Of course, the use of interference filters had restricted the range of ω selectable, but the filters still had a finite bandpass. In the first k-resolved scattering, it was assumed that the waves which scattered the light were those generated by SRS (and thus have known frequencies.) Since two scattering conditions had to be satisfied, those of SRS and those of Thomson scattering, it was possible to assign to a given angle a unique density and a unique wavevector. This simultaneous wavevector matching is shown in figure 3-10.

The k-resolved streak camera records were interpreted as follows. An incident EM wavevector, $\vec{k}_o$, of length $\omega_o(1 - \omega_p^2/\omega_o^2)^{1/2}/c$ decays into a scattered EM wavevector, $\vec{k}_s$, of length $\omega_o(1 - 2\omega_p/\omega_o)^{1/2}/c$ and an EPW wavevector, $\vec{k}_{epw}$, whose length depends upon the angle Ψ at which the $\vec{k}_s$ is directed. The usual k and

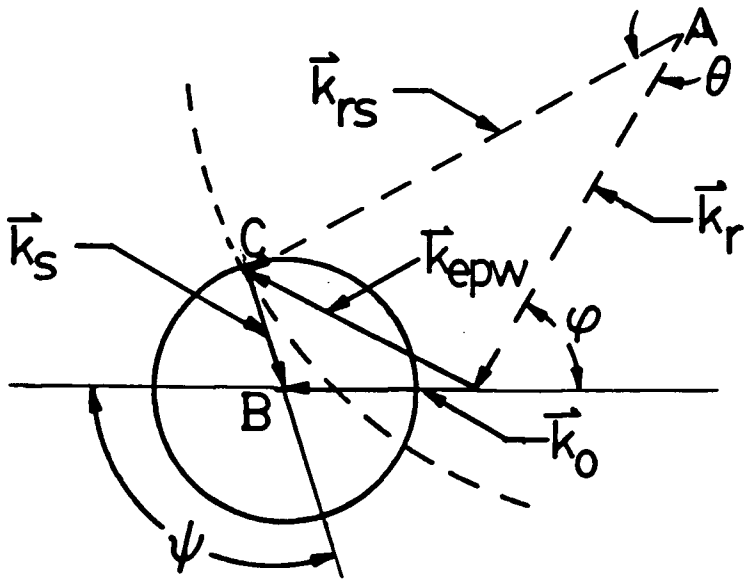

Figure 3-10 Simultaneous wavevector matching for SRS and Thomson scattering.

ω matching conditions apply to this SRS process. In Thomson scattering the incident probe light with wavevector, $\vec{k}_r$, of length ω_r/c, scatters off the EPW and exits the plasma with a wavevector $\vec{k}_{rs}$ of length $(\omega_r + \omega_{epw})/c$. For a fixed angle of incidence φ, θ is fixed for a given density since the point C is fixed (see Fig.3-10). C is the intersection of a circle centered at A with radius k_{rs} representing all the possible $\vec{k}_{rs}$ directions (the dashed arc) and a second circle centered at B with radius k_s respresenting the possible k_{epw} directions (the solid circle). The solution for various densities at our given angle of incidence ($\varphi = 56°$) shows that we can observe SRS driven epw corresponding to EM scattering at $\psi = 180°$ $(0.25n_{cr})$, at $\psi = 143°$ $(0.2n_{cr})$, and at $\psi = 135°$ $(0.15n_{cr})$. (Only the solution which gives plasma wavevectors longer than k_o was considered.)

Since a unique frequency can be assigned to a given angle, it is possible to correct for the bandpass edge rolloff of the interference filter. The transmission of the filter was measured using a monochromator attached to an optical multichannel analyzer (OMA). A broadband, incandescent source (a flashlight) was used to illuminate the filter and the spectrum of the transmitted light was recorded. At a given θ an ω_{rs} is deduced . The signal at that angle is divided by the transmission

of the filter at the scattered frequency. This method is crude, but assures that the k spectra are correctly interpreted.

In the second k experiment, it was assumed that all the waves probed were generated at $0.25n_{cr}$. This is not true in light of the above analysis, but for $\theta \geq 4.5°$, scattered light from SRS EPW would be shifted in frequency and would not be able to penetrate the interference filters. If scattered light is observed at these angles, it cannot be generated by SRS. It can also not be generated by SBS, as the scattered light frequency from that process is nearly the same as the probe and cannot penetrate the filters. (SBS light would have a maximum near 7° if there were no filters present.)

The assumptions made about ω_{rs} are verifiable if the scattered light is collected and sent through a spectrograph. This was done in the ω-resolved Thomson scattering. The plasma was imaged (demagnified) onto the entrance aperture of a spectrograph through a single interference filter. This filter was the 694.3nm filter tilted to 22°and thus permitted a wide wavelength range near 672nm to enter the spectrograph while still rejecting the unshifted ruby light by a factor of more than 100. The scattered light was collected over the same angular range that the narrow angle k resolved Thomson scattering examined. No entrance slit was used, since the image itself was small enough. The exit plane of the spectrograph was imaged onto the streak camera slit. The spectrograph permitted a range of 30 nm to be examined at a time. The relative dispersion was determined using several Ar I lines (696.5, 687.1, 675.2 nm) in the wavelength range of interest. Light from an argon Geisler tube was focussed over the gas jet through the same optics that were used for the Thomson scattering. These 3 lines were displayed across the slit of the streak camera and the positions of the lines were recorded by integrating the streak camera output using the internal trigger capabilities of the camera. From the recorded channel position of each of the lines the dispersion was calculated to be 0.172nm / channel. The streak camera was used in focus mode while these lines

illuminated it. The channels corresponding to line center were used. The absolute wavelength was found by assuming the SBS line to be unshifted ruby laser light at 694.3 nm. The relative dispersion and the channel separation from the SBS line was used to find λ at any channel. The experimental setup is shown in figure 3-11.

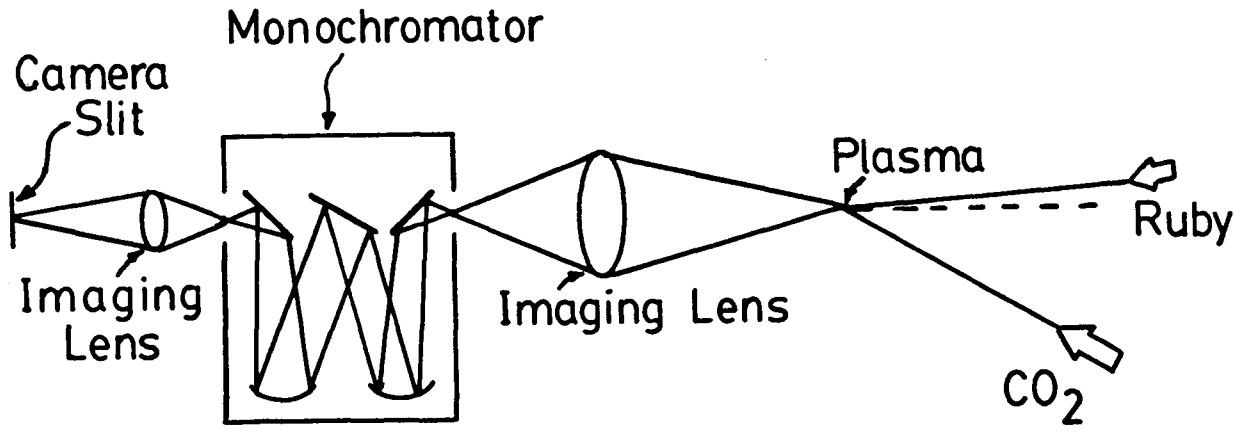

Figure 3-11 Frequency resolved Thomson scattering. A ruby laser interference filtered tilted to 22°is located in front of the entrance of the monochromator to reduce stray ruby laser light. An OMA could not be used to record a time integrated scattered light spectrum since there are, as noted earlier, several optical spectral lines present including one N I line which occurs exactly where Thomson scattered light from quarter critical density should occur, at 672.3 nm. In time resolved measurements, these lines will appear much later (i.e.when the plasma has cooled) than the Thomson scattered light.

The wavelength resolution of the system was measured by sending the well attenuated ruby laser light pulse through a pinhole at the jet into the monochromator and streaking the resulting single line. Since the line width of any ruby laser is less than 0.1 nm, any width observed is due to instrument broadening. The FWHM observed corresponded to 1.38 nm.

A few comments about the streak camera used are now made since it is being used to its limits. The linear dynamic range S_{max}/S_{noise} was measured by Bernard

who measured a dynamic range of 100. However, the upper count number is dependent upon how many persistence integrations were performed. For a greater number, the upper limit increases. Since the noise level also increases, the dynamic range should not change. The temporal resolution must also be emphasized. The manufacturer's measured temporal resolution is 2 picoseconds. This limit is set by several factors, one of which is the size of the entrance slit as it imaged onto the photocathode of the streak camera. For optimum temporal resolution, this image must be made as small as possible. This can be ensured if the entrance optics of the streak camera are fully illuminated. In each k case, the cylindrical lens was placed such that the entrance optics of the streak camera were fully illuminated. The temporal resolution is limited by two other factors. The actual streak rate used is important: the pixel resolution is the sweep time divided into 256 channels. For the growth rates measured, this digitizing resolution is 2.2 ps. The other factor is the intensity factor: the brighter the streaked light, the wider the recorded image is. Although this effect is difficult to quantify, it should be noted that no real difference in growth rates was found between (a) those measured for intensities similar to the ones at which the manufacturer measured the temporal resolution and (b) those at higher intensities which were within the dynamic range of the camera. Well saturated shots were not analyzed. The relative sensitivity across the streak tube was also measured. The center of the streak tube is about a third more sensitive than the edges. This was measured by uniformly illuminating the slit by attenuated ruby light and streaking the result. A quadratic response across the tube was observed and used to correct the k spectra.

3.3 Infrared Diagnostics

The second aspect of SRS which was investigated was the scattered EM radiation. Spectrally integrated and spectrally resolved measurements were performed.

Common to both measurements are the problems of absorption and dispersion in KCl and rejection of SBS. The first problem manifests itself in that at 15μm, KCl starts to absorb IR with transmission per cm dropping from 90% (Fresnel losses only) to 30% at 21μm. By the Kramer-Kronig relations, strong absorption is associated with strong dispersion. In KCl , n=1.454 at 10.6μm while n=1.39 at 21.2μm. When imaging the plasma at various IR wavelengths, the resulting chromatic aberration must be considered. In our case, a single KCl lens was used and its focal length was kept as short as possible. The lens subtended 0.016sr solid angle.

The second problem concerns SBS rejection. This was important since SBS is very strong and could be expected in second order in the monochromator. Since SRS can generate a signal at 21.2 μm, we had to be sure that no second order SBS light was detectable. Two 14μm redpass (cut-on) filters (OCL#L-13514-9) were used to provide a rejection of SBS of greater than 2.5 x 10^7. No SBS signal was seen through the two filters. This was checked by setting the monochromator to 10.6μm; no signal was observed at this wavelength. (A weak signal was seen through a single filter.)

The detector used in all SRS measurements was a Ge:Cu detector manufactured by the Santa Barbara Research Corp. It had a 5 mm diameter detector area behind a KRS-5 flat. (KRS-5 is a standard optical material for use in the far infrared. It is made from pressed, polycrystalline thallium bromo-iodide.) To detect light at 21 microns, the detector must be liquid He cooled. The spectral response, according to the manufacturer's specifications, should be constant to within a factor of 2 over the range 15 – 21μm.

Two types of spectrally integrated measurements were carried out. The integrated signals were observed to get some idea of the energy scaling of the signal and more importantly, to see how large a signal could be expected. The optics were set up as in figure 3-12(a). A crude resolution of the spectrum was performed using a

single redpass filter and a 15 micron bandpass filter (FWHM = 2 microns). This filter was an OCL#W-15000-9A filter.

The signal levels were sufficient that it was thought possible to resolve spectrally the signal on a finer scale. A second IR arrangement was setup as in figure 3-12(b). In this arrangement, since a smaller signal was expected, chromatic aberrations were considered more carefully. For this reason, a shorter focal length lens was used. The shorter focal length also allowed the plasma image to be reduced in size. This second consideration was important for lineup considerations. Although the plasma image itself was small (200μm), its actual position varied day-to-day by up to 2 mm. It is this change which had to be reduced so that the scattering volume was assured to be imaged into the entrance of the monochromator. The entrance aperture was positioned so that 20 micron light was perfectly imaged into it. The exit slit was imaged 1:1 onto the detector through the 2 redpass filters. The wavelength resolution, based upon the slit width imaged onto the detector was 0.2μm FW.

The effects due the varying f# mismatch with wavelength were calculated by multiplying the solid angle subtended by the collection lens with the ratio of the area of the collimating mirror of the monochromator to the area over which the collected light would be spread at this mirror's position. The resulting effective solid angle is plotted in figure 3-12(c). Complications in the lineup also involved the HeNe laser light used to align the IR optics since it was affected to a greater degree by the chromatic aberration. The HeNe beam was used primarily on the optical axis of the system so that image position problems occurred only along the axis. There were no beam angle deflections. This ensured that the optical system would be centered for any wavelength; only the image positions along the optical axis would be uncertain. The system of alignment had one drawback. In order to minimize lineup errors, an f# mismatch had to occur for the signals into the monochromator. A better system would use two KRS-5 lenses which have much better dispersion

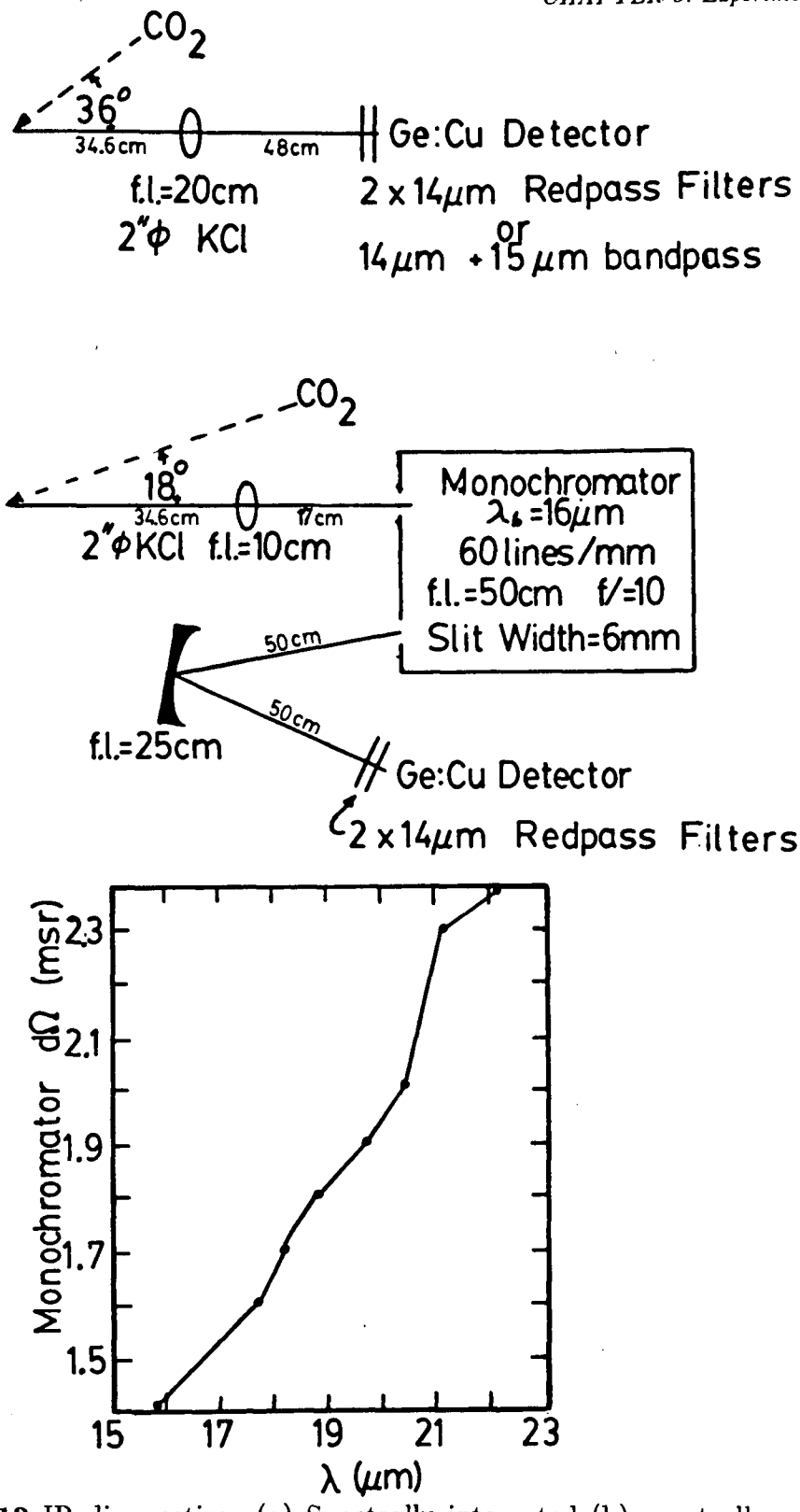

Figure 3-12 IR diagnostics. (a) Spectrally integrated (b) spectrally resolved (c) Effective solid angle detected

and transmission properties. The first lens would be used to collimate the scattered IR while the second could match the f# of the monochromator properly. Cost and time delays were the reasons this approach was not used. Complete use of only reflection optics would eliminate any chromatic aberration problems. However, severe spherical aberrations would have been introduced if mirrors were used to collect and direct scattered light from the target chamber since these mirrors would have to be used offaxis in order to avoid the jet nozzle on the way out. However, once the light has entered the monochromator, chromatic aberration is no longer a problem since only mirrors are used thereafter.

3.4 Electron Diagnostics

The third aspect of SRS which was investigated was fast electron generation. For this, the spectrometer outlined in figure 3-13 was used. An electromagnet disperses and line focuses the electrons. These are detected by a NE102 plastic scintillator disk (behind 5 μm thick Al foil) connected to an OMA with optical fibers. The magnet current was kept fixed so that electrons at 50, 100 and 150 keV could be observed. (No signal was seen in the lowest energy channel which is indicated in figure 3-13 as low energy electrons cannot penetrate the Al foil.)

Once the electron energy spectra are taken, there comes the question of interpretation. To fit a temperature (k_BT), a Maxwellian distribution of velocities must be assumed although there is some question as to whether this is completely justified. Further, it is not clear whether a 1-D or 3-D distribution should be tried. In the following, I will attempt to explain the choice I made. Since the electron spectrometer is located far from the plasma, the electron distribution found is biased. An effusion process is the appropriate model to apply. (For a simple model of an effusion process, imagine a pressurized sphere with a small hole which allows the gas to escape.) This implies

$$f(v_x, v_y, v_z) \propto v_z f(v_z) f(v_x) f(v_y)$$

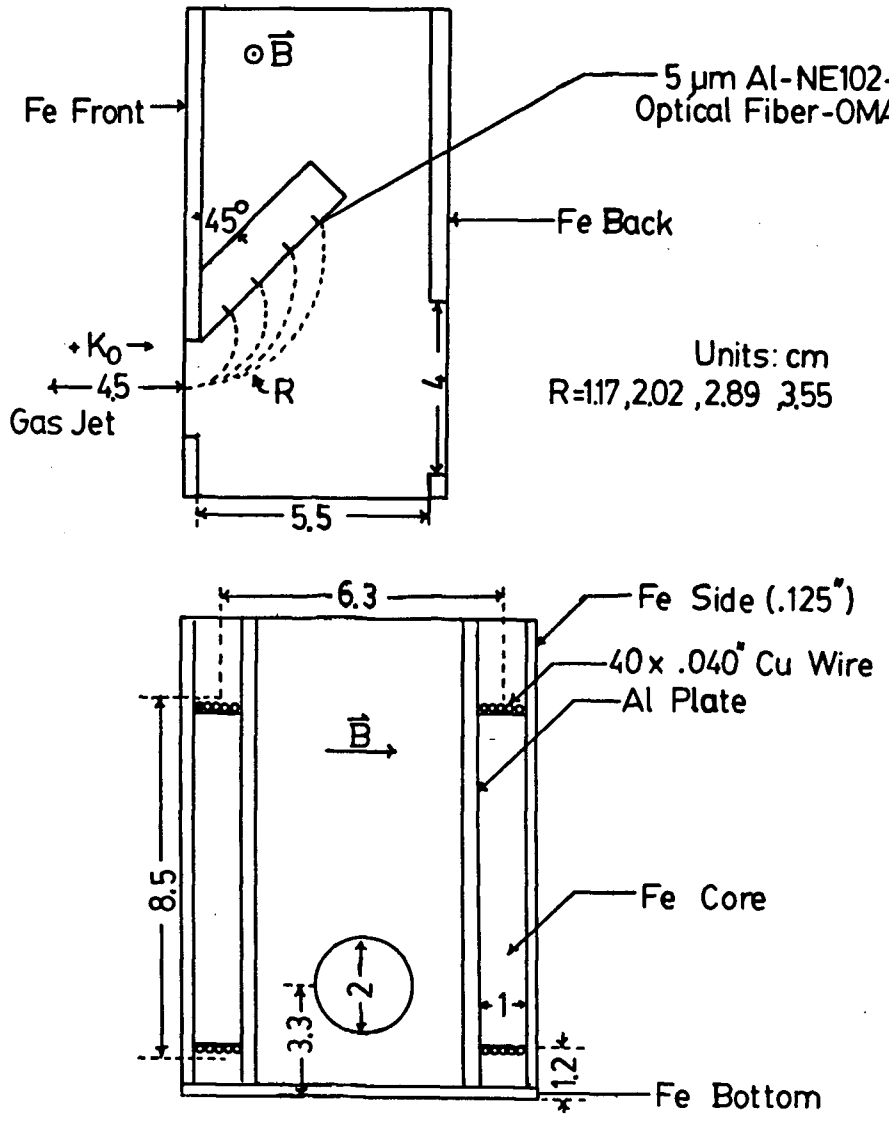

Figure 3-13 Mk.III electron spectrometer. All dimensions are in cm unless otherwise indicated.

for the spectrometer centered on the z axis.

The spectrometer is assumed to have an entrance aperture of radius r and is located a distance z_o from the plasma. If $r \ll z_o$, then v_x, v_y will both be $\ll v_z$. In fact,

$$v_x/v_z = v_y/v_z = r/z_o.$$

The observed signal is proportional to the total energy deposited on the scintillator

$$S \propto \int\int\int 0.5 m_e (v_x^2 + v_y^2 + v_z^2) f(v_x, v_y, v_z) dv_x dv_y dv_z.$$

The integration is performed over the scintillator area.

The spectrometer was designed to focus the electrons where focussing means that all electrons which leave a point at the plasma (the object) with a given speed converge at a line on the scintillator (the image). (Of course, only those electrons which pass through the entrance aperture of the spectrometer are focussed.) Electrons from the same object point but having different speeds will be focussed to different image lines. (Since the spectrometer uses a dipole magnetic field, there will only be focussing in the plane perpendicular to the B field.)

This situation is analogous to chromatic aberration in ordinary optics. Light which leaves a object point passing through the entrance pupil of the system is focussed to an imaged point. Light of different frequencies (the analogy of different speeds) will be focussed to different points. The analogy continues if one considers the spectrometer as a cylindrical lens.

The above argument justifies the following. Since $v_x^2 + v_y^2 + v_z^2 = v^2 \approx v_z^2$, we can approximate S as

$$S \propto 0.5 m_e v^3 \exp(-0.5 m_e v^2 / \mathrm{k_B T}) d^3 v$$

where a Maxwellian velocity distribution has been assumed. The term d^3v can be evaluated (approximately) as

$$(vd\phi)(dv)(v\Delta r/z_o)$$

where $d\phi = r/z_o$ and $dv = eB\Delta r/m_e c$. B is the magnetic field of the spectrometer and Δr is the radius of the scintillator. (This choice of this d^3v presumes a 3-D distribution of velocities, at least over a limited solid angle.) If we let $E = 0.5m_e v^2$, we find

$$S/E \propto E^{3/2} \exp(-E/\mathrm{k_B T}) \qquad 3-4$$

which is the function which was used to find $\mathrm{k}_B\mathrm{T}$.

Corrections for channel-to-channel variations in sensitivity have been made. The linearity of the electron signals detected was checked; the largest signal was 80% of the maximum linear range. A non-linear least squares routine (UBC Computing Centre NL2SNO) was used to fit the function above to the observed energy spectra to find $\mathrm{k}_B\mathrm{T}$.

CHAPTER 4

Results

In this chapter, the main results of my research are presented with a few, very brief comments made on them. A detailed discussion of their implications is given in the next chapter.

4.1 General Observations

Theory suggests that once a certain laser intensity is reached, SRS should occur. In experimental terms, this means a certain energy in a typical pulse time must be provided. Therefore, it is interesting to plot various signals versus incident energy. In figures 4-1 and 4-2, the relative $14 - 22\mu$m integrated IR scattered light energy and the relative number of electrons at 150 keV are shown as a function of pulse energy. The amount of each can be seen to grow nonlinearly. The vertical error bars are the standard errors of more than 4 data points while the horizontal errors represent the size of the energy bins used for averaging. A threshold energy upper limit of about 3 Joules, corresponding to an intensity of 1.9×10^{13} Wcm^{-2}, can be inferred from the electron numbers. This agrees with the upper limit on the threshold deducible from the integrated reflectivity measurements where the limit is set at the intensity where the signal to noise ratio equals one. For calculation purposes in the next chapter, an intensity slightly above this threshold of 3×10^{13}

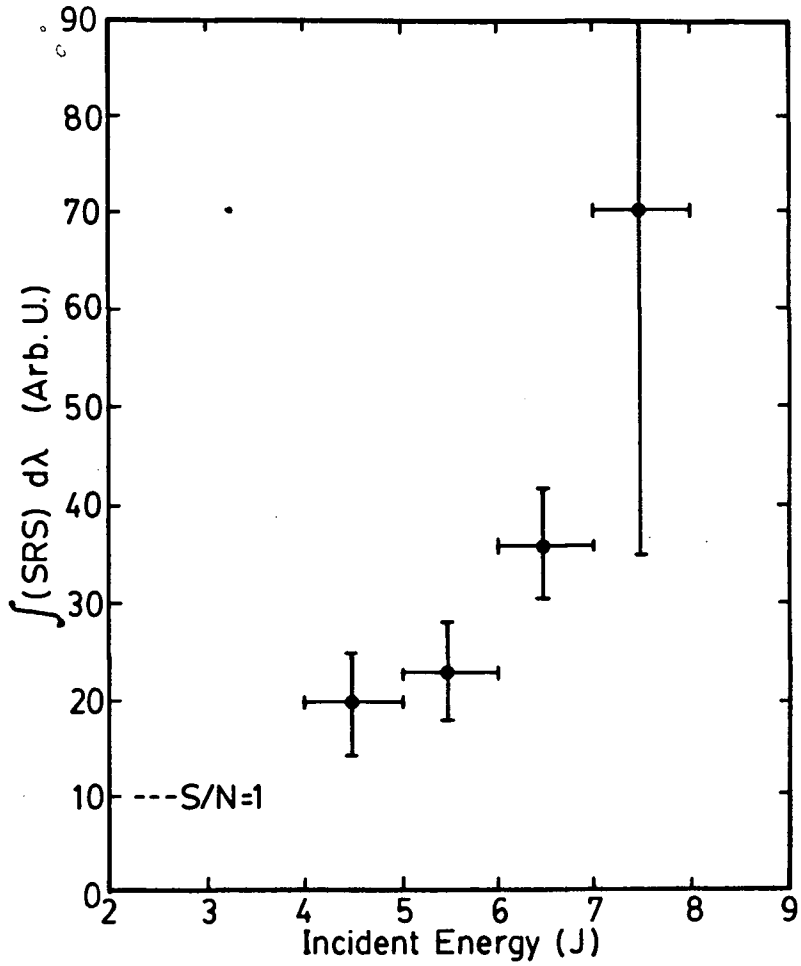

Figure 4-1 Threshold behaviour in the scattered IR light. The light was integrated from 14 to 22μm. No signal was found at low energy.

Wcm^{-2} will be used. This corresponds to average intensity on target corresponding to 5J. Most of the results were obtained at this energy.

4.2 Results from Spatially Resolved Thomson Scattering

In a finite or an inhomogeneous plasma, there is a characteristic length L which is important in determining thresholds. It is also important in determining the nature of the instability i.e. whether it is an absolute or convective instability. This L can be the length of the plasma, the density scale length, or more generally, the length of the interaction region.

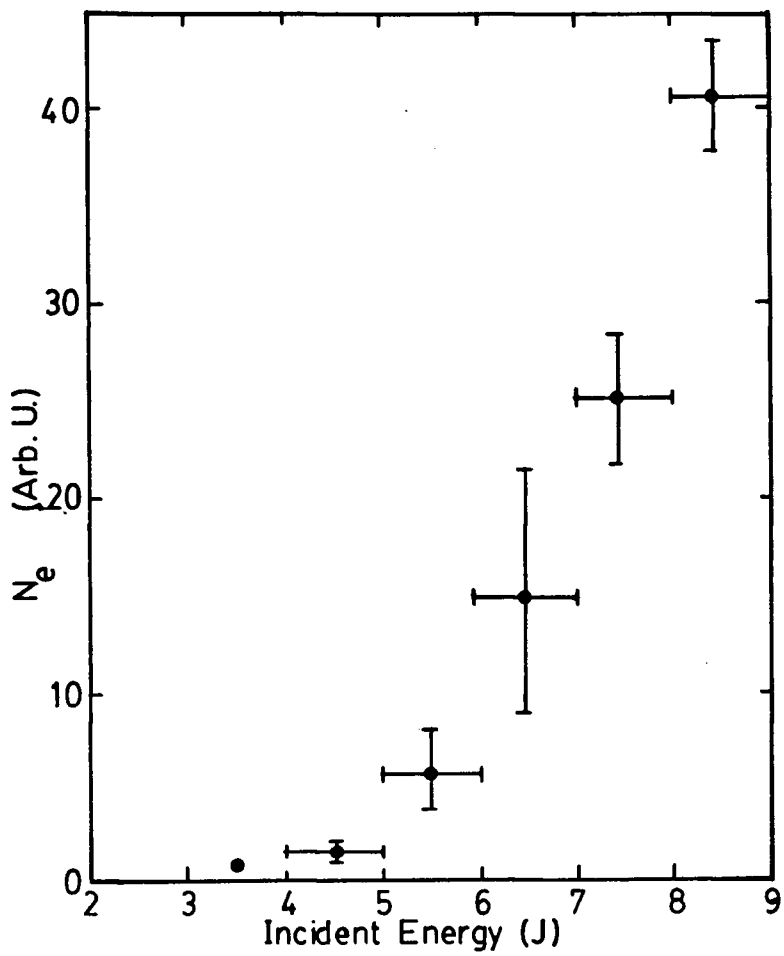

Figure 4-2 Threshold behaviour in the number of fast electrons. No electrons were observed at low energy.

In the present experiment, the plasma size and density (and thus L) were checked independently using interferometry and spatially resolved Thomson scattering. Since an extensive series of interferograms was available[60], it was useful to correlate where SRS occurred with the plasma density regions found from interferometry. This can be done by comparing the spatially resolved Thomson scattering results with the observations of the plasma light taken through the same optics. In figure 4-3(a), a density contour plot of the plasma for conditions at which SRS occurs is shown. The view is from 90°to the CO_2 laser axis and the contours are cylindrically symmetric around the axis. The quarter critical density contour is

emphasized while the contour interval is $0.05n_{cr}$ Early in the laser pulse, the interferometry shows that the plasma is about 200 microns long. In figure 4-3(b) the position of plasma light and the region where the Thomson scattering occurred are illustrated in streak camera photographs. The Thomson scattering comes from the very beginning of the plasma in time. (The bright line across the plasma light is a streak camera digitizing error.) Although the two distinct plasma regions of figure 4-3(a) are not seen in the plasma light of figure 4-3(b) because the the plasma is viewed from 60°to the laser axis instead of 90°, one can still identify the plasma region where the SRS occurs since the SRS occurs in the plasma region which forms first. The front plasma region of figure 4-3(a) formed first. This is clear since this front region has a well developed annular shape (the result of a shock wave) whereas in the rear plasma region, the plasma still has the characteristic initial spherical shape.

In figure 4-4, a contour plot of the spatially resolved Thomson scattering is given. The intensity contours are in steps of 1/4 of the maximum level. The size is 200 microns, although from shot to shot this varied from 190 to 410 microns (see the further examples of figure 4-5). The diffraction limited resolution of the spatially resolved Thomson scattering optical experiment was limited by the aperture used to define the wavevector range of the scattered probe light that was permitted to enter the optical setup. The resolution calculated was 36μm which agrees with the observation that features 50 microns in size can be seen. A streak camera pixel corresponds to 16 microns. The axial distance has been calculated assuming no radial width to the scattering region (see section 3-2 for details). If the width is set to $2r_o$, the axial distance is reduced to 140 μm. The scattering appears to be coming from only one region in space; there are no multiple regions of scattering as was observed in the case of SBS[47]. A lower limit on the average density scale length is established by assuming one end of the scattering region is at n_H density while the other end is set to n_L density. Since 0.15–0.25 critical density is the

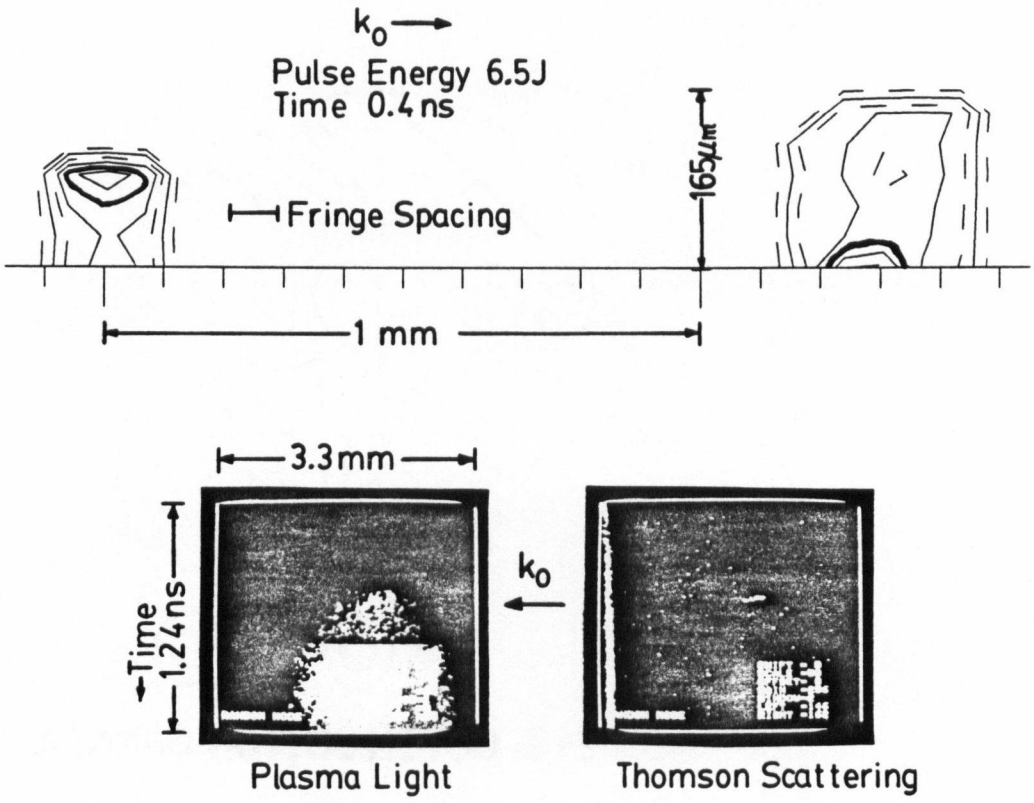

Figure 4-3 Position of the scattering region relative to the plasma. (a) Density contour plot (b) Plasma light and scattering region as observed through the same optics. Note that the Thomson scattering occurs at same temporal and spatial position as the beginning of the plasma light.

maximum density region expected for the given mask and interference filter used in the Thomson scattering, n_H can be set to $0.25n_{cr}$ and n_L to $0.15n_{cr}$. From the formula

$$L = n\frac{dx}{dn} \simeq \frac{n_H + n_L}{2}\frac{\Delta x}{n_H - n_L}$$

a scale length of 400μm at $0.2\ n_{cr}$ can be deduced. This is a lower limit since $n_H - n_L$ may be smaller than assumed. Scattering from densities outside the experimentally permitted limited range will make no contribution to observed scattering. This

scale length is of the same order as the scale length determined by interferometry. For calculation purposes in the next chapter, a typical characteristic size of 300μm will been used.

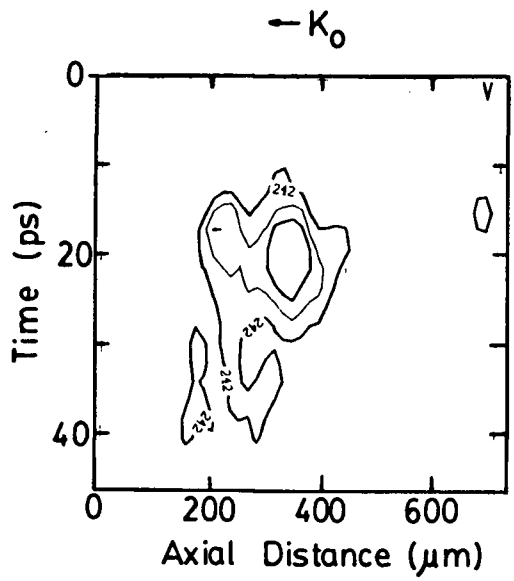

Figure 4-4 Spatial extent of SRS scattering. The intensity contours are in steps of 1/4 of the maximum level.

4.3 Results from the Wavevector Thomson Scattering

By imaging an area of the vertical focal plane onto the streak camera slit instead of the plasma (which is positioned at the horizontal focal plane of the astigmatic lens – see figure 3-7), the wavevectors generated in the plasma could be probed. In particular, EPW with wavevectors of length $k/k_o \approx 1$ and frequencies

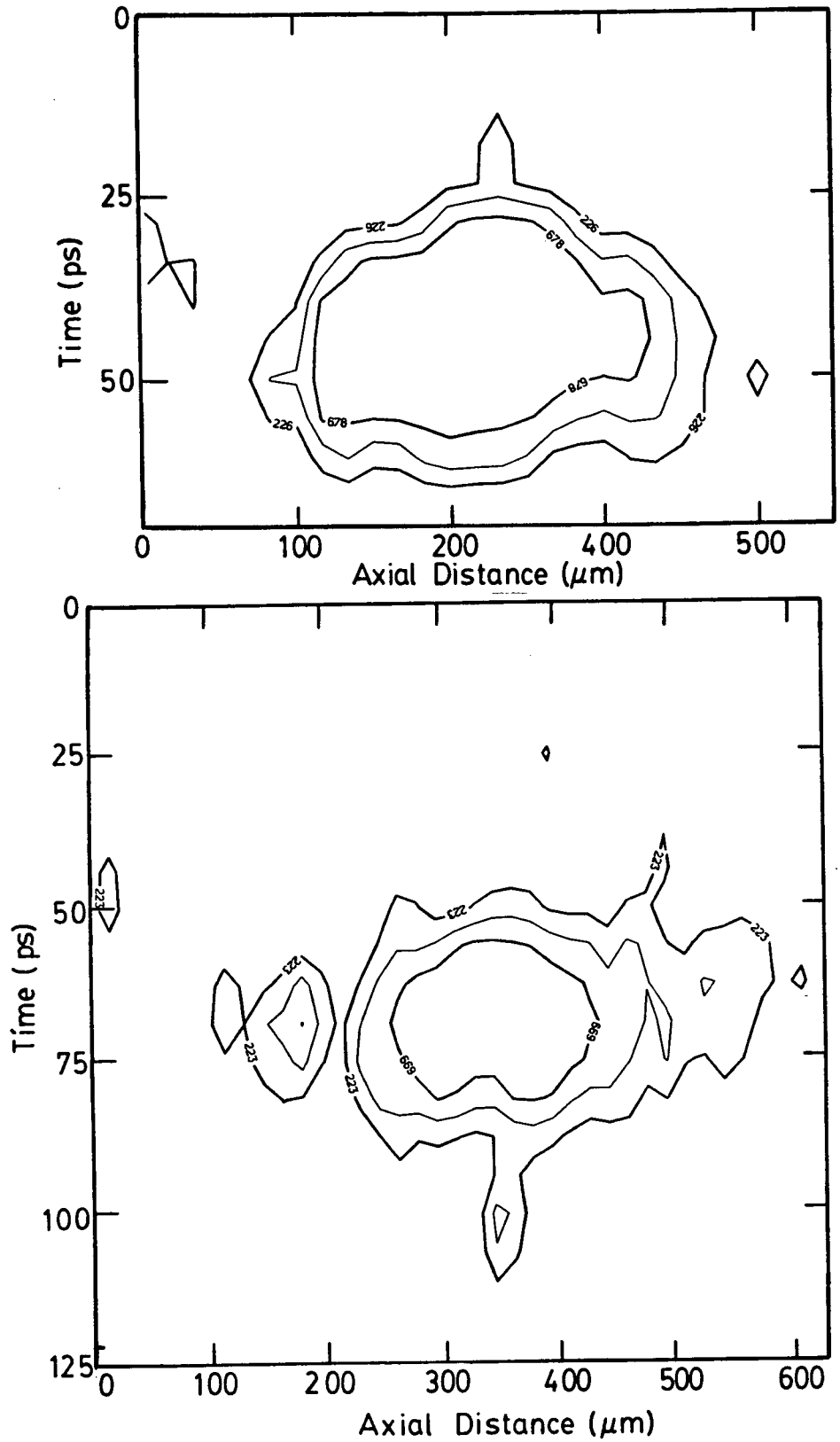

Figure 4-5 More examples of spatially resolved streaks of SRS.

$\omega/\omega_o \approx 0.5$ were of particular interest as these are the waves which SRS is supposed to enhance to levels well above the noise. In figure 4-6, a typical streak record shows two bursts of SRS, each about 15ps long and separated by 15ps. The relative k width of each burst can vary from shot-to-shot (see the further examples of figure 4-7). The dashed line in figure 4-6 is explained in the next chapter. Figure 4-8 shows the fluctuation level, averaged over the observation window, plotted as a function of time. This is an exceptional case in which there is weak reappearance of SRS after 200ps.

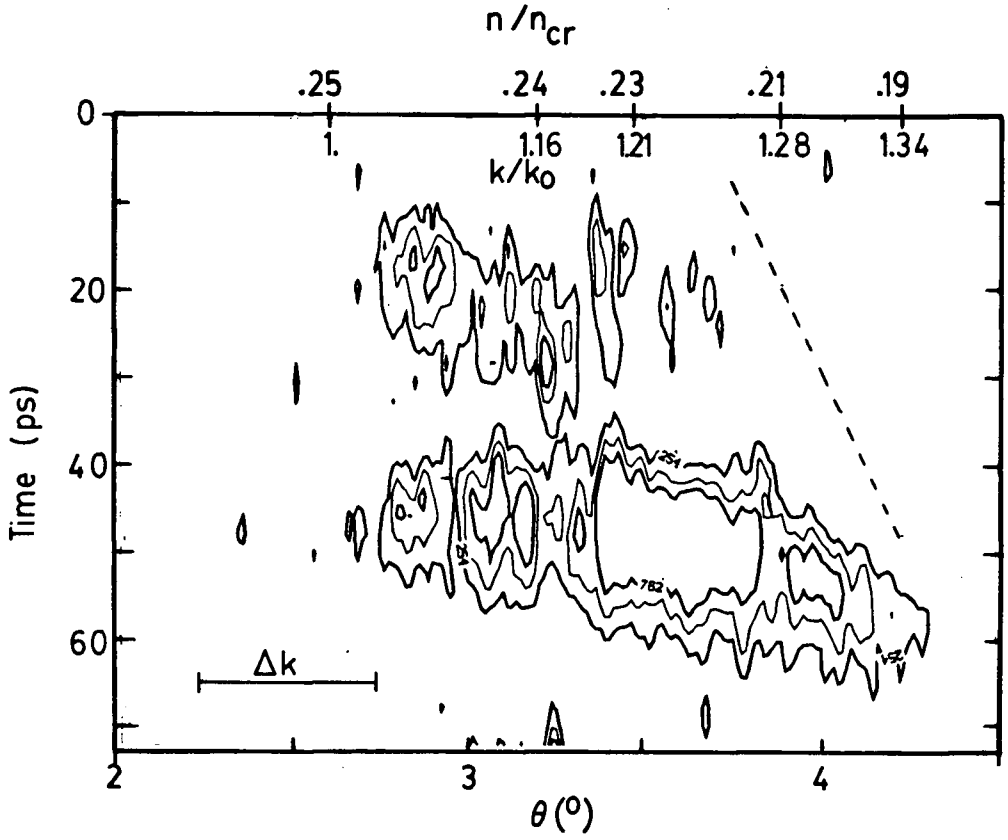

Figure 4-6 Example of a wavevector resolved streak record.

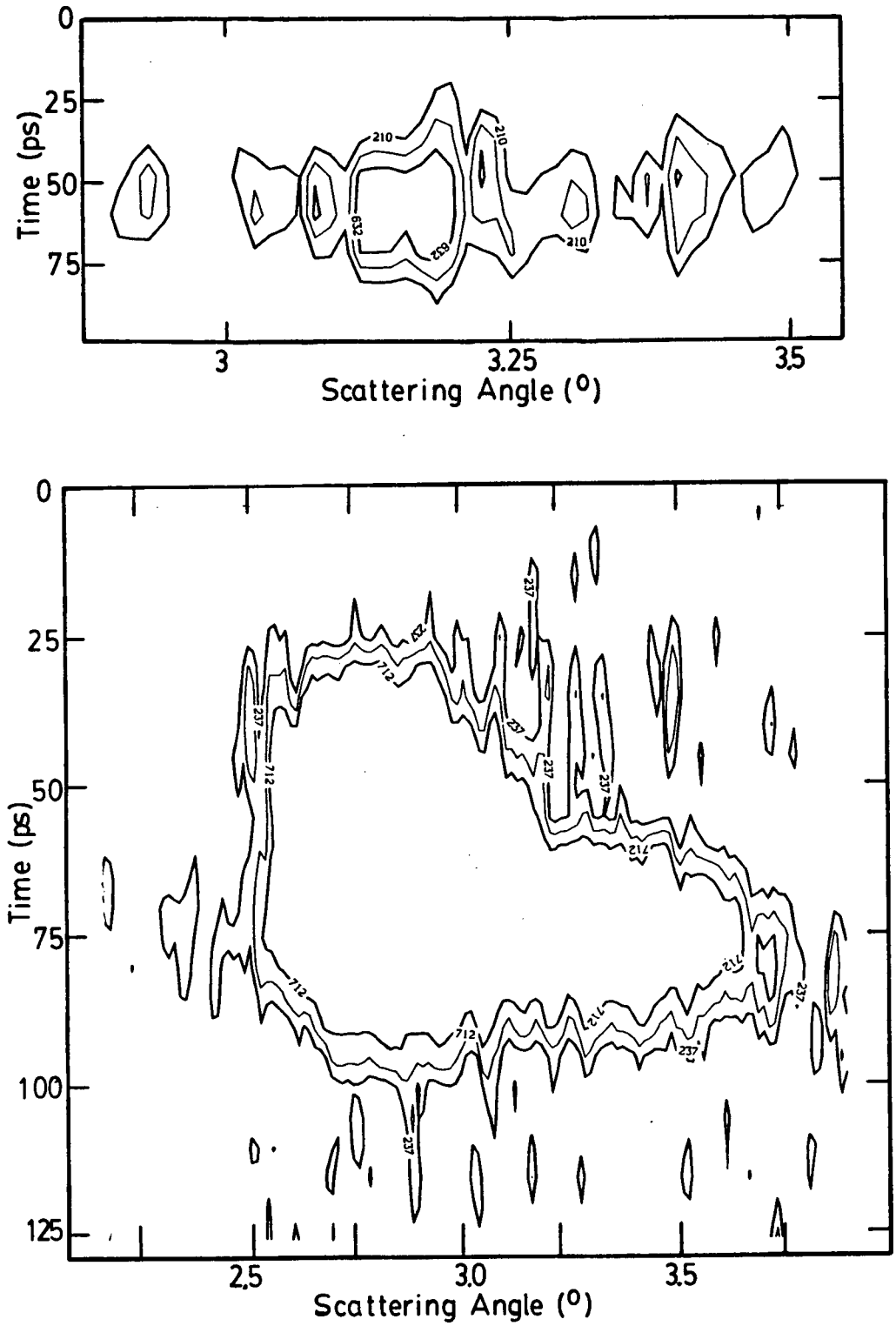

Figure 4-7 Further examples of wavevector spectra of SRS. The conversion from angle to density is the same in figure 4-5. The second streak is saturated.

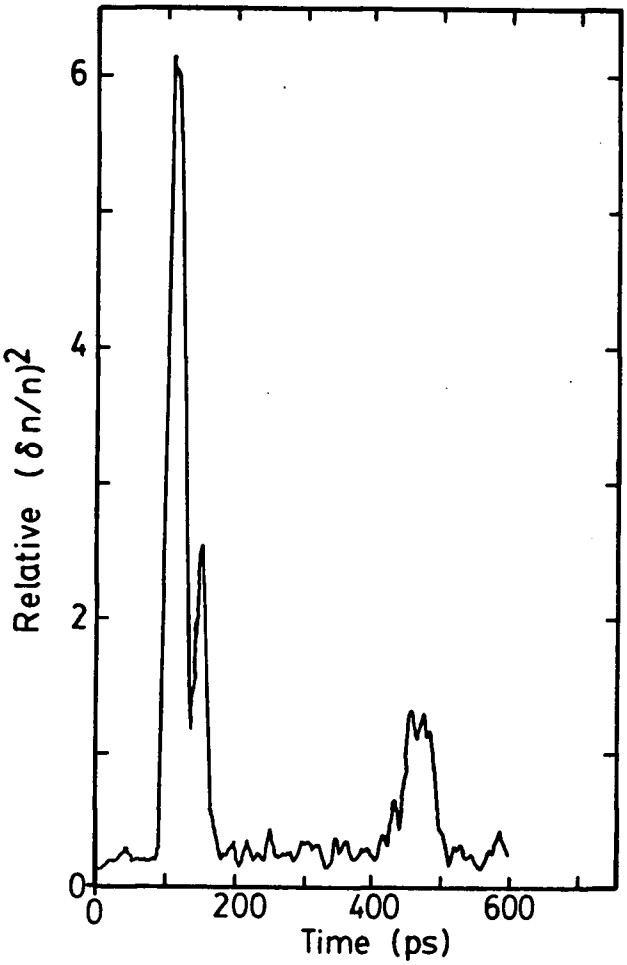

Figure 4-8 Reappearance of SRS in an exceptional case.

The k-resolved spectra, by inference (see section 3.5 for details), show that SRS occurs at all densities 0.15-0.25 n_{cr}. This observed range is limited by the interference filters used. In figure 4-10, we see some evidence of scattering at angles less than 2.6°which means that the EPW wavevectors are shorter than k_o. SRS can generate such wavevectors but only if the scattered IR light is scattered forward. Forward scattering was usually not present. In figure 4-9, a raw k spectrum averaged over 10 shots is presented (dashed curve). The maximum fluctuation level seems to be, *on average*, independent of density. The effects of the finite bandpass of the interference filter (the dotted line) which was discussed in chapter 3 and the streak camera non-uniformity of response have been deconvoluted to yield the solid

curve. It is quite suggestive of the frequency shift in the ruby scattered light that the expected rolloff due to the interference filter actually can be seen to occur in the dotted curve.

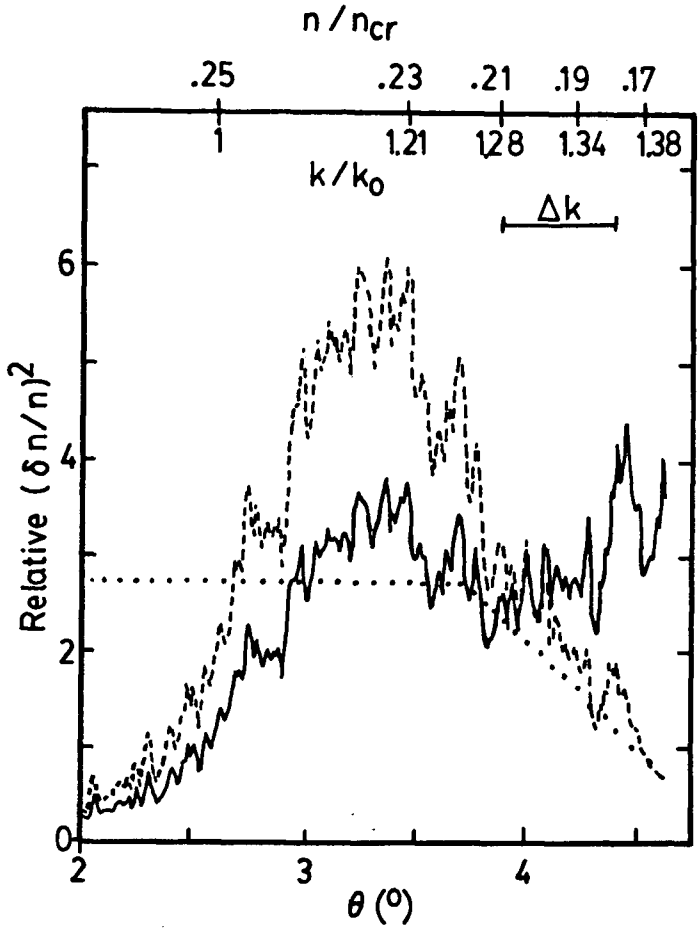

Figure 4-9 Average k vector resolved spectrum of SRS. The dashed curve represents the uncorrected spectrum, the dotted curve represents the interference filter bandpass and the solid curve represents the average fluctuation spectrum corrected for the bandpass rolloff.

Wide angle Thomson scattering was set up to scatter from the electron plasma waves generated by SRS, as well as those waves generated by the TPD instability. Since the EPW generated by TPD are most intense in the plane of polarization of the incident laser, the Thomson scattering in this setup was performed in this plane. Figure 4-10 shows several examples of the streak records obtained in this

experiment. It is interesting to note that the angular width varies considerably from shot-to-shot for nominally unchanged experimental conditions and that the angle at which the scattering originates also varies. On average, the scattering ranges from 3.4 ± 1.1° to 6.5 ± 1.3°. These angles correspond to k/k_o from 1.2 ± 0.3 to 2.1 ± 0.4 . Scattering at angles less than 4.5° is due to SRS-generated EPW whereas scattering at larger angles must be due to TPD. This average range (from 3.4°to 6.5°) is independent of incident laser energy. The maximum angle at which scattering was observed was about 9°, which corresponds to $k/k_o = 2.9$. In figure 4-11, it can be seen quite clearly that there is a progression in time from shorter to longer wavevectors.

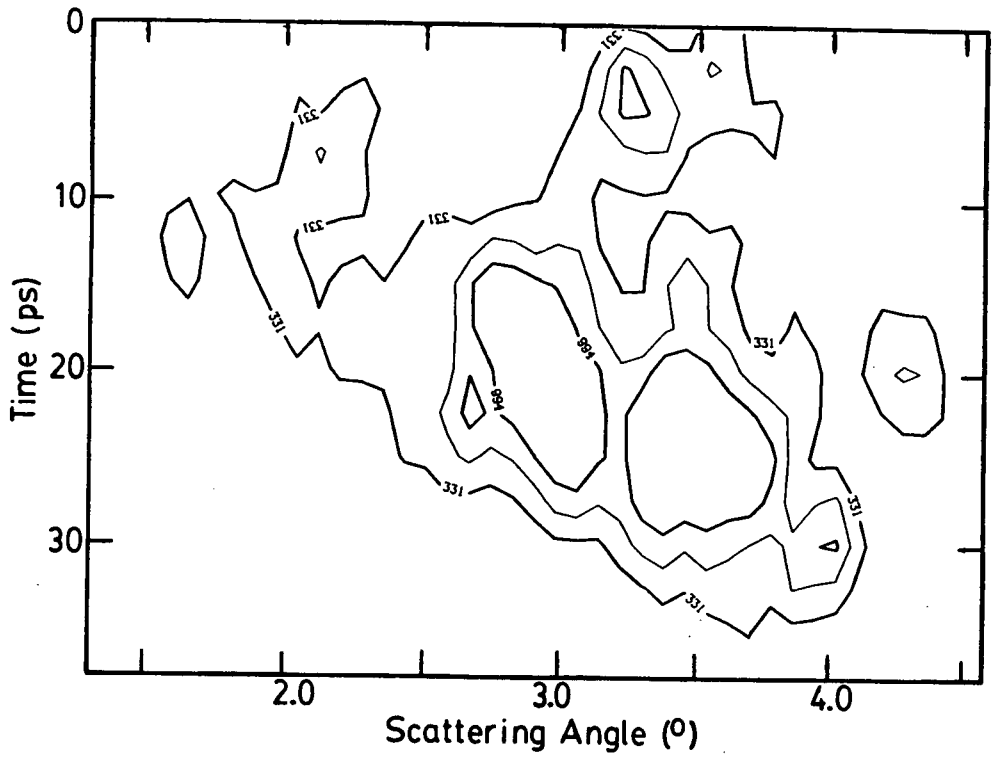

Figure 4-11 Example of wide angle Thomson scattering streak taken at a higher sweep speed.

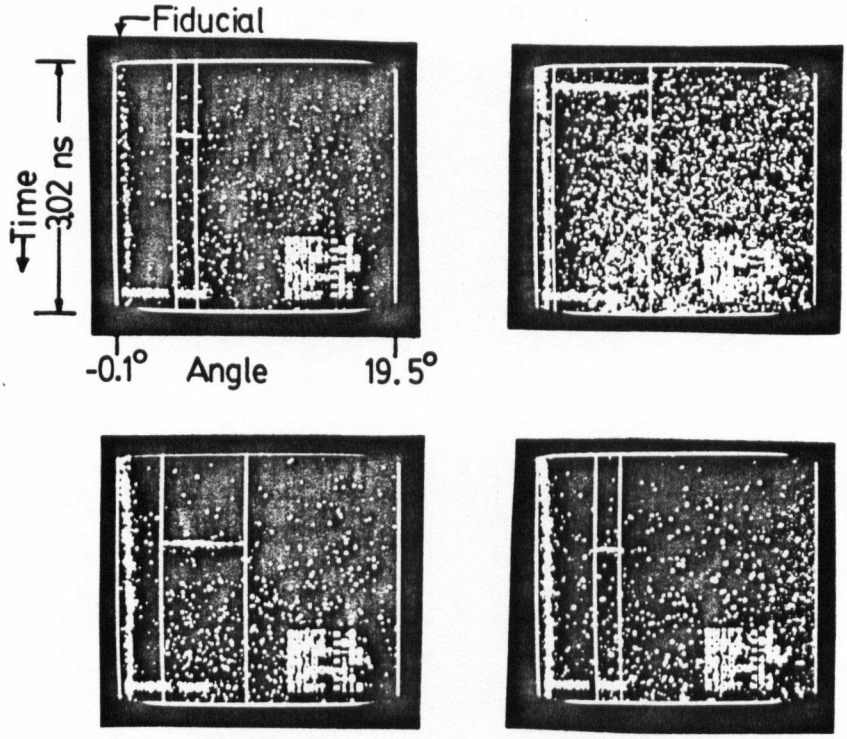

Figure 4-10 Typical streak records from the wide angle Thomson scattering. The scales are the same for all the records. Scattering at angles less than 1.5°was blocked.

4.4 Results from Frequency resolved Thomson Scattering

The frequency resolved Thomson scattering was performed to confirm the wavelength shift implied by the wavevector resolved results. The frequency shift of the scattered light is just the plasma frequency of the EPW probed. In figure 4-12, a typical spectrum is presented. The instrument resolution $\sigma_{ins} = 1.38$nm FWHM is appreciable but the observed width σ_{obs} is much wider than the instrument width alone. A simple estimate, $\sigma^2 = \sigma_{obs}^2 - \sigma_{ins}^2$ suggests the actual width σ is 1.4 nm. This implies a simultaneous appearance of SRS over the density range 0.17–0.19 n_{cr}; this is consistent with the narrow k range observed. (Note that the sample k

spectrum of figure 4-6 is much narrower than the averaged spectrum of figure 4-9.) The dashed line will be discussed in the next chapter. The cut-off in both the k and frequency spectra could be due to the finite aperture of the exit window of the Thomson scattering setup. The exit window cuts off scattering at angles greater than 4.5°which corresponds to density of $0.15n_{cr}$. Figure 4-9 seems to suggest that there are fluctuations present at even lower densities. This lower density regime was not further explored for two reasons. First, other experiments have seen SRS at those densities but not at higher densities. Second, substantial changes to the scattering geometry would have had to been made in order to detect such waves.

The importance of ion acoustic waves in SRS can been seen in frequency resolved Thomson scattering which can show the ion feature (spectrally unshifted probe light) as well as the electron feature (probe light well shifted). An example of this is shown in figure 4-13, a full screen spectrum of the Thomson scattered light seen through the narrow angle geometry. The intensity contours are in steps of 1/4 of the maximum level. SRS starts earlier than the IA waves do, but once the IA waves become well established, SRS is saturated and quenched. The levels of the ion acoustic waves must be quite large since a single interference filter with a rejection ratio of more than 100 was used to reduce the levels of the Thomson scattered light which was scattered from the ion acoustic waves.

The unshifted light is not stray ruby light. If it were, the signal should have started much sooner as the ruby laser was irradiating 2 to 3 ns before the start of the plasma. The ruby laser light also continues to irradiate the plasma for 3 ns after the start of the plasma whereas in the streak records, the unshifted light stops during the sweep. Further, an ion feature has been observed under identical experimental conditions [54] and this feature has the same temporal duration as the feature observed in this work.

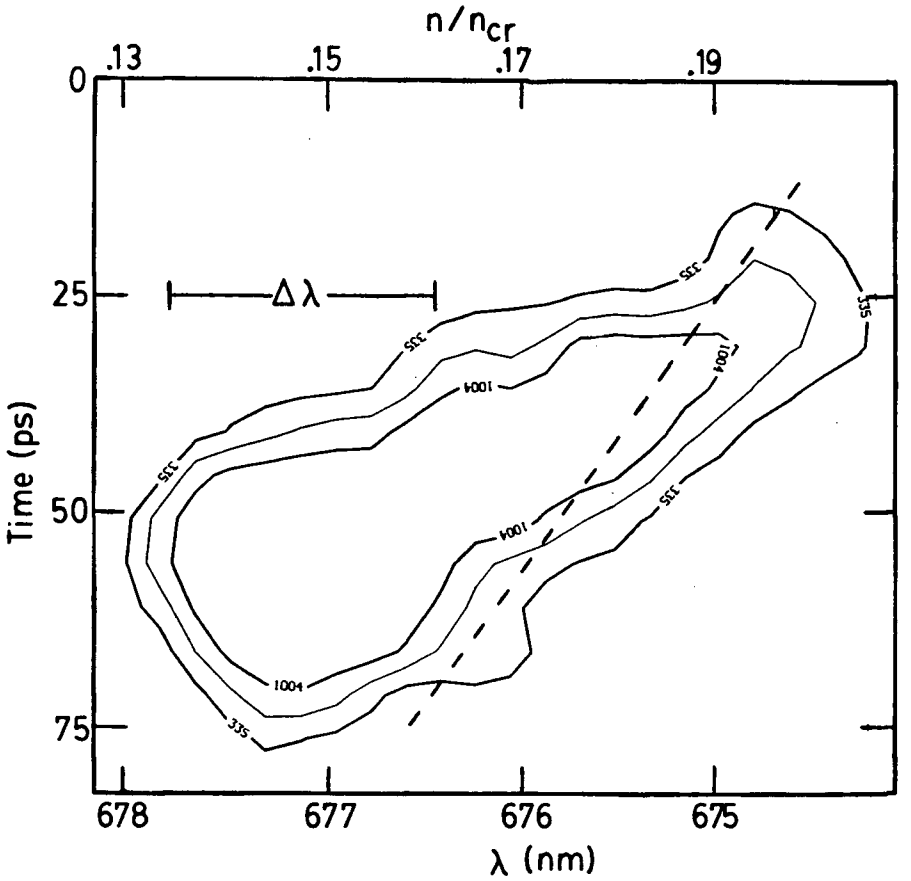

Figure 4-12 Typical frequency resolved Thomson scattering streak record. The intensity contours are in steps of 1/4 of the maximum level.

An interesting density-time effect can be seen in both figure 4-6 and 4-12. As time progresses, SRS seems to shift to lower densities. The typical rate is -0.001 n_{cr} ps^{-1}. Explanations for this will be discussed in the next chapter.

4.5 Scattered Infrared Light

If SRS is present, scattered IR light at frequencies shifted from the incident CO_2 frequency should be present. The results from the Thomson scattering, which examined the epw, suggested that IR associated with Raman scattering from densities 0.15–0.25 critical density should be present.

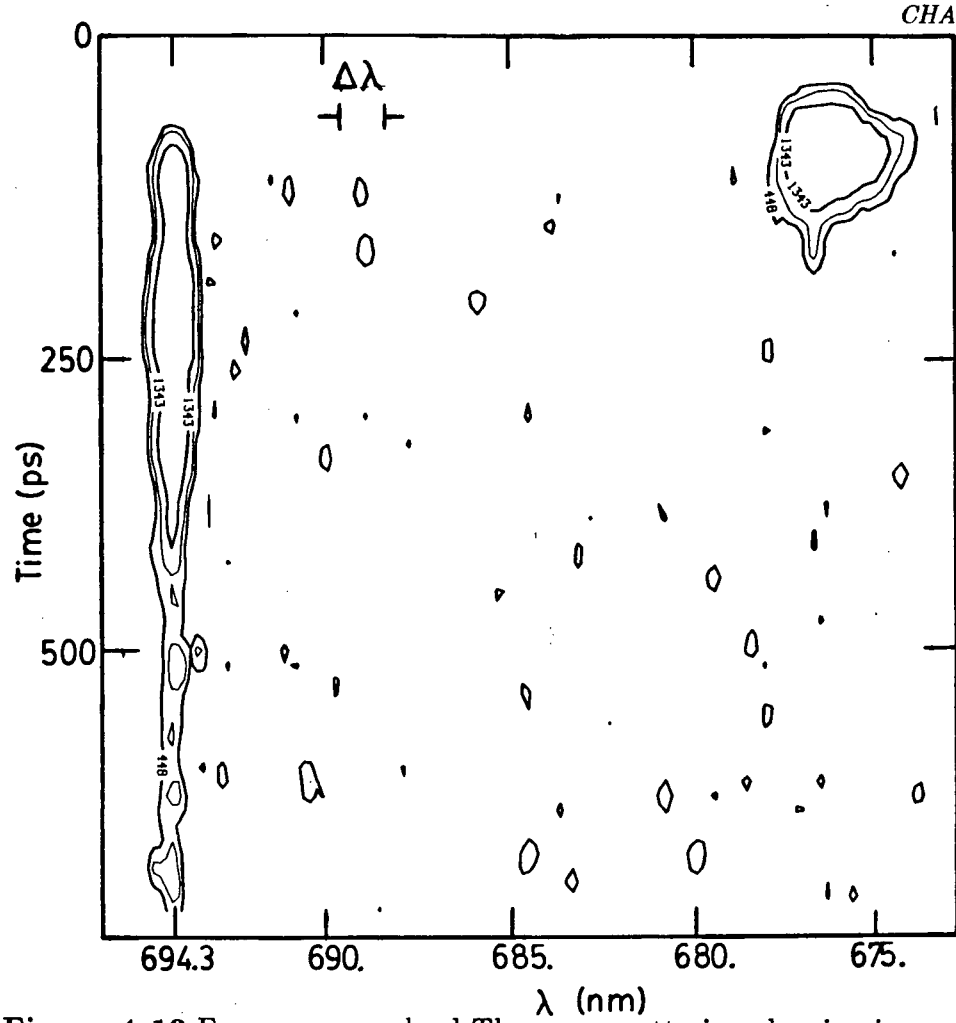

Figure 4-13 Frequency resolved Thomson scattering showing ion and electron features.

A systematic search for the scattered IR light was undertaken at 162°to k_o. (Observations of direct backscatter were not attempted as the thick KCl lens would absorb most of the scattered light.) Spectrally integrated measurements at an angle of 144°to k_o were also performed. The spectrally integrated measurements were summarized in figure 4-1 where the energy dependence of the signal is clearly seen. No temporal resolution was possible due to the limited bandwidth of the detector; therefore, all that can be said is that the IR scattering was less than 1 ns in duration since the time resolution of the Ge:Cu detector used was 1ns. The spectrally integrated reflectivity can be deduced by comparing the signal through one redpass filter S_1 to that through two redpass filters S_2. The filter properties

are such that 70% of any SRS signal, S_{SRS}, is transmitted while less than 0.05% of any SBS signal, S_{SBS}, is transmitted. Since

$$S_1 = 0.7S_{SRS} + 0.0005S_{SBS}$$

and

$$S_2 = (0.7)^2 S_{SRS} + (0.0005)^2 S_{SBS},$$

it follows, given the observed ratio $S_1/S_2 = 2.4$, that $S_{SBS}/S_{SRS} = 1000$. Since the SBS reflectivity is 10% [54], the SRS reflectivity should be 0.01%. This method of estimating the SRS reflectivity assumes SRS and SBS have the same angular distribution. This method gives the reflectivity at 180° ,i.e., where the SBS level is 10%. Out of the cone angle of the CO_2 laser, the SBS level drops rapidly. In fact, at 135°, the SBS reflectivity is only 0.2% and thus the SRS reflectivity at that angle will be correspondingly smaller. Thus, when one deduces absolute reflectivities from the signal size, this angular dependence of the signal strength should be remembered.

The spectrally resolved scattered IR light was also examined with two methods. One way used the 15 micron interference filter. The signal observed this manner was 40% of the total integrated signal. This indicates a large amount of SRS is occuring at densities near 0.1 critical density at an approximate reflectivity of 0.004%. However, IR scattered at these densities was not further explored since, as mentioned earlier, it was the scattering from higher densities (in the so called gap) that was of more interest.

A second spectrally resolving system which used a monochromator was set up. The region from 16 to 22 microns was examined at 1 micron intervals. A signal was found only near 21 microns. At all other wavelengths, the scattered light must be at levels below 10% of that at 21 microns. The wavelength bandwidth of the monochromator, fixed by the exit aperture, is 0.2μm FW. The region near 21

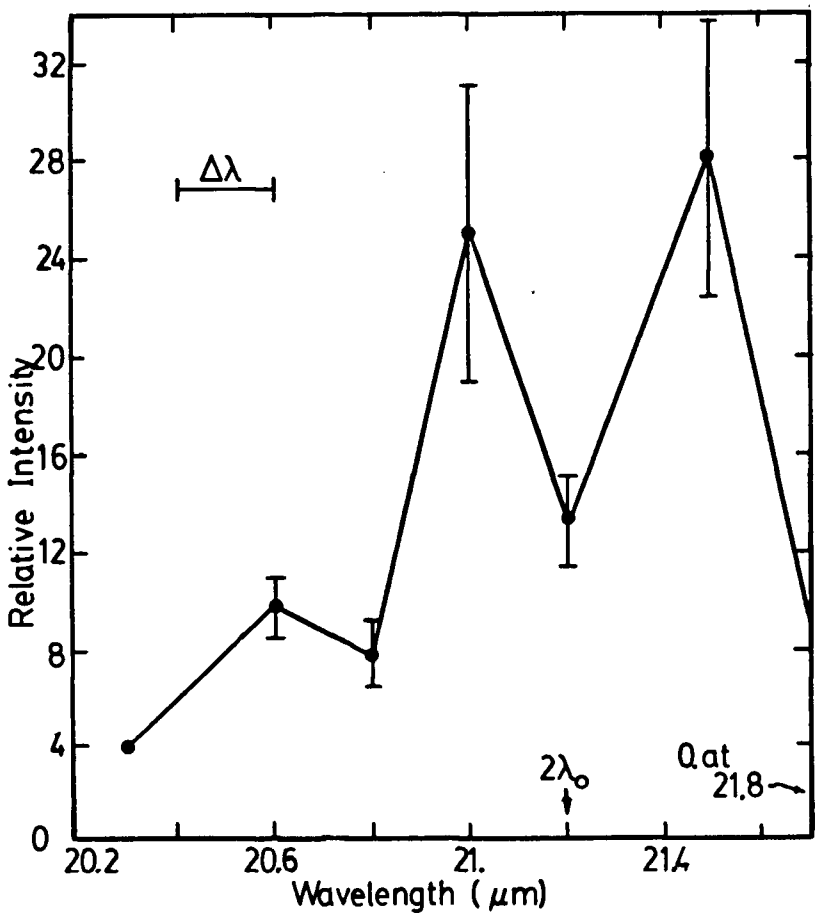

Figure 4-14 Spectrum of scattered IR near $2\lambda_o$.

microns was examined at 0.2 micron steps and the results are shown in figure 4-14. The intensity seems to be split around exactly $2\lambda_o$.

4.6 Simultaneous Observations of Electrons and Plasma Waves

In a CO_2 laser experiment, all the observable aspects of the SRS process can be easily measured. This presents a unique opportunity to correlate these aspects. It is important to correlate the high energy electrons with the SRS as these electrons are one of the main problems in laser fusion schemes.

The electrons can be correlated with SRS in two areas. The number of electrons can be compared with the amount of SRS measured through Thomson scattering or through IR levels. The energy spectra of the electrons can be compared with

the scattered IR spectra or with the the wavevector spectra from Thomson scattering. Both comparisons are important for either large numbers or high energies or both are detrimental to laser fusion schemes.

The simplest comparisons are made between the number of hot electrons at 150keV, N, and the saturated fluctuation level δn or the amount of SRS integrated reflectivity R. In figures 4-15 and 4-16, the relative number of electrons at 150 keV, as measured by the electron spectrometer, are compared with the $\delta n/n_e$ and R. A straight line relation is indicated between ln(N) and the fluctuation level or reflectivity. This is what was predicted by Eqn. 2-29. It is worthwhile noting that, in both cases, a change in the abscissa coordinate by a factor of 2 results in the same fractional increase in ln(N). The relative number of electrons can be compared directly because the same detector located at the same position was used to record the data. The straight lines are least squares fits whilst the error bars in figure 4-15 are estimates in the error for a single shot, due primarily to uncertainties in the signal/fiducial ratio in the Thomson scattering streakcamera data. Each datum represents a shot in which both the number of high energy electrons and either the fluctuation level or the spectrally integrated reflectivity were observed simultaneously.

In order to correlate the number of electrons with the fluctuation level, the Thomson scattering data must be interpreted using the actual (not relative) levels. In Table 4-1, the parameters used to find the fluctuation level via Eqn.3-3 are given. The maximum signal to reference count ratio $N_{signal}/N_{fiducial}$ measured was 12 which corresponds to a fluctuation level of 1%. The largest errors in this level are due to uncertainties in L and σ.

Table 4-1 Parameters to find absolute fluctuation levels

Parameter	Value
N_1	200
N_2	180
Δy	84 μm
f	1
N.D.	5
θ_o	1.8°
σ	0.03mm^2
L	115μm
n_e	0.25n_{cr}
$\delta\theta$	0.00022 rad

(Here, Δ y is calculated for a diffraction limited focus.)

The second correlation of high energy electrons with SRS can be seen through the energy spectra of the electrons compared with the wavevector spectra of the epw. (The prediction of computer simulations is described by Eqn. 2-3.) In this experiment, fluctuation spectra and electron energy spectra were recorded simultaneously with the objective of testing the predictions. In figure 4-17, typical spectra are shown. Electron energy spectra (Fig.4-17(a)) and the corresponding wavevector spectra (Fig.4-17(b)) are given. As the number of electrons in the high energy channel increases, the time-averaged wavevector spectra shift to shorter k (higher phase velocity waves).

This behaviour can be quantified. A temperature k_BT is fitted, as described in chapter 3 (Eqn.3-4), to many spectra of the electron energy distribution. The wavevector spectra require a bit more analysis as there is a range of k vectors to choose from. The shorter k vector corresponding to one-half the square of the maximum fluctuation level was arbitrarily used to find the phase velocity, v_p and in figure 4-18, the k_BT versus $0.5m_ev_p^2$ is shown. The vertical error bars represent the standard errors of at least 4 data points while the horizontal error bars represent the size of the bins used for averaging.

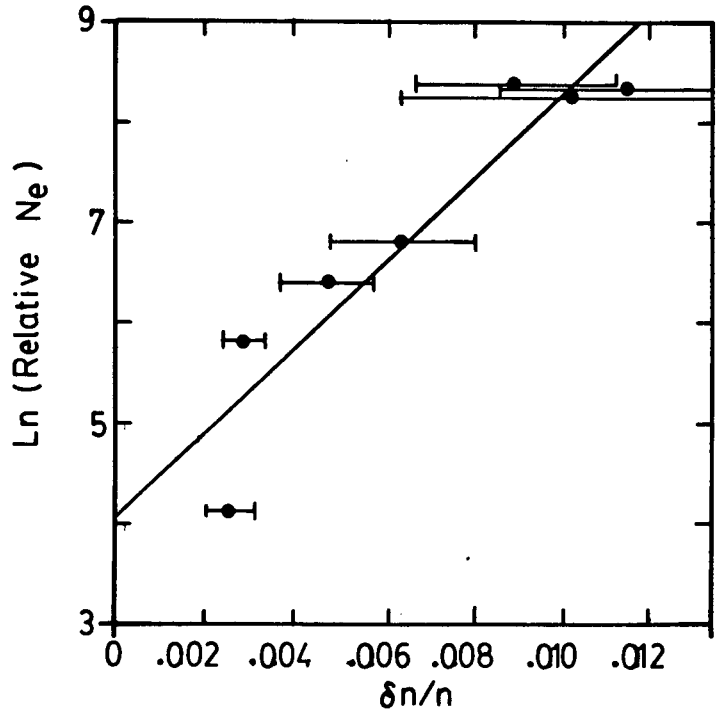

Figure 4-15 Correlation of electron number with the fluctuation level. Eqn.2-29 predicted a straight line relationship on a semilog plot. The prediction was based upon a simple trapping model.

There are convolution effects, since the electrons observed are time and space (density) integrated. There is also a range of EPW responsible for the generation of the electrons. These effects are minimized if averages over many shots, such as those in figure 4-18 are used.

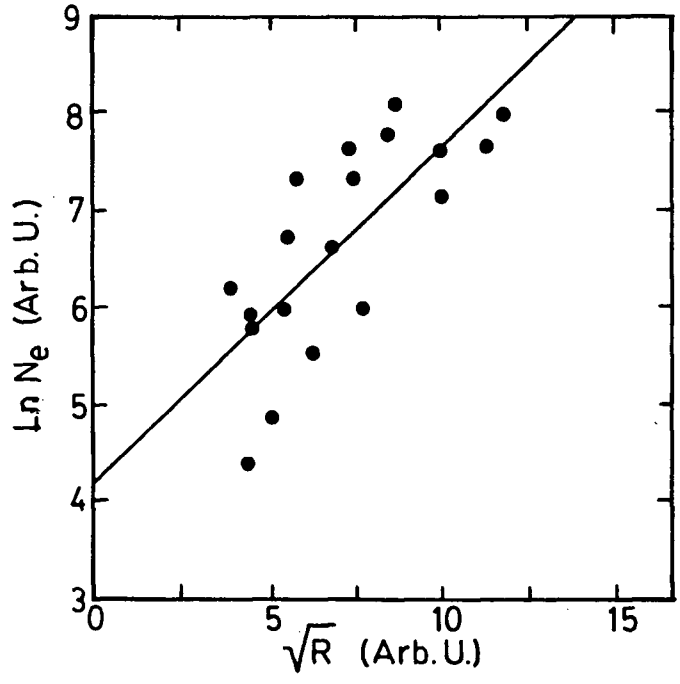

Figure 4-16 Correlation of electron number with the integrated IR level. A straight line relationship is predicted by Eqn. 2-29 if one makes the reasonable assumption that R is proportional to δn.

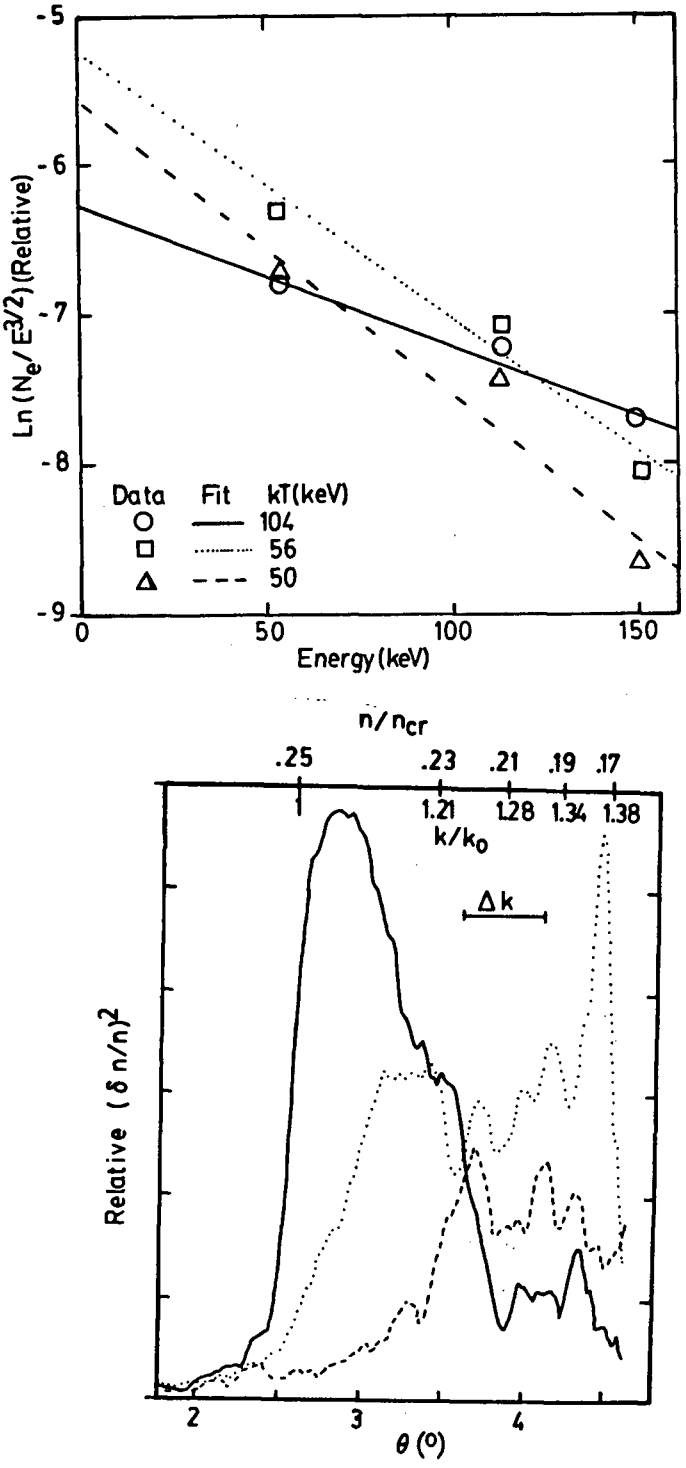

Figure 4-17 Simultaneous electron and wavevector spectra. (a) The electron spectra (b) the k vector spectra . There are three different irradiations shown. As the fitted temperature increases, the wavevector spectrum shifts to higher phase velocity waves.

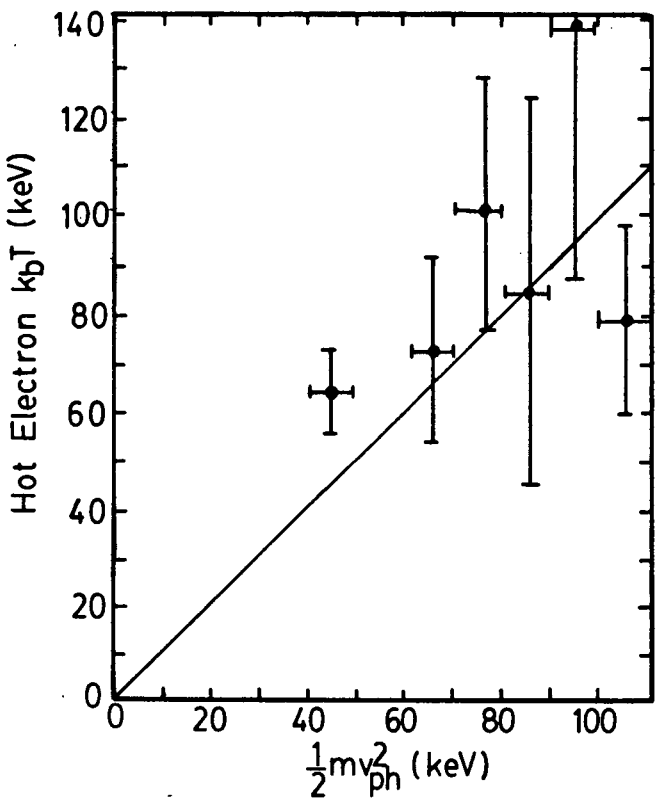

Figure 4-18 The fitted fast electron temperature compared to that expected from the fluctuation spectra. The straight line is suggested by simulations.

CHAPTER 5

Discussion

In this chapter, the main results of my research are discussed and compared with the relevant theories and other experiments. A selfconsistent picture emerges.

5.1 Preliminary Numbers

If one wishes to compare theory to experiment, specific quantities, such as T_e, L, v_o, n_e,etc. all of which must be derived from experiment, must be used. In the following sections, typical values are used extensively to derive orders of magnitude for thresholds, growth rates, etc. In order to avoid repetition and to be consistent, the experimentally measured numbers (which do vary from shot to shot) used in the calculations (unless otherwise indicated) are:

k_BT=300 eV (from Popil [52]),

L=300 μm (measured from spatial Thomson scattering),

v_o/c =0.05 (for a 5J incident laser pulse),

n_e =0.23 n_{cr} (from interferometry [47,60]),

$\delta n/n_o$ = 0.01 (measured with Thomson scattering), and

Z=4 (from Popil [52]).

5.2 Threshold Considerations

Theories of SRS predict that certain threshold intensities must be reached before the interaction proceeds. Many threshold estimates can be made. In this section, these estimates are made and a comparison to the observed threshold is

made. Computer simulations[44] have shown the estimates of thresholds, based upon analytic theory, are quite good. Various theories are available for comparison with the present experiment. The simplest model is the one for an infinite, homogeneous plasma in which the stimulated growth rate must be greater than the damping rate for the waves (Eqn. 2-15). To overcome collisional damping (Landau damping being negligible), an intensity around 6.5×10^9 Wcm^{-2} is needed which, in this experiment, is exceeded by 4 orders of magnitude. In a finite, homogeneous plasma, there is the convective threshold (Eqn. 2-21) which must be exceeded. This threshold intensity is 9.6×10^7 Wcm^{-2} which again is exceeded by many orders of magnitude. However, if the laser intensity on our target is reduced by only a factor of 10, no scattering is seen. This behaviour is a direct result of the fact that our plasma is laser produced and is not preformed. Because of this, a certain amount of the incident energy must be used to form the plasma. Bernard [54] has estimated that this takes about 1 J. In such a plasma, large density gradients are expected and thus, the inhomogeneous plasma theories are more appropriate to use in finding thresholds. There are several regimes for these theories. At $0.25n_{cr}$, the threshold for absolute growth set by Drake and Lee (Eqn. 2-23) is $I=4 \times 10^{12}$ Wcm^{-2}. At lower densities, a threshold for absolute growth (Eqn. 2-22) of $I = 6 \times 10^{13}$ Wcm^{-2} at 0.2 n_{cr} is found. On the other hand, the convective threshold set by Rosenbluth (Eqn. 2-19) at 0.2 n_{cr} requires a γ_o of 6.3×10^{12} s^{-1} (or an intensity of 2.6×10^{13} Wcm^{-2}) is required. It seems the observed threshold of 1.9×10^{13} Wcm^{-2} is above the absolute thresholds at $0.25n_{cr}$, but near the thresholds (absolute or convective) at $0.2n_{cr}$.

Since SRS is observed at the lower densities, there is a discrepancy (less than a factor of 3) between theory and experiment. Other experimenters have noted such a discrepancy, with the theoretical thresholds usually being larger than those experimentally observed, although not all investigators agree on the size of the discrepancy. Elazer et al.[61], Villeneuve et al.[62], Walsh et al.[63] and Turner et al.[64]

report thresholds close to those predicted while Seka et al.[65,66], Shepard et al. [67], Tanaka et al. [68] and Figueroa et al.[69] report thresholds below the theoretical estimates by factors of 5 to two orders of magnitude.

Several explanations have been proposed. The most plausible explanation is that experiments and theory are not being compared consistently. For instance, what intensity should be used - a peak, an average over 60% or 90% energy radius, the instantaneous intensity at the time of the interaction or something else? The theories usually do not consider these practical points. Theorists assume that a plane wave of uniform amplitude is interacting with the plasma. In an experiment, the focussed laser beam can be thought of as a superposition of many plane waves. Is this important? There are effects which can perturb an ideal plane wave so that its amplitude is not spatially uniform. For example, pondermotive filamentation can raise laser intensities locally, perhaps even well above thresholds. This process has a threshold intensity [70] of

$$I_t(\mathrm{Wcm}^{-2}) = [2.5 \quad 10^{15}/L_{\mu m}\lambda_{\mu m}]T_{eV}\, n_c/n$$

which is $10^{12}\mathrm{Wcm}^{-2}$ in our case. Its growth rate is similar to that of SBS and should not be able to increase the intensity of the incident laser beam in the plasma on timescales on which SRS occurs (less than 50ps).

A proper calculation of a threshold requires a knowledge of the plasma density profile. The reason is that the spatial gain in an inhomogeneous medium involves

$$\int_0^{L_{int}} (k_o(x) - k_{epw}(x) - k_s(x)) \quad dx$$

and this depends on exactly how k_o, k_{epw} and k_s vary with x. All of the quoted formulas assumed a linear profile to simplify the calculations whereas real profiles are not necessarily of this form. Figueroa et al. [69] and Villeneuve et al. [62] have

shown that the form of the profile assumed (Gaussian, exponential, parabolic, linear, etc.) affects the threshold calculated (by as much as several orders of magnitude).

Finally, if one uses a convective threshold, such as that of Rosenbluth, some level of growth must be assumed. Rosenbluth used $e^{2\pi} \approx 535$ as the level above which the threshold is said to be exceeded. Tanaka claims a more realistic estimate can be made if a growth of 50 is used which reduces the required intensity by 1.6. In addition, to apply correctly a convective threshold formula, some initial noise level should be measured or calculated. One possible noise source is random plasma fluctuations.[11] A detector may see a signal (e.g. scattered light) but only if this signal exceeds the background levels can it be said SRS is occurring. The results from the Thomson scattering, where saturated fluctuation levels at 50 to 100 times the noise level are observed, suggest Rosenbluth's explanation for any threshold discrepancy is correct. The convective growth threshold calculated under this reduced growth requirement agrees with that observed although it is absolute growth which is observed.

The IR signal observed at $2\lambda_o$ could be a result of the TPD instability. Therefore, an estimate of its threshold intensity must be made. From Simon [24], we find his equation (54) which reduces to

$$I(\mathrm{Wcm}^{-2}) \geq (v_e/c)^2 (k_o L)^{-1} 3.8 \times 10^{18} / \lambda^2_{o(\mu m)}.$$

For our conditions, this reduces to an intensity threshold of 1.4 10^{11} Wcm^{-2}. Thus, the thresholds for both SRS and TPD are exceeded in my experiment and the interpretation of the other results is therefore complicated by this fact.

5.3 Spatial Details

SRS can occur on a density gradient. However, the growth of the instability depends upon the magnitude of the gradient. The plasma length observed can yield some idea of whether absolute or convective growth should be expected. (The

density profile is also important.) The lower limit for (reduced) absolute temporal growth in a finite, homogeneous plasma, $(v_{epw}v_-)^{1/2}/\gamma_o$, is 5.6 microns while the upper limit, v_-/γ_o, is 36 microns. The condition for absolute growth, L much larger than 5.6 μm, is well satisfied and therefore, this type of growth might be expected. Since the observed density scale length is longer than 36 μm, there should be a short period of temporal growth at γ_o, followed by growth at γ_r (Eqn.2-17). This short period (L/v_-), about 2 ps, is a tenth of the observed duration of SRS and, hence, the observed temporal growth should be at γ_r unless nonlinear effects become important. Further, this short period is less than the temporal resolution of the streak camera and therefore, if the waves do grow at γ_o, we cannot observe this growth.

The spatially resolved Thomson scattering gives some idea of how the plasma wave fluctuations vary with position. This is important since the nature of the instability determines how the fluctuations (sometimes called normal modes in the literature) will be spatially distributed. In particular, in a finite but homogeneous plasma, there should be spatial growth. For the determination of the spatial distribution, this finite, homogeneous model of the plasma should be valid since the observed length of the SRS scattering region is much larger than the upper limit for absolute growth. This means the density inhomogeneity is not important at least for this aspect of SRS. In the spatially resolved Thomson scattering, some evidence for spatial growth was found. In figure 5-1, exponential growth in space can be seen which indicates that spatial growth has occurred. (The inset in the figure shows the complete spatial variation of the fluctuation level.) Over 10 shots, an average amplitude Im(k) of $0.026 \pm 0.004\mu m^{-1}$ was found.

A spatial growth rate in amplitude can be calculated from Eqn 2-18 with the parameters mentioned in section 5.1. The result is $0.28\mu m^{-1}$ which is a factor of ten larger than observed. It must be emphasized that this prediction is for a finite, homogeneous plasma. This prediction of the spatial growth rate is the only one

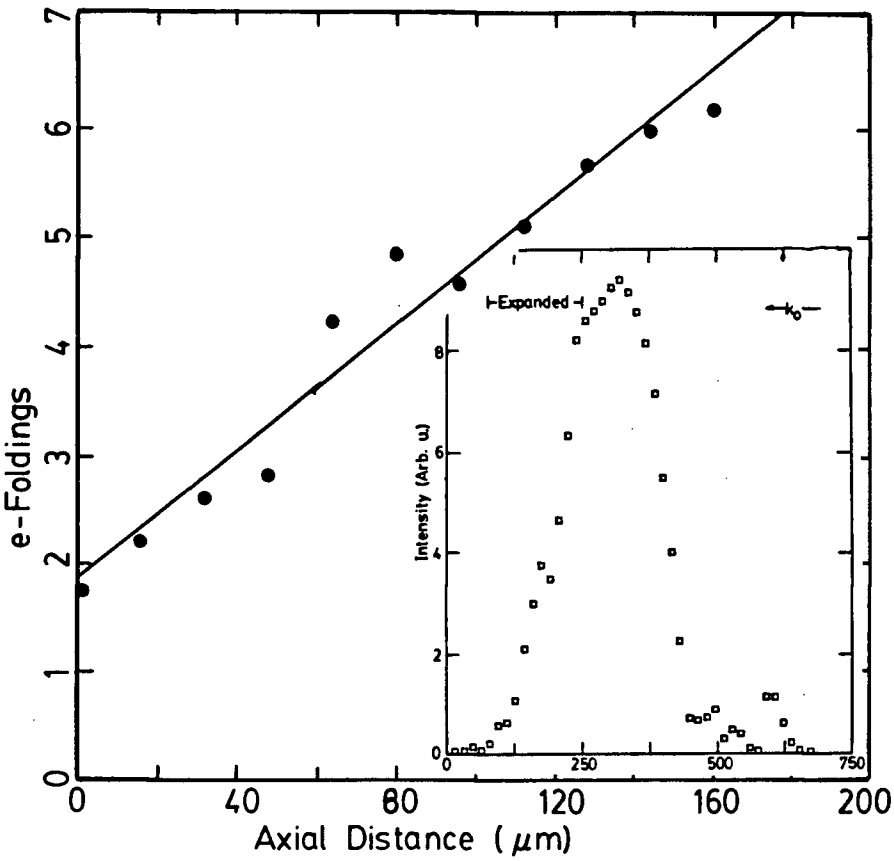

Figure 5-1 Evidence for spatial growth of SRS. The intensity of the Thomson scattered light is plotted as a function of spatial position. A straight line on the semilog indicates that possible spatial growth is occuring. The inset shows the full spatial extent of the scattering on a linear plot.

that I am aware of. The possible reasons for this difference will be discussed with the temporal growth rates, also measured (which show a similar discrepancy).

The spatial results obtained should not be compared directly with other experiments. For comparison purposes, the differences in the wavelengths of the incident laser light must be taken into account. The simplest scaling parameter is L/λ_o. In the present experiment, this ratio is about 20 to 40. Most other experiments [61,64,65,66,68,76,81] are performed at shorter wavelengths (less than one micron) for similar L. Effectively, the other experiments have longer plasmas and therefore,

higher levels of SRS might be expected from them. Experiments which used CO_2 lasers have been done with ratios of 30 (Villeneuve et al.[62]) and more than 10000 (Offenberger et al.[72], Watt et al.[73,74]) although the latter two experiments were performed at much lower densities (less than $0.01 n_{cr}$). All of the above experiments, except for the experiment of Villeneuve et al. [62], report much higher levels of SRS than those observed in this work. The plasma size is probably the most important reason for this difference.

5.3 Temporal Growth and Behaviour

In the section on spatial growth, it was decided that the instability should be absolute and should grow at the reduced temporal rate (Eqn. 2-17) in accordance with the theory of Forslund et al. [8]. In this section, this hypothesis is examined.

Temporal growth is characterized by an exponential growth in time. In figure 5-2, the plasma wave amplitude can be seen to grow exponentially which indicates that there was absolute growth. The figure shows the increase of the scattered light intensity at $\theta = 3°$. In figure 5-3, growth rates from similar plots are shown as a function of wavevector. One notices that the growth rate does not vary within the standard deviations, at least over the range investigated, and, by inference, does not depend upon density dramatically.

For comparison to the measured growth rates, various theoretical growth rates can be calculated. The theoretical growth rates for an infinite plasma (Eqn. 2-11) are about 30 times too large. Other theoretical growth rates are lower than the growth rate for an infinite, homogeneous plasma. Since the plasma is not infinite, the next level of complexity requires the rates to be calculated in a finite, homogeneous plasma (Eqn. 2-17). This was done and the results are shown in figure 5-3 where they are divided by 10 (the solid curve). The theoretical rates do not vary greatly with density, at least over the region of most interest. The measured rates are about 7 times lower than expected from this theory.

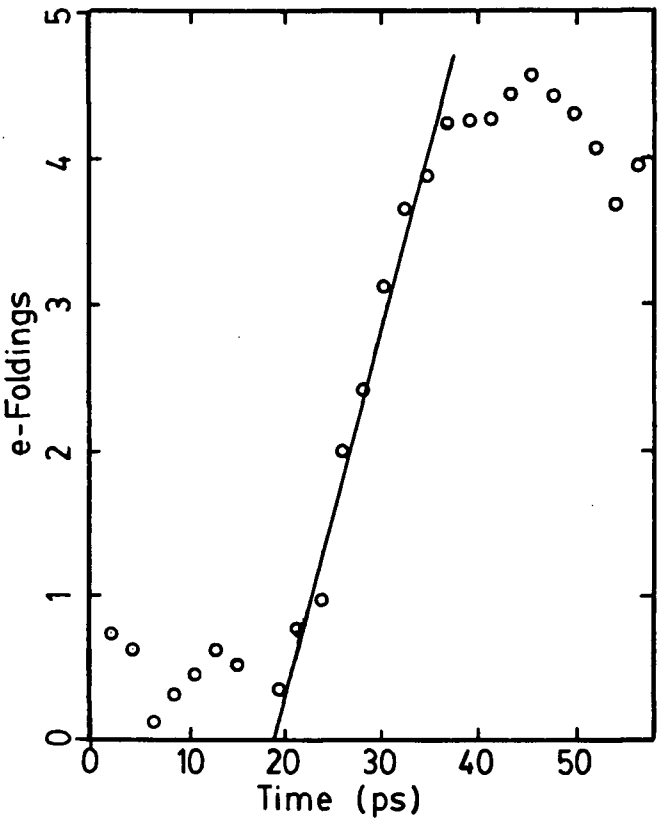

Figure 5-2 Evidence for temporal growth. The plots shows the intensity of the Thomson scattered light as a function of time. The straight line on the semilog plot indicates that temporal growth has occured.

Other complications can further reduce the theoretical growth rate. From the comparison of the plasma light timing with the timing of the scattering, it was found that SRS occurs early in the laser pulse. Since the exact intensity at the time of the scattering was not known, an average laser intensity was used in the calculation. Further, the measured growth rates presented were averaged without any regard to incident laser intensity. Thus, it did not seem reasonable to calculate the growth rate at intensities different from the average intensity used in the experiment. However, since the growth rate is proportional to $\sqrt{I}$, a lower intensity results in a lower growth rate. This could account for (at worst) a factor of

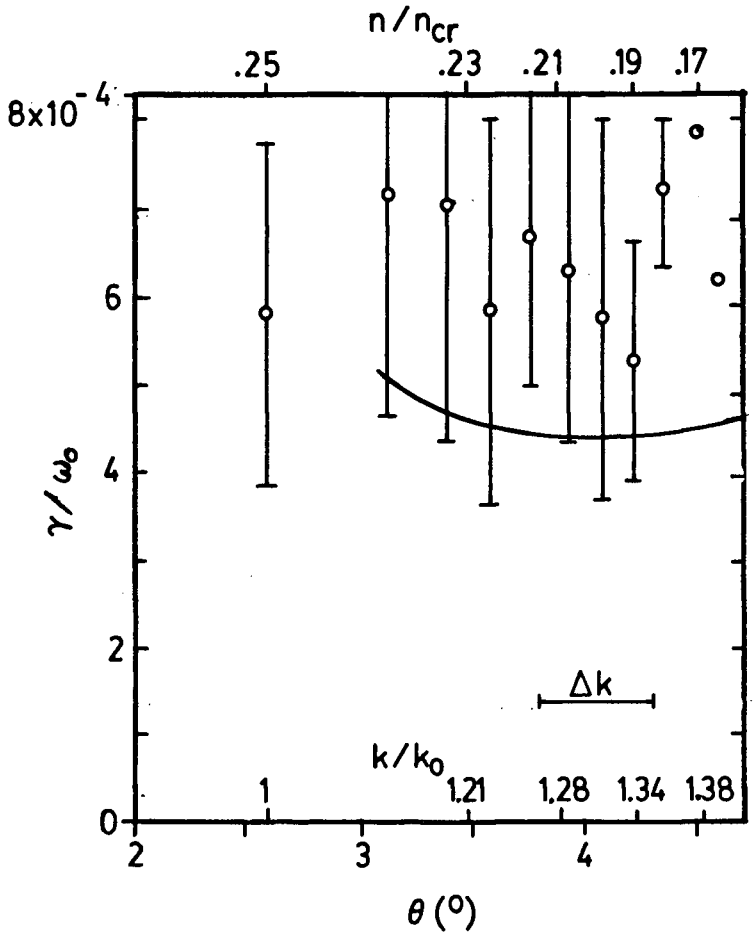

Figure 5-3 Experimentally measured growth rates. These growth rates were determined from plots such as the one in Figure 5-3.

3, since I is constrained by threshold and plasma production considerations. An inhomogeneous plasma will also result in a lower growth rate. Again, since there are variations in the scale length, a simple calculation of the growth rates ignored any effects of inhomogeneities. If the full expression of DuBois (Eqn. 2-20) is used, the inclusion of a typical inhomogeneity observed in the experiment will reduce the rate to 25% of the rate in a homogeneous plasma. This term accounts for the wavevector mismatch mentioned earlier. Any damping will also reduce the growth rate, but Landau and collisional damping alone are too small to have any significant influence. In an infinite, homogeneous plasma, the scattered IR light can be generated into directions other than direct backscatter. The growth rate for this sidescattering is

lower than that for direct backscatter. In the present experiment, the Thomson scattering indicated that some sidescattering was occurring. These sidescatter effects which change the value of γ_o by $\sin(\pi/2-\psi)$ (see Eqn.2-11) have only a small effect on the final growth rate since the maximum ψ expected is 135 °. Inclusion of this in Eqn. 2-11 can reduce the theoretical growth rate over the range of scattering observed to 70% of the backscatter rate (at most). Some combination of all these effects can reasonably reduce the expected growth rates to levels at which theory and experiment can be made to agree although the exact mixture cannot be stated. Even given the uncertainties in the experimental parameters which are needed to calculate the growth rates, the net result is still that the measured growth rates are of the correct order of magnitude as those rates predicted by theory.

A consistency between the temporal and spatial growth rates can be attained if a slightly higher electron temperature (approximately 375 eV) and a much lower laser intensity (approximately $4.0 \times 10^{11} \mathrm{Wcm}^{-2}$) are postulated. By choosing this temperature, the ratio of the theoretical to the measured temporal growth rates is equal to the same ratio for the spatial rates. By choosing this intensity, the ratio can be reduced to one. This consistency also requires the plasma to be finite and homogeneous. More theoretical work should be done on the spatial growth rate in an inhomogeneous plasma before a realistic comparison to the present results is undertaken.

The temporal behaviour of SRS is interesting for another reason. Some simulations show that there should be modulations in the level of the scattering. The simulated modulation rates are of the same magnitude as can be resolved by the present experiment and therefore the streak records should be examined for evidence of such modulations. Short period (about 15 ps)modulations were found (see figure 4-6). The reason for the short period fluctuations is not known. The reappearance in the exceptional case (figure 4-8) may be related to similar fluctuations observed in the TPD instability and SBS.

Temporal behaviour of the SRS scattered light has been observed in other experiments, although growth rates of SRS in a laser produced plasma have never before been measured. SRS has always been subnanosecond in duration, with the shortest (instrument limited) pulses reported being 20ps long [75]. Modulation times of 50ps to 500ps have been reported [75,65,66,64,76,63,67]. In a similar CO_2 laser-plasma interaction experiment [62], the pulse widths were 100ps and separated by 200-500ps. The reasons for the bursts of SRS are not at all clear. Two suggestions have been made in the literature. These are variations in the incident laser intensity [64] and localized, moving density plateaus [66]. The intensity of the laser beam used in this experiment is believed to be temporally smooth; no variations on the instrument limited scale of 500ps were seen (see figure 3-1). The spatially resolved Thomson scattering did not reveal any evidence for moving, localized density plateaus. (These plateaus would be a result of the TPD profile modification process. The flattened regions would propagate away from $0.25n_{cr}$. Temporal behaviour would then be associated with the periodic saturation, quenching and reappearance of TPD.) Modulations have been observed in simulations in which periods of 100 laser periods (about 3 ps) were found but no detailed explanation for such behaviour was given. [2]

Since the two explanations above do not seem to be applicable to this experiment, another reason must be found. One is that ion acoustic waves disrupt the SRS EPW and that modulations in the IA waves are reflected in SRS. The origin of these large amplitude ion acoustic waves is of some interest. Are they a result of the SRS-TPD processes or are they a result of SBS? Since SBS has a lower threshold intensity than SRS does, one might suspect that SBS starts before SRS does but grows at a lower rate for a longer time and might be the source of ion acoustic waves when the laser intensity reaches the threshold for SRS. However, there is a complication to this simple picture – it takes a certain amount of energy to produce a plasma in which these instabilities can occur. A typical laser rises from 0 to 5 $\times$

10^{13} Wcm^{-2} in 1.2ns. The required amount of energy to form a plasma, approximately 0.8J, will have been deposited into the target by 0.7ns at which time, the laser intensity will be 3×10^{13} Wcm^{-2}. This intensity is well above the observed thresholds for SBS (about 10^{12} Wcm^{-2}) and SRS (about 1.9×10^{13} Wcm^{-2}). Since the interactions cannot proceed before a plasma has formed, a good approximation to the physical situation is that SRS and SBS start simultaneously at 0.7ns. In the next 20ps, both instabilities grow in time at the measured rates of 10^{10} s^{-1} for SBS and 10^{12} s^{-1} for SRS. The relative e-foldings at the end of this 20 ps will be 0.2 for SBS and 20 for SRS. Thus, SBS will be relatively unimportant and any large amplitude ion acoustic waves observed in this experiment at the time of the SRS interaction must have some other origin. In preformed plasmas, this plasma production complication does not enter into consideration. In such cases, it is best to examine each problem individually. Two such experiments have been presented in the literature. Rozmus [77] and Offenberger [78] have shown that for a large, low density plasma, SBS can occur before SRS does whereas Walsh [63] showed experimentally that, in a preformed plasma which has conditions similar to the present experiment, the presence of large amplitude IA waves stops SRS. The results presented here so far hint that comparisons with this latter case are appropriate. The connection of ion acoustic waves to SRS will be discussed as a saturation mechanism later. Ion acoustic waves have been associated with the saturation of TPD.

5.4 Density Behaviour

One important point about SRS which has not been discussed yet: in many previous experiments [62,64,65,66,67,68,69,79], there is a gap in the scattered EM spectrum, corresponding to scattering from densities approximately 0.1 to 0.24 n_{cr}. This experiment probed two aspects of SRS which should be present, namely, scattered IR light and enhanced electron plasma waves. In this section, the density fluctuations found by wave vector and frequency resolved Thomson scattering are

examined to determine if the fluctuations are enhanced for densities in the region of interest.

Upon examination of the typical streaks presented in chapter 4, it is immediately obvious that the EPW are enhanced at densities below $0.25n_{cr}$. This can be seen in both the wavevector and frequency resolved streaks. This means, in the present experiment, that the gap does not exist as far as the plasma wave fluctuations are concerned. In the next section, the levels of the IR that should be associated with these fluctuations are estimated and compared with the observed IR spectra.

In Chapter 2, a hypothesis was put forward that the SRS should propagate to lower densities at a rate fixed by the plasma wave group velocity and the density gradient scale length. The present experimental data will be examined to see if there is any evidence for this. In both figures 4-6 and 4-12, SRS behaves qualitatively as predicted. On a quantitative level, the dashed line in these figures represents the rate at which the density should change if the convective model (Eqn. 2-25) is applied with the parameters L=400μm, $n = 0.2n_{cr}$, and T=300eV. In both cases, the observed rate is faster than the predicted rate of -0.0006n_{cr} ps^{-1} which is a result of the shot-to-shot variation in the density scale length. In a plasma with a steeper density gradient, the rate is predicted to increase. Thus, the convective hypothesis seems to be quantitatively consistent with the data.

The convective model is interesting in that it proposes that the EPW generated at density n_S increases the noise levels for EPW at lower densities. As was mentioned in chapter 2, the EPW initially propagate up the density and are reflected at their critical surface. The EPW then propagate down the density gradient. As the EPW propagates from the higher to lower densities, its wavevector must become longer since its frequency does not change. This means that the wave damping via Landau damping becomes greater. By a slight rearrangement of the

plasma wave dispersion relation, one finds that

$$n(x)/n_S = 1 - 3(kv_{th}/\omega_{epw})^2$$

where $\omega_{epw} \approx \omega_p(n_S)$. Generally, Landau damping is important when kv_{th}/ω_{epw} is about 0.3 . At this point, the damping becomes greater than the growth rate for SRS (for the modest intensities used in this experiment). This limit suggests that the plasma waves can propagate to a minimum density of $0.73n_S$. This lower density cut-off is observable in some shots. For example, in figure 4-6, the wavevectors start at $0.25n_{cr}$. The limit expected is $0.18n_{cr}$ and the limit observed is $0.19n_{cr}$. In figure 4-12, the plasma waves start at $0.19n_{cr}$ and end at about $0.15n_{cr}$. The limit expected is $0.14n_{cr}$. In figure 4-12, this cut-off may be coincidental since the interference filter and the angular limitations of the Thomson scattering also limit the observable spectrum. In figure 4-6, these effects should not be responsible for the cut-off since the cut-off point in that figure is far from the cut-off set by the Thomson scattering setup. This further supports the convective model.

The temporal behaviour of SRS has been observed in other cases. In each case, SRS always proceeds to shorter wavelengths, although the explanations for this vary. Seka et al.[66] claims that the temperature change in time is responsible. Differentiating the dispersion relation for an EPW (from page 6), one finds

$$\frac{1}{\omega_p}\frac{d\omega_{epw}}{dt} = (\frac{k}{\omega_p})^2\frac{3k_B}{2m}\frac{dT_e}{dt}.$$

Using the measured $d\omega_{epw}/dt = -0.22ps^{-2}$ we find a $dT/dt = -100eV \quad ps^{-1}$. This rate is too large and the wrong direction. A reasonable estimate would be an increase of 300eV in 1.2ns. Therefore it is unlikely that a changing temperature is responsible for the observed effect.

A second effect was suggested by Figueroa et al. [69], namely, the plasma density might be changing. Results from the interferometry indicate that the plasma

density varies very little at times less than one nanosecond. This mechanism does not seem to be responsible for the present results. This shock wave should not change the density on 20ps timescales.

5.5 Scattered Infrared Light

In chapter 4, the results presented showed that scattered IR light was found only near 21μm and in a broad band near 15μm. However, the Thomson scattering indicated that there should be more IR light than this. In this section, an attempt is made to reconcile the Thomson scattering results with the IR results. The observations seem to imply that enhanced EPW are driven at densities below $0.25n_{cr}$ yet there is a lack of detectable scattered light corresponding to those densities. In addition, there are large signals observed at $2\lambda_o$ and at wavelengths corresponding to approximately $0.1n_{cr}$. These results are discussed in the following order. First, a plausible origin for the signal at $2\lambda_o$ is given. Then, the levels of SRS at lower densities is estimated from the results of the Thomson scattering. Finally, these estimates are compared with the IR detector threshold. It is shown that a detectable signal should have been generated. The gap is to be explained. To this end, the current explanations are outlined and applied to this experiment. A variation of one of these explanations is shown to be consistent with the results observed.

The origin of the $2\lambda_o$ signal is probably not due to SRS, but rather due to linear mode conversion for the TPD instability epw. In this mechanism, the EPW propagates up a density gradient until it reaches its turning point at which point the wave no longer propagates. The electrostatic wave energy is transfered the electrons and the electrons reradiate the energy as electromagnetic waves. This process is called inverse resonance absorption [92]. Only frequencies present in the EPW can reproduced in the EM wave. Therefore, it is necessary to look only at mechanisms which cause splitting in the frequencies of the epw. In other experiments [75,61,80,65,66,81,79,82,67,68,83,84,69], frequency splitting has been observed near $2\lambda_o$.

The explanations given for such experiments are applied to this experiment. Two hypotheses are usually put forward; the peak to peak splitting can be due to either a finite temperature [93]

$$\Delta\lambda_{pp}(\mu m) = 4.4 \times 10^{-3}\lambda_o(\mu m)T(keV)$$

or a finite magnetic field [93]

$$\Delta\lambda_{pp}(\mu m) = 1.87 \quad 10^{-2}\lambda_o^2(\mu m)B(MG).$$

The finite temperature effect is a result of small corrections for the EPW dispersion of the SRS EPW which were previously ignored in the thesis. A temperature of 8 keV or a magnetic field of 200 kG is required to explain the observed splitting of about 0.4μm. This 8 keV temperature is unreasonable since the measured temperature is only 300 eV. Although no magnetic field was looked for in this experiment, other experiments [84a] have reported fields in excess of 2MG although those experiments were performed under very different conditions. A field of 200kG is reasonable since a rough estimate made in chapter 2 showed that, for our conditions, the thermoelectric effect could generate a field of on the order of 100kG. A field of this magnitude will change the temporal growth rate by $\pm$15%. A third possible explanation can be proposed. Since there are large amplitude IAW present, a coupling of these waves with the EPW would result in sidebands being generated at $\omega_p \pm \omega_{ia}$. However, the observed frequency splitting is 10 times the splitting expected for IAW of $k_{ia} = 4k_o$. Sideband splitting has been observed for light scattered at $3/2\omega_o$ in a recent experiment [85]. Another possible source of the splitting is due to electron trapping. The scattered light will be modulated at the bounce frequency [11] of the electrons in the wave i.e.

$$\omega_b = k_o v_e(\delta n/n)^{1/2}.$$

This leads to a modulation of 4.3×10^{11} s^{-1} which is narrower than the observed splitting of 1.7×10^{12} s^{-1}. Thus, we conclude that the observed splitting is consistent only with the presence of a magnetic field. Further experiments would be necessary to prove this definitely.

The Thomson scattering results qualitatively imply that SRS scattered IR should be present. In this section, a quantitative estimate of the IR signal size is attempted. Further, this estimated power will be compared to the minimum power the detector can measure. The amount of scattered IR can be estimated since the Thomson scattering was absolutely calibrated. It is important, however, to keep track of the difference between power reflectivity and energy reflectivity. Theoretical formulas predict power estimates whereas experiments measure energies. The conversion from power to energy requires a time estimate. In the following, SRS is assumed to occur for 10ps, which is approximately the minimum duration of the Thomson scattering. The first estimate of the amount of scattered light is made under the assumption that the IR light is simply Thomson scattered from the observed fluctuations. In section 2.5, an expression was given with which the power scattered by a given fluctuation per solid angle and in a given frequency range can be calculated. This calculation is independent of the wavelength of the light which is to be scattered. In section 3.3, this formula was applied to ruby laser light Thomson scattering and an estimate of the absolute scattered power could be found. If the CO_2 laser is used in place of the ruby laser, it is straightforward to show that

$$\left(\frac{dP_s}{P_i}\right)_{CO_2} = \left(\frac{dP_s}{P_i}\right)_{Ruby} \frac{\Delta\omega_{sCO_2}}{\Delta\omega_{sRuby}} \frac{\Delta\Omega_{CO_2}}{\Delta\Omega_{Ruby}} \frac{L_{CO_2}}{L_{Ruby}}$$

where $\Delta\omega$ is the bandwidth of the scattered light which can be detected, $\Delta\Omega$ is the solid angle into which the detected scattered light was emitted, and L is the length of the scattering region. The maximum $(dP_s/P_i)_{Ruby}$ can be calculated with the method outlined in chapter 3 and with the parameters of Table 4.1. The result is

1.5 10^{-8}. The term $\Delta\Omega_{CO_2}$ is set by the collection optics of IR diagnostics. The calculated solid angle detected is given in figure 3-12(c) as a function of wavelength. In the calculation, a typical solid angle of 0.0016 sr is used. The solid angle of the ruby laser scattered light which was detected is set by the angular range of a single pixel (0.00022 rad) at a distance of 30 cm from the target and by the height of a mask opening (1 cm) at the same distance. The $\Delta\Omega_{Ruby}$ found this way is (0.00022 x 1 cm)/ (30 cm) or 7.3 10^{-6} sr. The frequency range accepted by the IR diagnostics was set by the exit aperture of the monochromator. This reduces to 8.4 10^{11} rad s^{-1}. The frequency range for the ruby laser Thomson scattering can be estimated two ways. The most conservative estimate would set $\Delta\omega_{Ruby}$ equal to the bandpass of the interference filter. This is not used since the frequency resolved Thomson scattering (e.g. figure 4-12) indicated a much narrower range is more appropriate. Accordingly, the frequency window used is 1.2×10^{13} rad s^{-1} which corresponds to a wavelength range in the scattered ruby light from 675nm to 678nm. I also assume that the scattering lengths for the ruby and carbon dioxide lasers are equal. When all these estimates are combined, one finds that the typical IR power reflectivity is 2.2×10^{-7}. For a typical incident power of 2.5GW, we find that 5.5 nJ of scattered IR energy should have reached the detector. This should be a lower limit. A second estimate of the amount of scattered light, based upon the Manley-Rowe relations (Eqn.2-32) indicates that there should be 60μJ of scattered light but the direction of this light cannot be specified. This estimate is based upon the amount of energy contained in the observed plasma waves.

These estimates are now compared with the sensitivity of the Ge:Cu detector used in the experiment. For signals of duration much less than the *RC* time of the detector, the output signal is proportional to the input energy, not the input power. For *RC* about 1ns, a noise voltage of 5mV, and a power sensitivity of 0.2A/W into 50Ω, we find the minimum detectable energy of U_{min} = (1ns) (5mV)/(0.2A/W 50Ω) of 1pJ. Even given the roughness of this estimate, we can note that it is still many

orders of magnitude below the estimate of the scattered energy. Thus, I conclude that a signal should have been detected.

The lack of scattered light is consistent with many experiments (e.g. Ref.65,66 and references therein) although most of these same experiments also observe a signal at $2\lambda_o$ (never before in a CO_2 laser experiment, however). The explanations put forward have varied widely, but can be reduced to two. The majority of the investigators believe profile modification is important. This may be important for quenching the instability. However, it is difficult to see how this mechanism can explain the gap in this experiment. If the profile has been modified to such an extent that SRS does not occur at certain densities, it should not be possible to observe EPW generated at said densities. Other investigators believe that the source of noise from which SRS must grow is important. This noise can be electromagnetic or it can be electrostatic. For the source of the electromagnetic noise, blackbody radiation has been suggested. Since in the long wavelength region this noise is proportional to $1/\lambda^4$, the IR at longer wavelengths generated by SRS will have to grow from a much smaller noise level. The electrostatic noise is calculated in standard textbooks [11] and is given by (after integration over all frequencies)

$$(\delta n)^2 = N\frac{(k\lambda_D)^2}{1+(k\lambda_D)^2}$$

where N is number of electrons in the plasma volume. As k becomes larger, the noise level becomes larger. Since longer plasma wavevectors are needed for SRS phasematching at lower densities, SRS growing from electrostatic noise should be more predominant at low densities. In either case, the actual gain (including losses due to inverse bremsstrahlung) at a given wavelength requires an integration over actual density and temperature profiles. Seka *et al.* [65,66] were able to reproduce their results quite well using hydrodynamic simulation results for the density and temperature profiles and assuming SRS grew from blackbody noise.

A novel explanation was proposed by Simon and Short [86,87] who pointed out that a pulse of fast electrons moving in a cold plasma leads to an enhancement of plasma waves whose phase velocities lie on that part of the distribution where $\partial f/\partial v > 0$. Spectra which are frequently identified as SRS are, by this theory, the result of ordinary Thomson scattering of the CO_2 laser from these enhanced waves. They state enhanced scattering occurs if the denominator in their scattering crossection is zero or negative. The expression for this denominator is given by

$$\nu_{ei}/\pi^{1/2}/\omega_{epw} + (E_p/T_c)^{3/2}\exp(-E_p/T_c) + f_h\alpha^{3/2}y^2(y-1)\exp(-\alpha(y-1)^2)$$

where $E_p = 0.5m_e(\omega_{epw}/k_{epw})^2$, $\alpha = 3T_{hot}k_x^2/2/T_ck_{epw}^2$, $y^2 = 2E_pk_{epw}^2/(3k_x^2T_{hot})$, and k_x is the component of k_{epw} along the direction of a pulse of hot electrons. In 1-D, the problem becomes easier to examine since k_x will then be just k and E_p has already been calculated (see figure 2-4). In the present experiment, the fraction of hot electrons, f_h, is 0.01 at maximum[60]. The observed hot electron temperature, T_{hot}, is about 100keV. If various scattering angles and electron densities are tried in this formula, no region of enhanced scattering is found. The reason for this is that the collisional term in the denominator (the first term of the above expression) is totally dominant. For the denominator to be zero or negative, the final term must be large and negative. While there is no problem in making the term negative (i.e. making y less than 1), the exponential term makes the term small compared to the collisional term. This can be clearly seen by noticing that α is on the order of 500 for the temperatures specified earlier.

The theory of Simon also predicts enhanced plasma waves. However, it is felt that the standard theory adequately explains all the observed phenomena (except for the lack of IR light from low densities). This does not preclude further more detailed experiments to further test the theory of Simon et al. It may be the correct explanation.

The IR light may be scattered in some unexpected direction. Shepard [67] has observed that Raman scattering is preferentially scattered within the cone angle of the incident laser light. As mentioned earlier, the severe attenuation of KCl (and the problem of eliminating SBS) prevented examination of this direction. Refraction effects could reduce this preferential scattering. If the density gradients are parallel to the wavevector of the incident laser light (as they are in this experiment at the time of the SRS interaction), refraction effects will be small.

There is one aspect of SRS which I believe has not been completely examined although Seka et al. [65,66] have included the effect in their calculations. This has to do with the propagation of the scattered IR to the boundaries of the plasma. It seems evident that one solution to the inconsistency of the EPW / IR results is the possibility that the scattered light is being absorbed as it transverses a large region of plasma before reaching the detector. In particular, if the scattered light must pass through a region of cold, dense plasma, inverse bremsstrahlung absorption can reduce the signal appreciably. In a plasma, the inverse bremsstrahlung coefficient [87a] is given by

$$k_{ib}(\mathrm{cm}^{-1}) = \frac{7.8 \times 10^{-9} Z n_e^2(\mathrm{cm}^{-3}) \Lambda}{T_{eV}^{3/2} \nu^2 (1 - \nu_p^2/\nu^2)^{1/2}}$$

which can be a function of position. In particular, the signal which starts off at I_o on one side of a slab of plasma of thickness L is reduced to

$$I = I_o \exp(-\int_0^L k_{ib}(x)dx).$$

In a plasma with density, thermal and ionization gradients, the absorption coefficient is certainly a function of position. To see how important this effect was, the absorption was calculated for SRS generated on an isothermal, linear density ramp. In this model the density varies from quarter critical density to 0 in a distance L. The frequency of the scattered light was calculated at each point on the ramp,

assuming $\omega_s = \omega_o - \omega_p(x)$ and that the light transversed only the distance from its origin to the plasma boundary with the light scattered from quarter critical density layer transversing the entire plasma. Figure 4-13 shows the escaping fraction of light generated at a given density. It is clear that light generated at the higher densities is severely attenuated. This attenuation is also a sensitive function of the temperature of the plasma. A temperature of 300eV has been assumed previously but this temperature is actually temporally averaged. Further application of this model requires the exact temperature at the time of the SRS which is not easily measurable. Computer simulations for the gas jet show that, early into the laser pulse, the electron temperature is less than 100eV. In addition, the heating model used by Popil [52] assumed that the electron temperature in the bulk of the plasma grew linearly with time during the first 1.2ns, i.e. during the rise time of the incident laser pulse. Whatever the temperature is, the plasma should be spatially isothermal as the thermal conductivity of a hot plasma is large enough to permit thermalization on times less than 10ps. (This can be seen qualitatively by noting the collision period for a 30eV plasma is about 3 10^{-13}s. The plasma thermalizes after a few periods.)

There is one obvious inconsistency with this model — a signal is observed which must originate near the quarter critical layer. From the averaged Thomson scattering results, SRS can be seen to have similar fluctuation levels at all densities in the range examined and hence, similar levels of scattered infrared light are expected over the corresponding wavelength region. However, the IR signal observed externally is the product of both the attenuation and the actual amount of IR present at its origin deep inside the plasma. At $0.25n_{cr}$, additional light at $\omega_o/2$ can be generated as a result of the linear mode conversion of the TPD plasma waves. Stokes scattering of the incident CO_2 laser light from the TPD plasma waves can also generate additional $2\lambda_o$ light. In either case, the IR light at $\omega_o/2$ will be

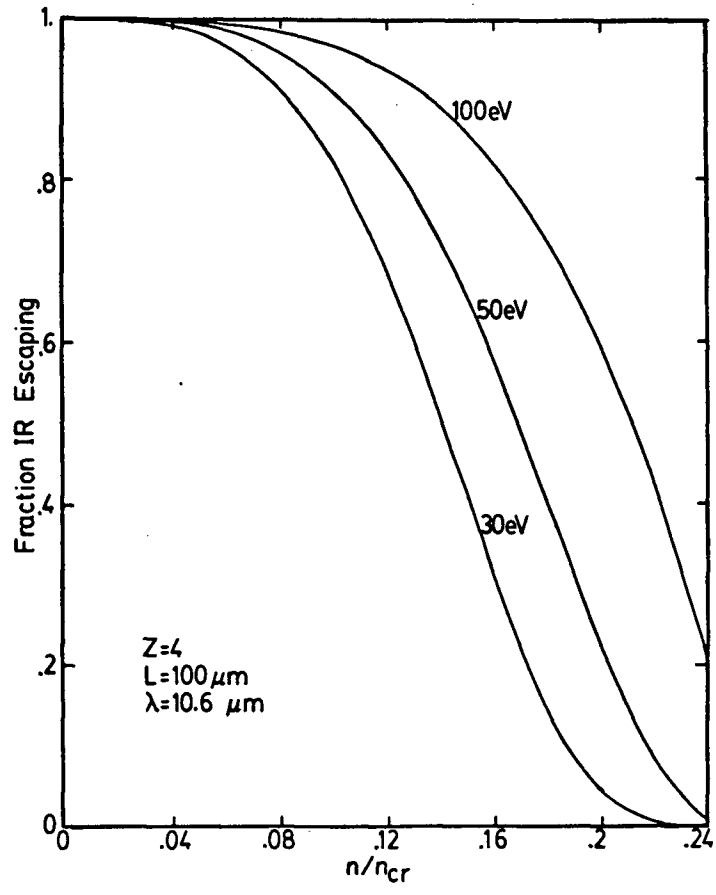

Figure 5-4 Absorption of SRS IR in a isothermal density ramp. This was calculated for 10.6μm light incident on a plasma which has a density ramp from 0 to $0.25n_{cr}$ in 100μm and has an average Z=4. Light generated at a given density has a frequency $\omega_s = \omega_o - \omega_p$.

enhanced over the IR light at shorter wavelengths. The amount of electrostatic energy in TPD waves of wavevector $4k_o$ with a fluctuation level of 10% and which are contained in a volume r_o in radius and 20μm long is comparable with the estimate of the energy in the SRS EPW i.e. O(μJ). This is the maximum amount of energy available for conversion from the electrostatic mode to electromagnetic mode. The parameters quoted for TPD were measured in a previous experiment [91] performed on this plasma.

5.6 Saturation and Competition

SRS was shown to grow exponentially, but eventually the plasma wave must saturate. There are many saturation mechanisms which will be discussed in the following. In an experiment, any combination of the mechanisms could be present and it may not be possible to separate their effects.

One possible saturation mechanism is profile modification. Previous work at this university showed some indications of this mechanism, based upon an interferometric study of the plasma. Since the profile is modified by the pondermotive forces setup by the beating of the EPW generated by the TPD instability, an independent check of this mechanism could be performed. Wide angle Thomson scattering was set up to scatter of SRS epw, as well as those generated by the TPD instability. In figure 5-5, a summary of this experiment and the previous work is given. The range of observation is shown as a dashed line while the range where waves were actually seen is plotted as a solid line. The contour for zero growth i.e. the threshold curve is shown as a dotted line. This line was calculated from the growth rate of Langdon (Eqn.2-12) for I= $3.3 \times 10^{13}\mathrm{Wcm}^{-2}$ with Landau damping (Eqn.2-14) at k_BT=700eV (from Ref. 91) and the inhomogeneous damping of Simon (Eqn.(51) of Ref. 24) for L=20μm. (Simon's damping reduces to $\omega_o/(8k_yL)$.)

Thomson scattering at angles greater than 9° was never observed in over 100 shots. This indicates an absence of large TPD wavevectors in the present experiment. Threshold considerations do not seem to be an adequate explanation as there is a large region where the growth rate should certainly be positive yet no EPW were observed in this region. Of course, this assumes that all the contributions to the growth and decay of the TPD were included in the calculation of the threshold contour. When the previous work is compared with this one, an interesting observation can be made: both cutoffs appear at the same k_x value of $\approx 5/2k_o$. By wave vector matching for the TPD instability a wave with $k_{x2} = -3/2k_o$ must be present. (The k_y of these two waves are equal in size and opposite in direction.)

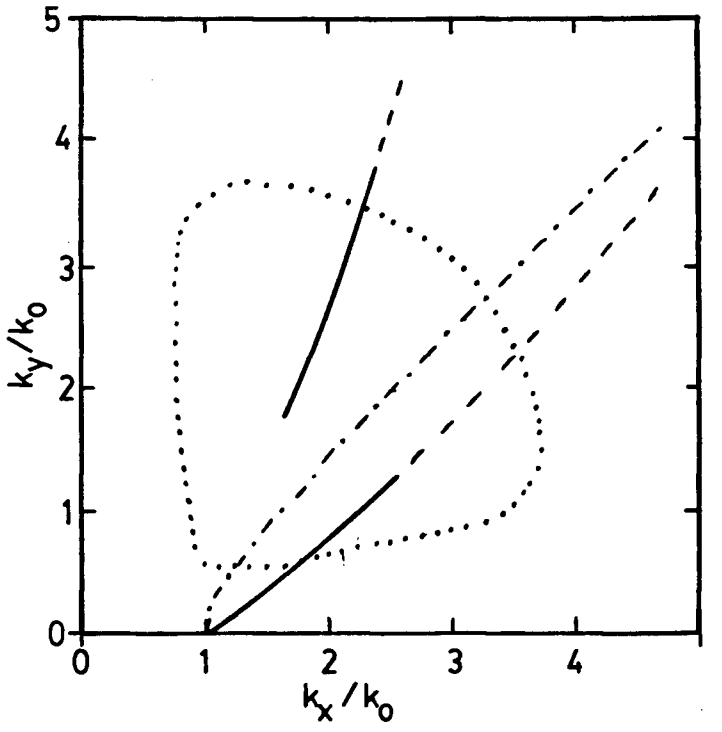

Figure 5-5 Summary of wide angle Thomson scattering. The upper solid-dashed curve is from Ref.91; the lower solid-dashed curve is from the present work. The dot-dash curve represents the contour of maximum growth for SRS-TPD in a homogeneous plasma in the absence of damping (Eqn.2-13). The threshold for TPD is given as a dotted line. In the lower solid curve the wavevectors of TPD and SRS have not be separated. The upper solid curve is entirely TPD wavevectors.

Ion acoustic (IA) waves of $4k_o$ parallel to k_o have been observed and assigned to the decay of the TPD instability. This is shown in figure 5-6 which is reproduced from Bernard [47]. Since the *difference* between the two EPW wavevectors is also $4k_o$, it is believed that IA waves are closely connected with the saturation of SRS as well as TPD. The proposal here is that the EPW generated at quarter critical density start at $k = k_o$ and proceed to longer wavevectors (Figure 4-6 shows the start of such behaviour) but stop when $k_{1x} - k_{2x} \approx 4k_o$ and $\omega_{ia} = \omega_1 - \omega_2$ at which point,

the EPW of SRS decay into an IA wave and an EPW travelling in the opposite direction. This prevents further growth. The wave vector matching for this process is shown in figure 5-6(b).

The importance of ion acoustic waves on SRS is also seen in figure 4-13 where large amplitude IA waves were seen at the same time as the SRS waves but once the IA waves became well established, SRS was quenched.

It thus seems that the ion acoustic waves are responsible for the saturation and quenching of SRS. The exact connection between the ion acoustic waves and the saturation of SRS is now discussed. There are at least two possible mechanisms. Rozmus [77] showed that the presence of large amplitude IA waves causes a frequency shift in the EPW where the resulting frequency mismatch can drive SRS off resonance (i.e. $\omega_{epw} \neq \omega_o - \omega_s$). SRS can still occur at off resonance conditions but the growth rate is much reduced. Far from resonance, the stimulated growth rate will drop below the threshold rate and SRS stops. A second approach, discussed by Karttunen [27,28], has the EPW of SRS decaying into another EPW and an IA wave. The scattering condition for this is $k_{epw1} \rightarrow k_{epw2} + k_{ia}$. In a well underdense plasmaan for backscattering, $k_{epw1} = 2k_o$ and the frequency matching condition for the plasmon decay with the highest growth rate requires that $k_{epw2} = -k_{epw1}$ and $k_{ia} = 2k_{epw1}$. Although little energy is transferred to the ion waves, the scattered (or decay) EPW now has the wrong direction to continue in the primary SRS process. The Karttunen model predicts a saturation of the SRS reflectivity R at a value of

$$R = \frac{\pi^2}{4} \frac{k_{epw2}}{k_{ia}} \left(\frac{k_{epw1}}{k_s}\right)^2 \left(\frac{v_e}{c}\right)^4$$

which for the present experiment is about 10^{-6}. The growth rate for this decay (Eqn.2-22) is also large enough for the decay to occur on 10IV2790ps scales.

Simulations have also shown that the presence of SBS, a source of strong IA waves, leads to a reduction of SRS. A simple simulation, performed by Barr [89] who

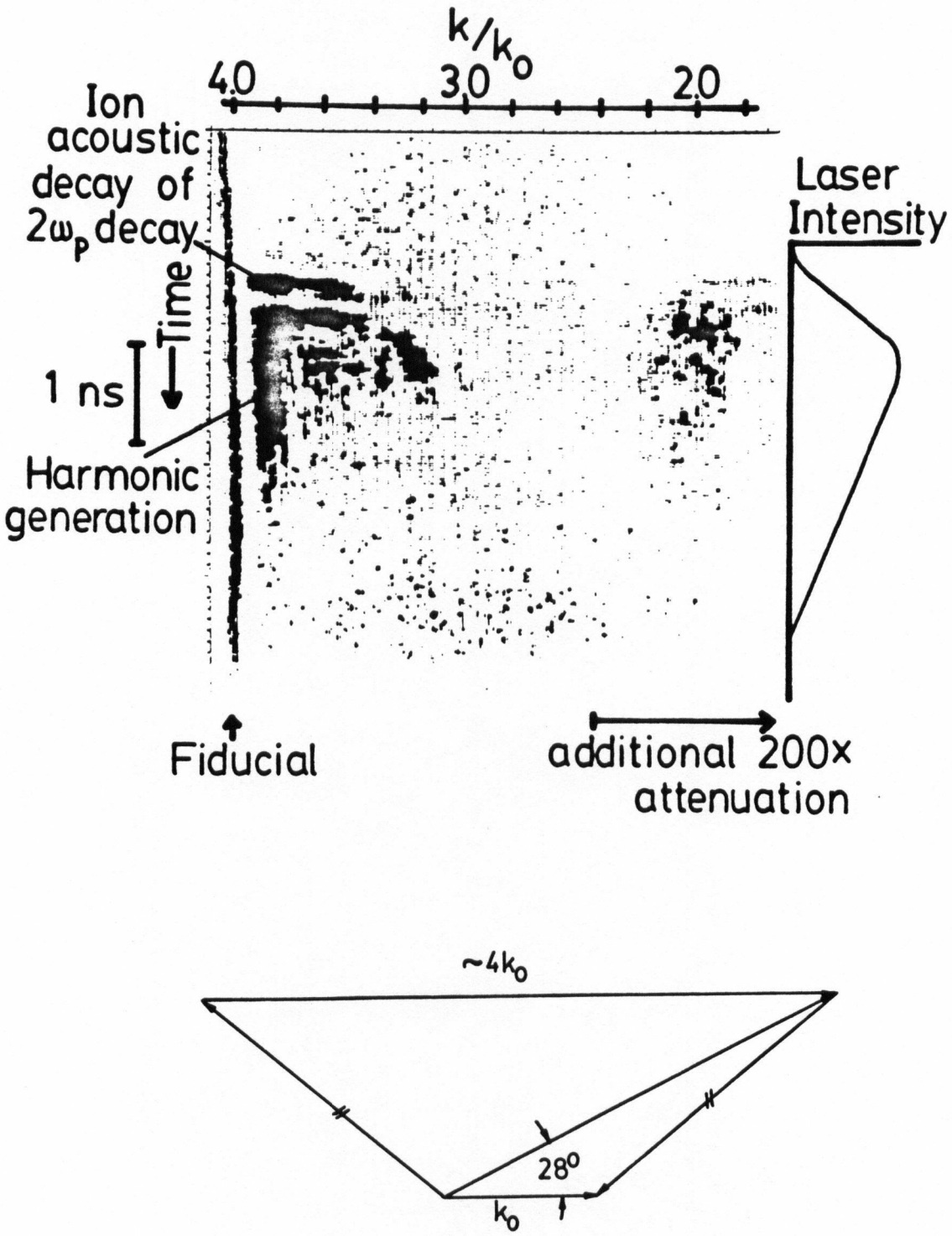

Figure 5-6 Ion acoustic waves from TPD saturation. (a) The wavevector record at the ion acoustic frequency. (b) The wavevector matching process involved.

superimposed a sinusoidal ion density ripple on a plasma, showed that a fluctuation level of 15% is sufficient to quench completely SRS. Since IA waves of this level are eventually present[47], it is reasonable to expect SBS to saturate SRS. Barr was able to show that the growth rate of SRS in the presence of an ion density ripple of depth $\epsilon = \delta n/n_o$ reduces to

$$\gamma = \gamma_o\Big(1 - \frac{q^2}{32(k_{epw}/k_o - 1)^2}\Big)$$

where $q = \epsilon/(6k_o^2\lambda_o^2)$. His simulations also showed that the scattered SRS light would be modulated in frequency by the frequency of the ion acoustic waves. In this experiment, modulation of the scattered light at $2\lambda_o$ was observed. However, the influence of ion acoustic waves was not responsible for the observed modulation. This was shown section 5.5. Other simulations [2], in which ions are not fixed, show reduced levels of SRS when compared to identical simulations in which the ions were fixed. Finally, yet other experiments [90,63] show that large amplitude ion acoustic waves can saturate the epw.

The saturation mechanism which is most likely for SRS in the present case is the effect of ion acoustic waves but there are other mechanisms which must be discussed. Since high energy electrons are observed, the mechanisms of electron trapping and enhanced Landau damping due to the population of fast electrons should be mentioned.

Electron trapping [32] can saturate SRS because it acts as an effective damping on the large amplitude EPW. The energy of the waves is transfered to the kinetic energy of the trapped electrons and damping of a wave is defined as a removal of energy from the wave. This mechanism is not important in the present case as the maximum trapping levels ($\delta n/n = 1\%$, corresponding to a trapping potential of 1keV), are too small to capture significant numbers of electrons. The observed number of fast electrons is puzzling since there are very few electrons in the tail

of a Maxwellian distribution which could be trapped to produce the hot electrons. A non-equilibrium population of velocities may be established because the slower, larger amplitude EPW from the TPD instability may move more electrons into the velocity regime where the EPW from SRS can trap and further accelerate them. This is, however, highly speculative.

A significant population of high energy electrons, perhaps a result of the electron trapping in the TPD plasmons, can saturate SRS through a different route [2]. There is an additional damping of SRS if a hot electron tail is present. In the absence of hot electrons, an exact solution of the nonrelativistic dispersion relation (in the absence of a laser field) shows that over the range k_o to $3k_o$ the frequency of the EPW is ω_p (within 3%) while the damping is much less than $10^{-6}\omega_p$. If a 1% population of fast electrons at 100keV is added, the situation changes. The frequency remains near ω_p but the damping grows to levels between $6 \times 10^{-3}\omega_p$ at k_o to $4 \times 10^{-4}\omega_p$ at $3k_o$. (The approximation, Eqn.2-26, give similar results in this range.) The reason for this large effect is quite simple. Landau damping is resonant phenomena between waves at v_{ph} and particles at a mean speed v_e which becomes large when $v_{ph} \approx v_e$. The added 100keV electron's velocity is nearly resonant with that of the EPW generated at $0.25n_{cr}$ and even a small population can affect the damping greatly.

Since $\omega_p \approx \omega_o/2$, the excess damping is approximately $3 \times 10^{-3}\omega_o$. This rate is of the same order of magnitude as the observed growth rates. This damping may be partially responsible for the reduced growth, but is not large enough to quench SRS. When this damping and the growth are comparable, it is necessary to include the effect of the laser field. This would entail solving the dispersion relation of Drake [9] generalized to a 2 temperature electron distribution.

The fraction of hot electrons used above is based upon the total number of fast electrons observed. This fraction is time integrated. However, the number of electrons associated with the TPD instability grows exponentially with the duration

of the instability (up to 1 ns)[91]. Therefore, the number of hot electrons actually present during the short duration of SRS will be much less than 1% and the damping due to them will be much lower than calculated. Hot electron damping should not saturate SRS in this experiment.

5.7 Connection between SRS and high energy electrons

We have seen that SRS grows at various densities and discussed the mechanism which saturates and quenches the instability. In the section on saturation, electron trapping was dismissed as a saturation mechanism. This is not to be interpreted as a statement that electron trapping is unimportant. Indeed, electron trapping is responsible for the generation of high energy electrons. Both the number and energy distribution are well correlated with the electron plasma waves which produce the hot electrons.

The first item to be discussed is how the number of electrons are related to the level of the density fluctuations. In chapter 2, a simple trapping model was presented which suggested there would be an exponential relationship between the electron number and the fluctuation level (Eqn.2-29). For the data in figure 4-15, the predicted slope (at 0.24 critical density)is 423. The slope found experimentally is 400 which is surprisingly good agreement. It should be pointed out that the predicted slope is quite sensitive to the density chosen. The slope ranges from 570 at 0.25 critical density to 230 at 0.2 critical density. The same trapping model can be applied to figure 4-16, provided the reasonable assumption that the reflectivity R is proportional to the square of the fluctuation level is made. This assumption presumes that the scattering level is small (see chapter 2.5). A conveniant comparison to figure 4-15 is allowed if the plot against $\sqrt{R}$.

The TPD decay instability can also trap and accelerate electrons by the same mechanisms as SRS. However, if the trapping model is applied, the predicted increase is much slower than for SRS. This is because the predicted slope is pro-

portional to k_{epw}^{-2}. Since the plasma waves due to the TPD are $3k_o$ or longer[91], at $0.25n_{cr}$, the slope will at least 9 times smaller. This does not agree with the observed slope.

There is alternate relationship between the number of hot electrons observed and the reflectivity which is a result of the Manley-Rowe relations. These relations predict that the energy in the EPW is proportional to the energy scattered. If a constant fraction of the energy in the EPW is transfered to fast electrons, then the energy contained in the hot electrons will be proportional to the energy scattered. Further, if the energy distribution of the hot electrons is constant, then the number of hot electrons at a given energy, N, will be proportional to the reflectivity, R. Other experiments [84,86,66] have observed such a linear relationship over more than 3 orders of magnitude of variation in R. Our instruments do not have this dynamic range and therefore, it cannot be stated whether this limit has been reached .

Simulations have shown that the hot electron energy distribution is approximately Maxwellian with a temperature $k_BT = 0.5m_ev_{ph}^2$. In this experiment, the electron plasma waves and the electron energy distribution were observed simulataneously. In figure 4-18, the results shown indicate that the simulations give a reasonable prediction of k_BT.

The comparison of the electron energy spectrum to the wavevector spectrum has never been done before but other experiments [73,74,88] the connection. In some of these experiments [88], the maximum density of the plasma could be controlled and the electron spectra (or equivalent x-ray bremsstrahlung spectrum) were observed. Higher k_BT were obtained as the plasma density approached quarter critical density. In different experiments [73,74], the scattered EM radiation was used to infer a k_BT which was compared with the k_BT fitted to the electron spectra observed at the same time. The same behaviour was seen. In summary, the simulation predictions of k_BT have been confirmed in many ways – through the variation of the plasma

density, through the study of the scattered EM radiation and, from the present work, through the study of the epw.

CHAPTER 6

Summary and Conclusions

A summary of the SRS process is given, as I believe it to be. The original contributions are explicitly outlined in the second section. The thesis ends with suggestions for further work, based upon questions which arose in the course of this work.

6.1 The SRS Process

Stimulated Raman scattering is a process in which an electromagnetic wave, incident upon a plasma, decays into a scattered EM wave and an electron plasma wave. The interaction involves a feedback which enhances the scattering. SRS starts when the incident EM intensity is near the threshold value. Estimates of this intensity can vary by as much as an order of magnitude. After the threshold intensity is exceeded, the instability grows exponentially. The convective or absolute nature of the growth is determined by the plasma size and the incident intensity. If the plasma is sufficiently long, the growth is absolute and exponential growth in both space and time can be expected. As the waves grow in amplitude, other effects saturate the instability. The influence of ion waves is the primary cause of saturation. Pump depletion, electron trapping and enhanced Landau damping due to hot electrons are secondary processes. Profile modification, which happens on

a longer timescale, is responsible for the quenching i.e. the disappearance of the instability.

An essential component of SRS is the scattered EM wave. It is not essential that this wave escape the plasma; it need only be present over the interaction region. As this scattered wave propagates to the plasma boundaries, it is absorbed and may not escape from the plasma. This gives rise to the gap observed in the spectrum of the scattered IR light. The weak signal at $2\lambda_o$ is due to the two-plasmon decay instability. Linear mode conversion of the TPD EPW could generate a large amount of light and a small fraction of this light might escape the plasma.

The alternate explanation for the results, the enhanced Thomson scattering theory of Simon et al., could possibly explain the results. It is felt, however, that this is not the case since the standard theory of SRS (from chapter 2) explained all the observed data (threshold, growth rates, frequency and wavevector of the plasma waves observed, etc.) except for the observed lack of IR light. This explanation for the lack of IR light is unknown. Simon's theory is the first one to explain the gap.

Associated with SRS is the generation of high energy electrons. These electrons are a result of trapping and wavebreaking of the epw. The energy distribution of these electrons is consistent with the simulations which suggest a Maxwellian distribution with $k_bT = 0.5mv_{ph}^2$.

6.2 Original Contributions

Several of the summary statements are based upon the work performed by the author. The measurements of the spatial and temporal growth of SRS EPW were first made by him. (Phys. Rev. Lett. 57,337 (1986)) He was also the first to observe electron plasma waves at densities in the range $0.15 - 0.25n_{cr}$. The scattered EM signal with a wavelength of $2\lambda_o$ has never been observed previously in a CO_2 laser experiment. The correlation of the EPW fluctuation levels with the number of fast electrons has never been made before either. The author was also

the first investigator to show the simulations of the hot electron production were valid. This was done by measuring the EPW spectra and comparing them with the simultaneous electron velocity distributions (Phys. Fluids 29,3451 (1986)).

6.3 Suggestions for Further Work

In the course of this work, many questions concerning SRS were answered. Some questions were also raised. A spectrally and temporally integrated IR signal near 15μm was observed. The Thomson scattering geometry did not permit examination of the EPW that should be associated with this IR. It may be worthwhile to setup a proper scattering geometry to see these wave. A splitting of the $2\lambda_o$ IR spectrum suggested that a 200 kG magnetic field may be present. Although it may be difficult, the direct observation of such a field should be made, to check that this explanation of the splitting is correct. The gap in the scattered IR spectrum was ascribed to the absorption of the IR light as it leaves the plasma. It would be beneficial to check that the absorption is adequate to confirm this explanation. To this end, it would be necessary to measure the temperature distribution in the plasma when SRS occurs. The absorption is easily calculated from this temperature distribution and the previously measured density distribution.

REFERENCES

1. For examples, see ref.65,69,79

2. Estabrook, K., Kruer, W.L., Lasinski, B.F., Phys.Rev.Lett. 45,1399 (1980); Estabrook, K., Kruer, W.L., Phys. Fluids 26,1892 (1983)

3. Kruer, W.L., Estabrook, K., Lasinski, B.F., Langdon, A.B., Phys. Fluids 23,1326 (1980)

4. Manley, J.M. and Rowe, H.E., Proc. of the IRE 44,904 (1956)

5. Jackson, J.D., Classical Electrodynamics, John Wiley, N.Y., 1975

6. Shen, Y.R., Principles of Nonlinear Optics, John Wiley, N.Y., 1984

7. Tsytovich, V.N., Nonlinear Phenomena in Plasmas, Plenum Press, N.Y., 1970

8. Forslund, D.W., Kindel, J.M., Lindman, E.L., Phys.Fluids18,1002 (1975)

9. Drake, J.F., Kaw, P.K., Lee, Y.C., Schmidt, G., Liu, C.S., Rosenbluth, M.N., Phys. Fluids 17,778 (1974)

10. Langdon, A.B., Lasinski, B.F., Kruer, W.L., LLL Report UCRL-50021-73-1 p.187 (Jan-June 1973)

11. Ichimaru, S., Basic Principles Of Plasma Physics,p.59,199, Benjamin Cummings, Reading, Mass., 1973

12. Chen, F.F., Introduction to Plasma Physics,p.322 , Plenum Press, N.Y., (1974)

13. McKinstrie, C.J., Simon, A., Phys.Fluids 28,2602 (1985)

14. Hiob, E., Barnard, A.J., Phys. Fluids 26,3119 (1983)

15. Kroll, N.M., J.Appl.Phys. 36, 34 ,Sec.IIIB2 (1965)

16. Rosenbluth, M.N., Phys.Rev.Lett 29,565(1972)

17. Pesme, D., Laval, G., Pellat, R., Phys. Rev. Lett. 31, 203 (1973)

18. DuBois, D.F., Forslund, D.W., Williams, E.A., Phys.Rev.Lett. 33,1013 (1974)

19. Chambers, F.W., Bers, A., Phys.Fluids 20, 465 (1977)

20. Drake, J.F., Lee, Y.C., Phys.Rev.Lett 31,1197 (1973)

21. Dawson, J.M., Oberman, J., Phys.Fluids 5,517 (1962); 6,394 (1963)

22. Sagdeev, R.Z., Galeev, A., Nonlinear Plasma Theory, W.Benjamin, N.Y., 1969

23. Kruer, W.L., Dawson, J.M., Phys.Rev.Lett. 25,1174 (1970)

24. Simon, A., Short, R.W., Williams, E.A., Dewandre, T., Phys. Fluids 26,3107 (1983)

25. Langdon, A.B., Lasinski, B.F., Kruer,W.L., Phys.Rev.Lett. 43,133 (1979)

26. Langdon, A.B., Lasinski, B.F., Methods in Comp. Phys. 16,327 (1976)

27. Karttunen, S.J., Plasma Phys. 22,151 (1980)

28. Karttunen, S.J., Phys.Rev.A 23,2006 (1981)

29. Heikkinen, J.A., Karttunen,S.J., Phys.Fluids 29,1291 (1986)

30. Koch, P., Williams, E.A., Phys. Fluids 27,2346 (1984)

31. O'Neil, T., Phys.Fluids 8,2255 (1965)

32. Klein, H.H., Ott, E., Manheimer, W.M., Phys.Fluids 18,1031 (1975)

33. Van Wakeren, J.H.A., Hopman, H.J., Phys.Rev.Lett. 28,295 (1972)

34. Max, C.E., Manheimer, W.M., Thomson, J.J., Phys.Fluids 21,128 (1978)

35. Barr, H.C., Rankin, R., Boyd, T.J.M., Phys.Lett. 105A,218 (1984)

36. Barr, H.C., Boyd, T.J.M., Gardner, L.R.T., Rankin, R., Phys. Fluids 27,2730 (1984)

37. Boyd, T.J.M., Gardner, G.A., Rankin, R., Phys.Fluids 28,1193 (1985)

38. Rankin, R., Boyd, T.J.M., Phys.Fluids 28,3380 (1985)

39. Salimullah, M., Liu, Y.G., Haines, M.G., Phys. Rev. A 30,3235 (1984)

40. Slusher, R.E., Surko, C.M., Phys.Fluids 23,472 (1980)

41. Vinogradov, A.V., Zeldovich, B.Y., Sobelman, I.I., JETP Lett. 17,195 (1973)

42. Kruer, W.L., Phys. Fluids 23, 1273 (1980)

43. Dawson, J.M., Rev.Mod.Phys. 55,403 (1983)

44. Forslund, D.W., Kindel, J.M., Lindman, E.L., Phys. Fluid 18,1017 (1975)

45. Estabrook, K., Kruer, W.L., Phys.Rev.Lett. 53,465 (1984)

46. Forslund, D.W., Kindel, J.M., Mori, W.B., Joshi, C., Dawson, J.M., Phys.Rev.Lett. 54,558 (1985)

47. Bernard, J.E., Ph.D Thesis 1985 UBC

48. Bernard, J.E., UBC Plasma Physics Report No.104

49. Houtman, H., Walsh, C.J. UBC Plasma Physics Report NO.79

50. Houtman, H., Meyer, J., Hilko, B., Rev.Sci.Instrum. 53,1369 (1982)

51. Houtman, H., Meyer, J., J.Appl.Phys 57,4892 (1985)

52. Popil, R., Ph.D. Thesis 1984 UBC

53. Houtman, H., Meyer, J., Appl. Optics 23,2178 (1984)

54. Bernard, J.E., Meyer, J., Phys.Fluids 29,2313 (1986)

55. Shapiro, A.H., Dynamics and Thermodynamics of Compressible Fluid Flow, V.1, Ronald Press Co., N.Y., 1953

56. Sheffield, J., Plasma Scattering of Electromagnetic Radiation, Academic Press, N.Y., 1975, Chap.1-2

57. Goodman, J.W., Introduction to Fourier Optics, p.83-89, McGraw-Hill, N.Y., 1968, pp.88-89

58. Born, M., Wolf, E., Principles of Optics, Pergamon Press, 1980

59. Klein, M.V., Optics, John Wiley, N.Y., 1970

60. McIntosh, G., M.Sc. Thesis UBC 1983

61. Elazer, J., Toner, W.T., Wooding, E.R., Plasma Physics 23,813 (1981)

62. Villeneuve, D.M., Baldis, H.A., Walsh, C.J., Phys.Fluids 28,1591 (1985)

63. Walsh, C.J., Villeneuve, D.M., Baldis, H.A., Phys.Rev. Lett. 53,1445 (1984)

64. Turner, R.E., Phillion, D.W., Campbell, E.M., Estabrook, K.G., Phys. Fluids 26,579 (1983)

65. Seka, W., Williams, E.A., Craxton, R.S., Goldman, L.M., Short, R.W., Tanaka, K., Phys.Fluids 27,2181 (1984)

66. Seka, W., Afeyan, B.B., Boni, R., Goldman, L.M., Short, R.W., Tanaka, K., Johnston, T.W., Phys.Fluids 28,2570 (1985)

67. Shepard, C.L., Tarvin, J.A., Berger, R.L., Bussch, G.E., Johnson, R.R., Schroeder, R.J., Phys. Fluids 29,583 (1986)

68. Tanaka, K., Goldman, L.M., Seka, W., Richardson, M.C., Soures, J.M., Williams, E.A., Phys. Rev. Lett. 48,1179 (1982)

69. Figueroa, H., Joshi, C., Azechi, H., Ebrahim, N.A., Estabrook, K., Phys.Fluids 27,1887 (1984)

70. Kruer, W.L., Comm.Plasma.Phys.Controlled Fusion 9,62 (1985)

71. Zimmerman, G.B., Kruer,W.L., Comm.Plas.Phys.Cont.Fusion 2,51 (1975)

72. Offenberger, A.A., Fedosejevs, R., Tighe, W., Rozmus, W., Phys.Rev.Lett. 49,371 (1982)

73. Watt, R.G., Brooks, R.D., Pietrzyk, Z.A., Phys.Rev.Lett. 41,170 (1978)

74. Watt, R.G., Pietrzyk, Z.A., Appl.Phys.Lett. 37, 1068 (1980)

75. McGoldrick, E., Sim, S.M.L., Opt. Comm. 40,433 (1982)

76. Turner, R.E., Estabrook, K., Kauffman, R.L., Bach, D.R., Drake, R.P., Phillion, D.W., Lasinski, B.F., Campbell, E.M., Kruer, W.L., Williams, E.A., Phys. Rev. Lett. 54,189 (1985)

77. Rozmus, W., Offenberger, A.A., Fedosejevs, R., Phys.Fluids 26,1071 (1983)

78. Offenberger, A.A., Fedosejevs, R., Rozmus, W., Physica Scripta T2,498 (1982)

79. Phillon, D.W., Banner, D.L., Campbell, E.M., Turner, R.E., Estabrook, K.G., Phys. Fluids 25,1434 (1982)

80. Nugent, K.A., Luther-Davies, B., Phys.Rev.Lett. 49,1943 (1982)

81. Turner, R.E., Phillion, D.W., Lasinski, B.F., Campbell, E.M., Phys.Fluids 27,511 (1984)

82. Bobin, J.L., Decroisette, M., Meyer, B., Vitel, Y., Phys.Rev.Lett. 30,594 (1973)

84. Nishimura, H., Azechi, A., Nakai, M., Uchida, S., Sakawa, Y., Wada, T., Hasegawa, H., Sakurai, H., Yamanaka, T., Yamanaka, C., Opt. Comm. 56,409 (1986)

84a. Stamper, J.A., MacLeans, E.A., Ripin, B.H., Phys. Rev. Lett. 40,1177 (1978) and Raven, A., Willi, O., Rumsby, P.T., Phys. Rev. Lett. 41,554 (1978)

85. Villeneuve, D.M., Walsh, C.J., Baldis, H.A., Phys.Fluids 28,1454 (1985)

86. Drake, R.P., Turner, R.E., Lasinski, B.F., Estabrook, K.G., Campbell, E.M., Wang, C.L., Phillion, D.W., Williams, E.A., Kruer, W.L., Phys. Rev. Lett. 53,1739 (1984)

86. Simon, A., Seka, W., Goldman, L.M., Short, R.W., Phys. Fluids 29,1704 (1986)

87. Simon, A., Short, R.W., Phys.Rev.Lett. 53,1912 (1984)

87a Johnston, T.W., Dawson, J.M., Phys.Fluids 16,722 (1973)

88. Ebrahim, N.A., Joshi, C., Phys.Fluids 24,138 (1981)

89. Barr, H.C., Gardner, G.A., Proc. of Int. Conf. on Plasma Phys. Lausanne 1984, Contributed Papers V.II,265

90. Darrow, C., Umstadter, D., Katsouleas, T., Mori, W.B., Clayton, C.E., Joshi, C., Phys.Rev.Lett. 56, 2629 (1986)

91. Meyer, J., Houtman, H., Phys. Fluids 28,1549 (1985)

92. Ginzberg, V.L., The Propagation of Electromagnetic Waves in Plasmas, Pergamon Press, Oxford, 1970 pp.277-280

93. Boyd, T.J.M., Can.J.Phys. 64, 944 (1986)